# ELECTROHYDRODYNAMICS OF ELECTROSPRAYED CHARGED DROPLETS IN A VORTICAL FLOW

A Dissertation
Presented to
The Academic Faculty

by

Jung Yun Lee

In Partial Fulfillment
of the Requirements for the Degree
Doctor of Philosophy in the
School of Mechanical Engineering

Georgia Institute of Technology
August 2020

# ELECTROHYDRODYNAMICS OF ELECTROSPRAYED CHARGED DROPLETS IN A VORTICAL FLOW

Approved by:


Dr. Andrei Fedorov, Advisor
School of Mechanical Engineering
*Georgia Institute of Technology*

Dr. Devesh Ranjan
School of Mechanical Engineering
*Georgia Institute of Technology*

Dr. Peter Kottke
School of Mechanical Engineering
*Georgia Institute of Technology*

Dr. S. Mostafa Ghiaasian
School of Mechanical Engineering
*Georgia Institute of Technology*

Dr. Matthew Torres
School of Biological Sciences
*Georgia Institute of Technology*



Date Approved: April 21, 2020

To my husband Young Moon

and my children Sion and Yireh

# ACKNOWLEDGEMENTS

I would first like to thank my husband Young Moon Song and my two children Sion and Yireh. Their loving support and encouragement have always sustained me in every step to the completion of this journey.

My deepest gratitude and appreciation go to my advisor Dr. Andrei Fedorov and Dr. Peter Kottke for their incredible guidance, encouragement, and support in every possible way. Their enthusiasm and positivity have been an inspiration for me to want to become a researcher like them. I am thankful to Dr. Matthew Torres for providing his instructional support and valuable input into my research.

My appreciation also extends to my colleagues in the Fedorov group, Joel Chapman for his direct contribution to my research and other fellow students for their friendship and support in many ways.

My research was supported by Grant Number 5R01GM11262-02 from the National Institute of General Medical Science (NIGMS), a component of the National Institutes of Health.

# TABLE OF CONTENTS

# LIST OF FIGURES

# LIST OF SYMBOLS AND ABBREVIATIONS

| | |
|---|---|
| $Ab_n$ | Ion abundance of n-th peak |
| $C_C$ | Cunningham correction factor |
| $C_d$ | Drag coefficient |
| CSD | Charge state distribution |
| $D$ | Nozzle diameter |
| $d_d$ | Droplet diameter |
| $D_g$ | Diffusion coefficient |
| $D_H$ | Hydraulic diameter |
| DRILL | DRy Ion Localization and Locomotion |
| $d_{TO}$ | Turbulence onset distance |
| $\vec{E}$ | Electric field |
| ESI | Electrospray Ionization |
| $\varepsilon$ | Solvent permittivity |
| $\varepsilon_0$ | Vacuum permittivity |
| $F_C$ | Centrifugal force |
| $\vec{F}_D$ | Drag force |
| $\vec{F}_E$ | Electric force |
| $f_{rel}$ | Droplet release frequency |
| $g$ | Gravitational acceleration |
| $\gamma$ | Solvent surface tension |
| $h$ | Flow thickness |
| HPLC | High purity liquid chromatography |

| | |
|---|---|
| I | Spray current |
| ID | Inner diameter |
| $K$ | Solvent conductivity |
| $k$ | Gladstone-Dale coefficient |
| LOD | Limit of Detection |
| $M_{avg}$ | Abundance weighted average mass |
| $m_d$ | Droplet mass |
| $m_n$ | Mass at n-th peak |
| MS | Mass spectrometry |
| $n$ | Refractive index |
| NPSA | Non-polar surface area |
| OD | Outer diameter |
| $q$ | Droplet charge |
| $q_{Ry}$ | Rayleigh stability limit |
| $\dot{Q}$ | Gas flow rate |
| $r$ | Radial position |
| $\bar{R}$ | Hydraulic radius |
| $r_c$ | Capillary radius |
| $R_d$ | Droplet radius |
| $Re$ | Reynolds number |
| RSD | Relative standard deviation |
| $R_u$ | Universal gas constant |
| $S$ | Swirl number |
| $Sc_g$ | Schmidt number |
| $Sh_d$ | Sherwood number |

| | |
|---|---|
| SNR | Signal-to-noise ratio |
| SRM | Selective reaction monitoring |
| T | temperature |
| $\tau_d$ | Droplet relaxation time |
| $\vec{u}$ | Gas velocity |
| $\vec{v}$ | Droplet velocity |
| $u_z$ | Gas axial velocity |
| $u_\theta$ | Gas swirl velocity |
| $V_C$ | Capillary voltage |
| $V_f$ | Liquid flow rate |
| $V_j$ | Volume of mesh element j |
| $y_f$ | Mass fraction of the solvent at the droplet surface |
| $y_\infty$ | Mass fraction of the solvent in the far-field away from the droplet |
| $\theta$ | Spray cone half angle |
| $\lambda$ | Gas mean free path |
| $\mu$ | Gas dynamic viscosity |
| $\nu$ | Gas kinematic viscosity |
| $\rho$ | Gas density |
| $\rho_d$ | Droplet density |
| $\rho_s$ | Charge density |
| $\psi$ | Electrical potential |

# SUMMARY

Electrospray ionization has become a popular method to produce ultra-small charged liquid droplets. The coupling of electrospray ionization to mass spectrometry (ESI-MS) has enabled determination of the composition of complex biological samples with applications including biomarker discovery and disease diagnosis. Improvement in ESI-MS sensitivity can be achieved via effective desolvation of electrosprayed charged droplets and more efficient transport of dry analyte ions into the mass analyzer. Based on a novel implementation of swirling flow, an ESI-MS interface developed as part of this dissertation exploits a vorticial gas flow to advantageously alter the spatial size-distribution of droplets. Numerical and experimental studies using a prototype vortical MS interface indicate that large droplets are displaced to the periphery of the electrospray plume under the influence of the outward inertia of the vortex flow, resulting in reduction in chemical noise with improvement in sensitivity. The objective of this research is to increase the understanding the behavior of electrosprayed charged droplets via theoretical and experimental studies focused on (1) the effects of a vortical flow on the spatial size-distribution and (2) the effects of the coupling of a vorticial flow to an active suction flow on droplet transmission. Multiphysics modeling considers vortical flow hydrodynamics in the presence of suction, applied external electric fields, and inter-droplet electrostatic interactions (space charge) to study their impact and ability to control charged droplets of differing size and charge. Experimental flow visualization and ion current measurements are used to provide basic insight into the phenomena and validation of model predictions. The successful

implementation of the work presented in this dissertation provides valuable input and insights into the vorticial ESI-MS interface design and operation.

# CHAPTER 1. INTRODUCTION

This chapter introduces electrospray ionization (ESI) mass spectrometry (MS) with focus on the limitations and opportunities for improvement in transfer of charged analytes from liquid aerosol phase to partially or preferably fully desolvated gas phase ion required for MS sensing. With this background, previously studied aerodynamic interfaces are critically discussed for coupling and efficient transfer of ESI generated droplets to the vacuum environment of a mass spectrometer. This motivates need for innovation in methods and design of novel approaches for droplet/ion transmission in atmospheric pressure (AP) environment based on fundamental understanding of electrohydrodynamics of charged droplets in complex gas flows designed to effectively separate smaller (desired) from larger (undesired) droplets and transmission of smaller (desolvated) droplets to an ion collection capillary. In a vortical flow, inertial effects are exploited for separation of electrosprayed droplets based on their size, which can be useful not only in ESI-MS but other spray applications beyond mass spectrometry. Specifically, this dissertation research explores behavior of variable size population of electrosprayed droplets subjected to a vortical flow with point-like suction. This introductory chapter concludes with the dissertation organization and overview of the entire body of work.

## 1.1 Mass Spectrometry

Mass spectrometry (MS) is a powerful analytical technique used to detect, identify and quantify chemical and biological compounds by measuring the mass-to-charge ratio (m/z) of analyte ions. The results are presented as a mass spectrum, a plot of ion abundance as a function of mass-to-charge ratio. The technique enables elucidation of the structure

and chemical properties of large biopolymers, including covalent and non-covalent interactions, analysis of complex samples with high selectivity and sensitivity. As a result, MS has become an important technology across a broad range of fields and applications, particularly in life science research areas such as proteomics, metabolomics and lipidomics. Some important applications include protein characterization, sequencing of peptides, and identification of protein post-translational modifications [1]. It is also invaluable in pharmaceutical and clinical research for drug discovery, cancer screening , and biomarker profiling [2]. The method is an efficient analytical tool for characterization of contaminants in air, water and soils [3]. In forensic testing laboratories, MS is used for analysis of trace evidence, arson investigation, confirmation of drug abuse, and identification of explosive residues [4].

A prerequisite for MS analysis is sample ionization. There are various methods to produce gas phase ions suitable for mass spectrometric analysis. Hard ionization techniques, such as electron ionization, deposit large quantities of residual energy, resulting in a high degree fragmentation of the subject molecule. Notable examples include fast atom bombardment (FAB) which uses a beam of high energy ions to impact a surface, on which the analyte molecule is applied, to generate ions; atmospheric-pressure chemical ionization (APCI) uses heated nebulizer gas to convert spray of analyte solution into a gas stream which is ionized by corona discharge under atmospheric pressure. In soft ionization methods, little energy is deposited in ionization leading to low fragmentation, which makes them suitable for analysis of fragile and easily fragmentable species such as biomolecules (DNA, proteins, peptides) and large organic molecules (polymers, macromolecules). In matrix-assisted laser desorption/ionization (MALDI), a mixture of the sample and a laser

energy absorbing matrix material is applied on a metal plate and then irradiated by a pulsed laser, producing a hot plume of ions. Electrospray ionization (ESI) uses a high intensity electric field to generate electrically charged droplets from the electrohydrodynamically unstable Taylor cone-jet. ESI is the softest ionization technique and produces more multiply charged ions from solvated molecules, facilitating analysis of large macromolecules, is the ionization method of interest for this dissertation.

In typical analytical workflows, charged droplets in ESI are generated under atmospheric pressure conditions and need to be transmitted to a vacuum environment of a mass spectrometer. The vacuum in the MS analyzer region is produced with high-performance pumping systems capable of gas pumping rates up to hundreds of standard liters per hour. To avoid an overload on the pumps, an internal vacuum of MS is separated from the external atmospheric pressure environment by a small diameter inlet capillary (ID 0.5 – 0.6mm), which is used for introduction of ionized molecules generated by the ion source. The small size of inlet capillaries poses a constraint on efficient transport of ions in their fully desolvated "dry" state or solvated state, e.g., disolved in preferably small charged droplets, into the mass spectrometer for analysis.

## 1.2 Electrospray Ionization (ESI) – Mass spectrometry (MS)

Electrospray ionization (ESI), a technique for creation of a charged aerosol by electrohydrodynamically dispersing a liquid electrolyte subjected to strong electric fields, was proposed as a source of gas-phase ions suitable for mass spectrometric analysis by Dole in 1968 [5], and demonstrated for soft ionization and mass spectrometric detection of large molecular weight biopolymers by Yamashita and Fenn in 1984 [6]. The significance

of ESI-MS for bioanalytical applications was recognized by the 2002 Nobel Prize in Chemistry awarded to ESI pioneer Professor John Fenn.

### *1.2.1 ESI-MS Process Description*

As shown in Figure 1.1, production of aerosolized charged droplets and resulting gas phase ions entails through three major processes: (1) generation of electrospray by discharging an electrolyte solution from a capillary needle using an imposed electric field, (2) spray breakup resulting in a population of primary (parent) charged droplets which, via solvent evaporation and repeated fission events, lead to generation of a sub-population of very small, highly charged droplets, and (3) generation of gas phase ions from the very small, highly charged droplets due to competing mechanisms of complete desolvation (charge residue model) or ion escape from the droplet surface to gas phase (ion evaporation model).

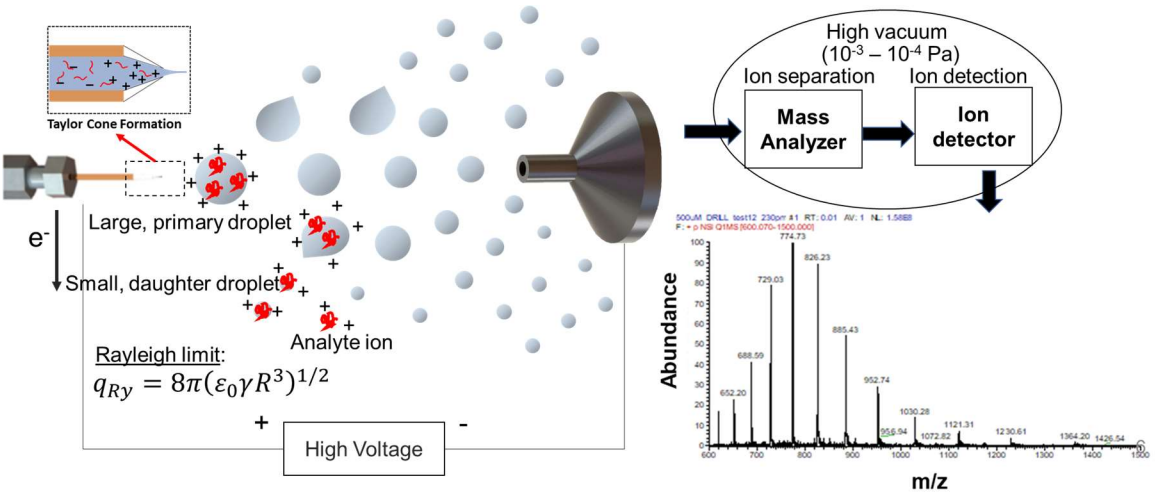


**Figure 1.1 Sequence of Processes in Positive Mode ESI-MS Workflow**

#### 1.2.1.1 Electrospray production of charged droplets

For charged droplet formation, a capillary filled electrolyte is subjected to a high electric field created by a large electrical potential difference between the capillary and the mass spectrometer inlet, which serves as a counter-electrode. The typical solution in which sample is dissolved consists of a polar solvent (i.e. water, methanol) and dissociative additives (i.e. acetic or formic acids) that provide protons or anions for analyte charging via adduct formation. The electric field generates the electrokinetic flow of the solution at the capillary tip, which induces free charge migration towards the extended meniscus of the liquid resulting in high charge density along the liquid interface. With increasing electric field, the liquid surface starts to protrude into a conical shape, known as the Taylor cone, due to electrical stresses present on the surface [7]. At a certain threshold of electric field intensity the Maxwell electrical stresses at the fluid interface overcome surface tension and a liquid jet emanates from the tip of the cone, liberating charged droplets. Theoretically derived equations in Eq (1.1) [8] and empirical experiment-based correlations in Eq (1.2) [9] provide a dependence of the initial size of electrosprayed droplets on liquid properties and flow rate.

$$R_d = \left( \frac{3\varepsilon\gamma^{1/2} V_f}{4\pi\varepsilon_0^{1/2} KE} \right)^{2/7} \tag{1.1}$$

$$R_d \approx \left( V_f \varepsilon / K \right)^{1/3} \tag{1.2}$$

where $R_d$ is the droplet radius, $\gamma$ is the solvent surface tension, $V_f$ is the liquid flow rate, $\varepsilon_0$ is the vacuum permittivity, $\varepsilon$ is the solvent permittivity, E is the electric field at capillary tip, and $K$ is the solvent conductivity.

#### 1.2.1.2 Production of smaller, high charge density droplets from primary parent droplets

The physics of electrospray phenomena is complex and remains a subject of intense theoretical and experimental investigations. Current evidence suggests that electrospray starts with generation of mono- or binary- size droplets by instability-induced breakup of the liquid jet. Primary, or "parent," droplets experience solvent evaporation due to thermal energy provided by the background gas. On the other hand, direct emission of charge from primary droplets (known as ion evaporation) requires significant energy input to overcome kinetic energy barrier and, therefore, is unlikely favoring less energy intensive solvent evaporation. In a liquid droplet of sufficient ionic conductivity, excess charges mutually repel and move until they are uniformly distributed over the droplet free surface to reach electrostatic quasi-equilibrium [10]. Reduction in droplet size leads to an increase in surface charge density, which causes increased Coulombic repulsion between surface charges and perturbation of the droplet equilibrium shape, leading to elongation and finally ejection of multiple smaller ("daughter") droplets from the elongated tail of a primary droplet [11]. Experimental observations suggest that such a fission event results in the production of about 20 offspring droplets at a time, which account for only 2% mass but 15% of the charge of the parent droplet [11]. Therefore, the charge concentration, i.e., charge-to-volume ratio, in a small progeny droplet is much greater than that of a mother droplet. Rayleigh [12] determined the critical charge (in Coulombs) which will cause such a fission event for a spherical droplet, known as the Raleigh stability limit and expressed as,

$$q_{Ry} = 8\pi\left(\varepsilon_0 \gamma R_d^3\right)^{\frac{1}{2}} \tag{1.3}$$

where $\varepsilon_0$ is the permittivity of vacuum, $\gamma$ is the solvent surface tension, and $R$ is the droplet radius. Any charged droplet that carries charge greater than the Rayleigh limit fissions due to instabilities induced by imbalance of electrostatic forces and generates multiple small progeny droplets with a high charge density. Over time, primary parent droplets experience repeated solvent evaporation and fission events to ultimately create a large number of small, highly charged offspring droplets in the state desirable for mass spectrometric analysis.

#### 1.2.1.3 Production of gas-phase ions from small, highly charged droplets

Transfer of ions from liquid droplets to gas phase is a crucial process in ESI – MS. Completely "dry" analyte ions free of solvent molecules or other (e.g., salt clusters) adducts with charge supplied by either addition of proton(s) (positive mode ESI) or hydroxyl groups (negative mode) enable accurate measurements of mass to charge ratio, and hence unambiguous determination of the analyte intrinsic molecular weight and chemical makeup [13]. The mechanism of ion formation from charged droplets has been a subject of extensive research and vigorous debate with two postulated mechanisms likely responsible for production of gas-phase ions. Figure 1.2 depicts the sequence of events stipulated by the ion evaporation model (IEM) and the charge residue model (CRM).

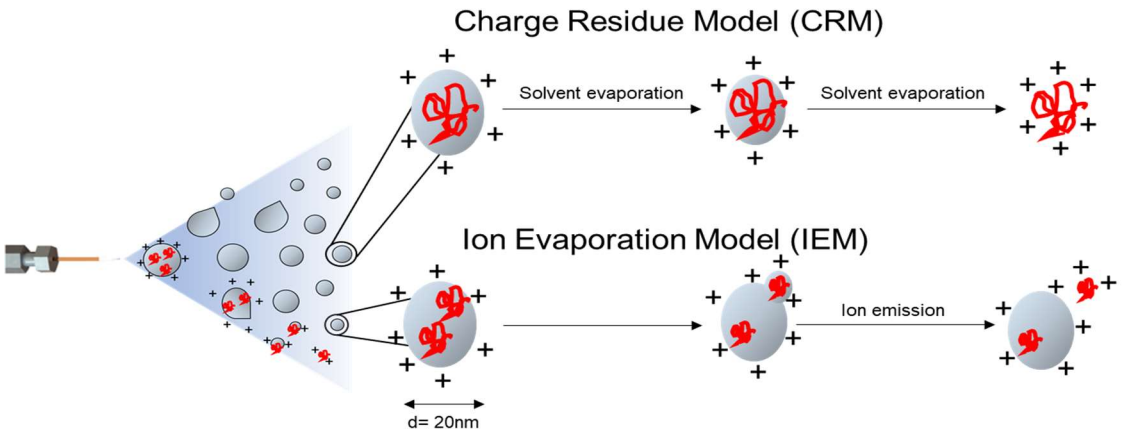


**Figure 1.2. Two mechanisms of production of gas-phase analyte ions: ion evaporation model (IEM) and the charge residue model (CRM)**

The IEM [14, 15] is based on the fact that the electric field generated in a charged nanodroplet (d=20$nm$) after many rounds of fission events is sufficient to enable direct emission of ions (with a few solvent molecules as adducts) from the droplet surface. Residual solvent molecules may be removed from the ion as they collide with background gases during flight. Low molecular weight species and small inorganic ions are thought to be liberated by the mechanism described by the ion evaporation model [14]. The CRM [5, 16-18] postulates that production of ions is possible through complete desolvation of charged nanodroplets (~100 $nm$ diameter) containing a single analyte molecule. This mechanism is thought to be preferred for transfer of large, globular analytes into the gas-phase [19]. As the solvent layer disappears, the elementary excess charges (protons or hydroxyls) in a diminishing droplet are transferred to the analyte [16, 17]. Both the mechanisms indicate that the release of gas-phase ions, the desirable form for MS analysis, is possible from small nanodroplets which are attainable via successive evaporation and fission of primary droplets. These small offspring droplets are the main producers of detectable ions [20]. In addition, ions derived from small offspring droplets are associated

with “cleaner” mass spectra showing reduced noise and improved sensitivity of analyte detection (as compared to ions originating from larger “mother” droplets whose spectral signature comes with significant background noise associated with undissolved water clusters) [21]. Therefore, size-selective extraction of smaller, highly charged droplets from the charged aerosol of variable size parent-offsping droplets and subsequent transmission of these small droplets to the mass spectrometer intake are fundamental to improved efficiency (reduction of analyte loss) and enhanced sensitivity (minimizing excess of solvent-induced noise) of mass spectrometric analysis.

### *1.2.2 Limitations and Opportunities in ESI-MS*

MS is one of the most sensitive methods in analytical chemistry. Its low limit of detection (LOD) is directly related to the capability to distinguish a signal from a vanishingly small amount of the analyte of interest from the noise. Contributions to spectral noise come from different sources with contributions from residual solvent molecules and dissolved adducts (e.g., salts and solvent impurities) being of primary concern for analysis of biomolecules. Coupling of MS with ESI as a soft ionization method has assumed a prominent role in many biomedical studies that require analysis for trace amounts of metabolites, peptides and proteins. The sensitivity of ESI-MS strongly depends on the effectiveness of production and transport of fully or partially “dry” ions formed on the basis of biomolecules in the atmospheric pressure region prior to introduction to the MS inlet via vacuum suction. It is quite striking that in ESI – MS, 80% of electrosprayed analyte ions are lost due to lack of desolvation [22]. Complete desolvation would potentially offer a five-fold improvement in the number of analyte ions available for improved spectral peak signal.

Complete ion desolvation is not the only important fact for improving the sensitivity of MS detection. Poor ion transmission efficiency is the other key factor, which is due in large part to a requirement to introduce the mutually repelling ions/small droplets into a small diameter inlet of the mass spectrometer, which is needed to maintain the first stage vacuum. An electrospray plume is heterogeneous and consists of larger in size primary droplets and smaller, highly charged progeny droplets with gas-phase ions produced as a result of evaporation and fission of small daughter droplets. This population of charged droplets and ions experiences a rapid radial growth as it moves towards the MS inlet under the influence of applied electric field and potentially an external carrier gas. What ultimately enters the mass spectrometer is determined by the size and geometry of the intake structure at the inlet to the mass spectrometer. The flow suction at the MS inlet results in droplet/ion extraction; the suction flow rate is determined by the capacity of a vacuum pump (which can only handle a certain gas load) and the required vacuum level in MS (10-3 Pa). These two effects – the plume expansion and droplet extraction due to flow suction – form an important fundamental trade-off whose understanding is essential for design of an efficient ion capture process. This radial plume expansion is largely due to the repulsive nature of inter-droplet interactions in a droplet population with same sign charge, commonly referred as the space-charge effect. As a result, in typical configuration with passive electrospray, the charged aerosol plume quickly grows to an extent much greater than that of a typical MS inlet orifice diameter (0.5 – 0.6 mm), thus allowing only a small fraction of charged droplets/ions to enter the mass spectrometer inlet.

Owing to the nature of space-charge interactions, droplets of different size and charge density occupy different regions in an electrospray plume [23]. The central region is mostly

occupied by large, primary droplets and the small, highly charged daughter droplets are located at the outer periphery. Near the MS intake, the spatial distribution of droplets is a result of the combined effects of electrical (due to charges on droplets and external electric field) and mechanical (friction due to surrounding stagnant gas and suction flow) forces that directs droplet motion in size (inertia) dependent manner, leading to preferential losses (no transmission to MS) of smaller, highly charged droplets moving further away from the MS inlet. Because gas-phase ions are most effectively derived from these small, highly charged droplets, the loss of large percentage of small progeny droplets results in substantially reduced MS sensitivity. Many ESI – MS interface designs have been developed and demonstrated to address the limitations associated with low transmission of the most valuable (small, highly charged) daughter droplets.

### *1.2.3 ESI – MS Interfaces for Improved Small Droplet Transmission*

The ESI source interfaces with MS, including their structural aerodynamic features and geometric orientation relative to the MS inlet, have continuously evolved to overcome the challenges associated with efficient generation and transport of small, charged droplets/gas-phase ions into a mass spectrometer. ESI droplets, while moving through gas at atmospheric pressure, experience strong cooling due to solvent evaporation [24, 25], resulting in a negative feedback loop of reducing evaporation rates and therefore diminishing rate of fission, production of daughter droplets, and ultimately negative impact on the MS signal. Therefore, different mitigating approaches have been introduced to improve desolvation, including incorporation of a heated auxiliary gas and a counter current gas flow to enhance both heat and mass transfer rates. Another strategy to enhance MS signal relies on preferential sampling of droplets from a portion of the ESI plume

periphery by strategic positioning of the spray source and the MS inlet, as the periphery is enriched with smaller, more highly charged droplets. This strategy is based on capturing a higher proportion of progeny droplets vs undesirable mother droplets (which are mostly located in the central location of the ES plume), and this is achieved by offsetting or angling the spray direction relative to the MS inlet orifice axis as shown in Figure 1.3 [26]. Similarly, the orthogonal positioning of pneumatically assisted electrospray in many commercial ESI – MS interfaces allows sampling from the exterior of the spray plume and hence, capturing small highly charged droplets while eliminating most larger droplets from the MS entrance [27-29].

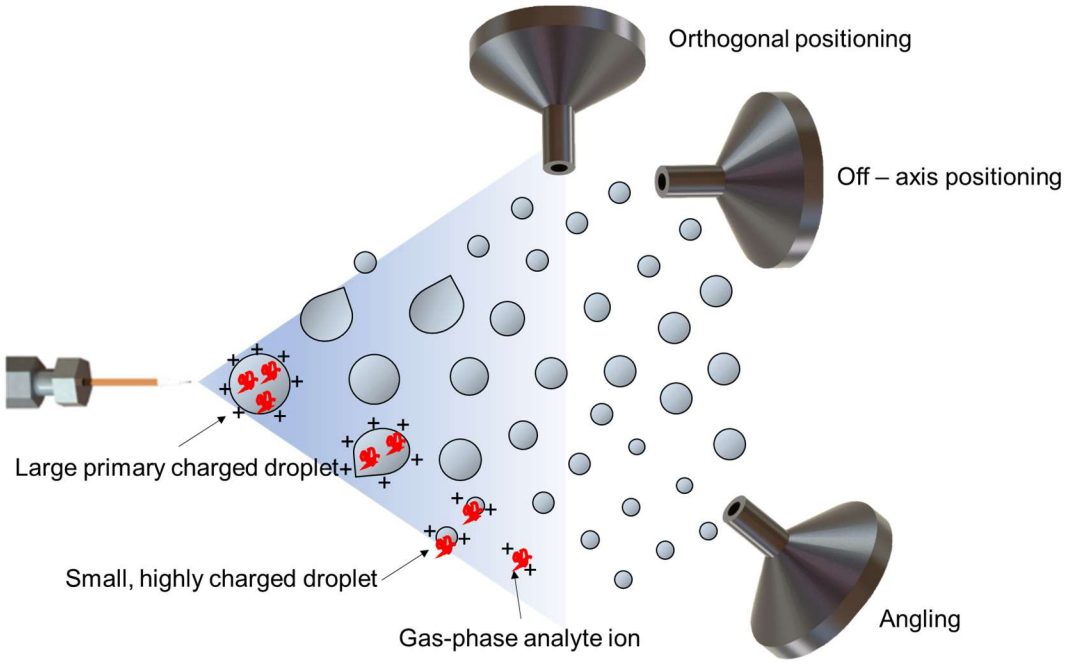


**Figure 1.3 Different sampling orientations of the MS inlet for enhanced capture of small highly charged droplets**

Another hydrodynamic-based ESI interface, shown in Figure 1.4, exploits the Coanda effect to increase the proportion of daughter droplets captured [30]. In this design,

a high velocity nebulizer assisted spray impinges on an off-axis cylindrical counter-electrode, with the impact promoting droplet break-up. The gas stream curves, following the round surface known as Coanda effect. Furthermore, flow over the round surface develops turbulence with vorticity in the flow separation region in which turbulent mixing enhances droplet desolvation. The combination of the impinging jet and vortex shedding improves heat and mass transfer and causes more rapid production of the desired smaller droplet population thus leading to higher ionization efficiency and sensitivity enhancement [30].

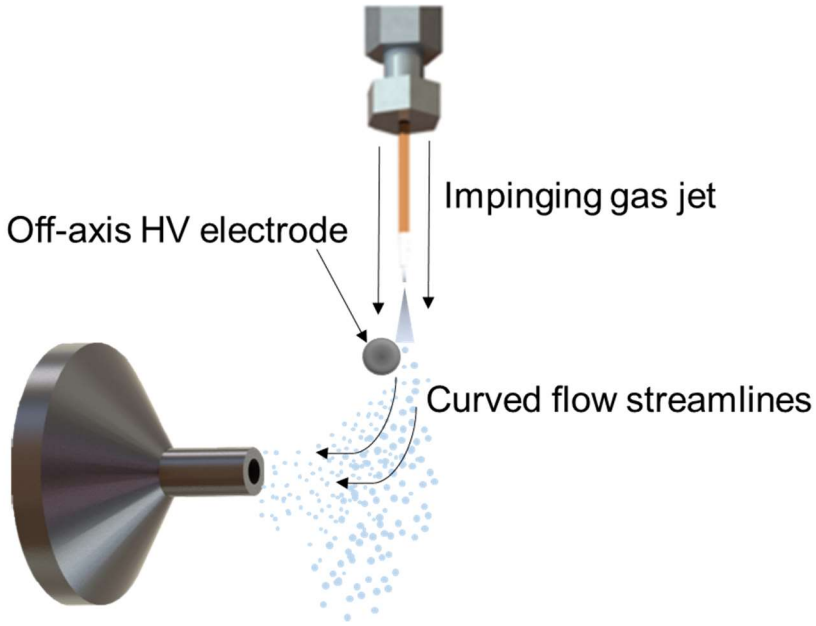


**Figure 1.4. Schematic of ion source interface exploiting the Coanda effect**

Other interfaces using Venturi flow-entrainment effects have been introduced to improve the ability to capture small highly charged droplets by focusing (reducing lateral expansion) of the electrospray plume [31, 32]. In the Venturi devices (Figure 1.5) a gas flow enters a narrow gap, accelerating to a high velocity with an accompanying pressure drop, which entrains additional gas ("gas amplification" can result in flow rates of 100

times greater than supplied from the driving gas source). The resulting high velocity gas flow leads to a reduced transit time for the rapidly expanding ESI plume so that fewer small droplets have time to transport to the periphery outside of the sampling zone at the MS inlet. However, there is no mechanism in these devices to improve selectivity of sampling small droplets over large droplets without a substantial loss in the total available droplet population in the sample, diminishing the benefit of sensitivity enhancement by size selective sampling due to overall loss of analyte transmission due to smaller available sample.

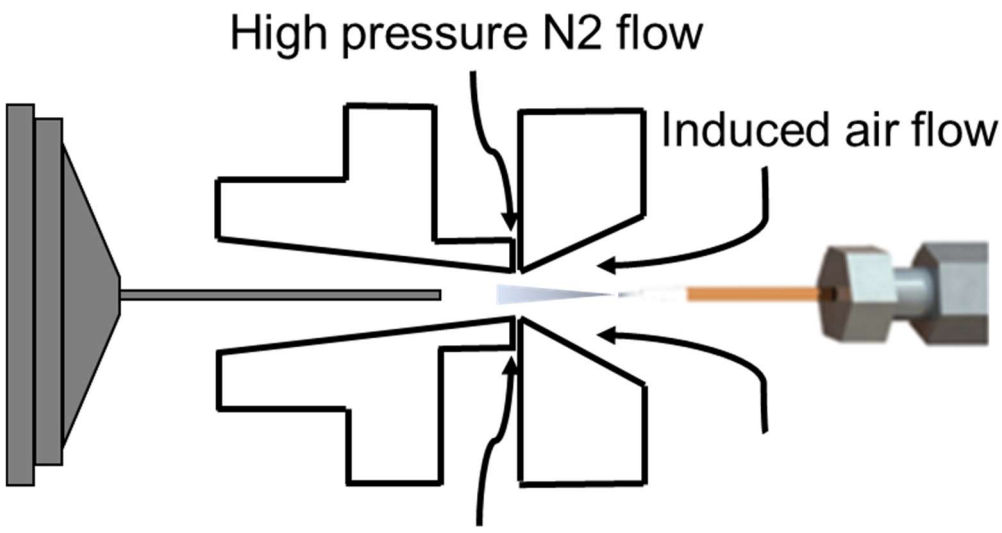


**Figure 1.5. Air amplifier ESI-MS interface exploiting the Venturi effect**

In addition to strategies based on spray re-orientation and aerodynamic manipulation of the ES plume, ESI-MS droplet transmission improvements have been sought through redesign of the MS inlet orifice to reduce ion loss (expressed in terms increased “ion conductance”) at the walls during rapid flow contraction at the intake. Importantly, MS inlet redesign to increase ion conductance and therefore increase the ion current into the MS inlet does not necessarily come with a proportional improvement in

ion signal intensities in MS spectra [22], as a large fraction of the ion current may not be associated with completely desolvated ions. The simplest inlet change is use of a larger inner diameter capillary which can handle a greater gas flow and thus entrain a greater portion of the ESI plume [33] with the spray emitter close enough to the inlet so that electrosprayed droplets are captured before the plume expands beyond the vacuum suction region. This leads to capture of a large proportion of large droplets and therefore desolvation would require the ability to provide significant heating. In an MS inlet capillary of larger inner diameter there is actually a reduced heated surface area to gas volume ratio with less effective heat transfer (and, in turn, less efficient droplet evaporation and analyte desolvation), resulting in more noise associated with parasitic intake of water molecules/clusters and reduced MS spectra quality [34]. Additionally, the increased gas load requires higher capacity and hence most expensive vacuum pumps. Alternatives to increasing the inlet diameter, such as an array of multiple inlet capillaries (allowing for increased flow intake without reduction in the heated surface area to gas volume ratio) have also been investigated. Using this arrangement, an increased ion current transmission efficiency was achieved (~23 fold) compared to the standard orifice interface, and the resulting mass spectra showed a 10 fold improvement in LOD [35]. This enhancement in sensitivity was attributed to the combined effects of high ion transmission and the desolvation efficiency. However, this approach again comes with significant increase in cost due to need for greater pumping capacity, and the high temperature used to achieve desolvation of analyte in larger mother droplets can fragment thermally labile compounds, leading to diminishing softness of ionization. In fact, attempts to use lower inlet capillary temperatures to improves softness of ionization by producing low temperature ions [36-

41], this approach has resulted in losses of sensitivity due to insufficient desolvation as expected. [35, 42]

Ion transmission has also been increased by reducing entrance losses using a funnel geometry [43] which was shown to increase the ion current into the detector, yielding a boost in signal intensity. A beam of protein ions generated by an ESI source and transmitted to the ultra-high vacuum using the funnel interface was deposited on a surface. The deposition was imaged (using scanning tunnel microscopy) to characterize all sampled charge carriers that landed on the surface. On the surface, no evidence of droplets, clusters, or contaminants was found, indicative of sufficient desolvation of protein ions. This was thought of as a result of heating supplied from the wall close to the ESI emitter. This highlights the fact that enhancements in MS sensitivity is not a simple result of increased ion current transmission. Rather, it relies at the same time on the quality of the ion current – improving limit of detection requires improving the signal to noise ratio and therefore methods that increase signal intensity but increase noise to a greater extent hurt overall performance. Improvements that prevent introduction of undesirable clusters, non-target ions, and large droplets from reaching the vacuum region would lower background noise.

### *1.2.4 Nanoelectrospray as an Intrinsic Source of Ultra-small, Highly Charged Droplets*

Nanoelectrospray is a method that improves the generation of the small highly charged droplets even as the primary parent population, which is critical to efficient ionization of analyte. The initial size of electrosprayed droplets has strong dependence on the flow rate [8, 44-46] and the sprayer orifice diameter[9, 47-49]. Nanoelectrospray uses spray capillaries with smaller tip diameters (down to 1 μm) and lower flow rates (as low as

1 nL/s). As a result, the initial droplet size generated by nanoelectrospray is an order of magnitude smaller than that of conventional electrospray, and nano-ESI yields higher quality mass spectra with improved sensitivity and less noise [50]. Nano-electrospray has become a popular choice for biological analysis due to the combined effect of low sample consumption with improved detection limits. Despite the advantages, nanoelectrospray is not applicable to in many workflows that require shorter runtime and high throughput analysis. For example, in many chemical, genetic and pharmaceutical applications, researchers conduct millions of tests at micro-liter to milli-liter per minute flow rates, which is up to 1000X greater than nano-electrospray could support, for rapid screening of diverse biomarkers, antibodies or genes.

## 1.3 DRy Ion Localization and Locomotion (DRILL) MS interface

A major part of the work described in this dissertation concerns with design of a novel ESI-MS interface. DRy Ion Localization and Locomotion (DRILL) is a new concept of aerodynamic separation of charged droplets, which exploits droplet-size dependent inertia to separate unwanted droplet populations (i.e., hard-to-desolvate large droplets) from the small, highly charged (i.e., preferred for ESI-MS) droplets in the electrospray plume, improving extraction and transmission of desirable gas-phase ions and smaller droplets that directly contribute to improved quality MS spectra and detection sensitivity of analytes.

### *1.3.1 Novel Strategy for Efficient Ion Desolvation and Transmission*

In contrast to approaches described in Section 1.2, DRILL interface adopts a different strategy without relying on increasing capillary temperature that negatively

impacts softness of ionization, source positioning which diminish the overall population of available droplets/ions for sampling and detection, or introduction of turbulent flow with greater mixing but accompanied by lack of reproducibility and predictability. Instead, it exploits laminar swirling gas flow intimately aerodynamically coupled to suction inlet to MS to achieve both the goal of selective capture of small, highly charged droplets (resulting in high ionization efficiency and reduced chemical noise) and optimized transmission path of captured small droplets/ion into the MS intake. Thus DRILL uses the same separation principle as a hydrocyclone, a device in which swirling gas flow is an effective mechanism for separating and sorting particles [51] based on the balance between droplet inertia (also referred to as centrifugal force in rotational motion) and fluid drag force experienced by droplets. The ability to sort electrospray droplets by size using inertia is complicated by the importance of electric forces, and because of the need to consider the interactions and aerodynamic coupling between high velocity swirling gas flow used for droplet separation and the suction flow used for droplet transmission into the MS inlet.

### *1.3.2 Creating a vortical flow in DRILL*

Chapter 4 presents a detailed description of the device design evolution from First Generation (Gen 1) to Final Gen 3 DRILL. Here we introduce the DRILL structure that enables creation of a swirling gas flow which was used in fundamental gas dynamics studies of vortical flow behavior using schlieren visualization. The vortex generator in DRILL mimics the concept of a conventional cyclone that has a cylinder-on-cone shape with one or multiple tangential gas inlets. Figure 1.6 shows the side and the front views of the vortex generator structure with relevant components. Gas enters the annular fluid domain (enclosed in the red dashed line) through six tangentially directed slots. The radius

of the annular channel diminishes in the flow direction so that the converging vortex experiences an increase in angular velocity due to momentum conservation. The flow rate into the DRILL device may be as large as a few standard liters per minute. In Gen 3 DRILL, the swirling flow exits from the 1 mm diameter nozzle concentric with the electrospray capillary positioned in the centre, allowing for co-axial introduction of charged aerosol into a vortical flow. The vortex generator nozzle is axially aligned with the suction tube of the MS inlet at a distance a few millimetres away. In this configuration, electrosprayed charged droplets are subjected to the combined effects of the vortical flow and the suction flow into the MS inlet and the flow behavior and charged droplet transport can be studied as a function of the flow rate and distance between the gas source and sink. All fundamental electrohydrodynamic studies presented in Chapter 2 and 3 were performed using this flow arrangement of Gen 3 DRILL device.

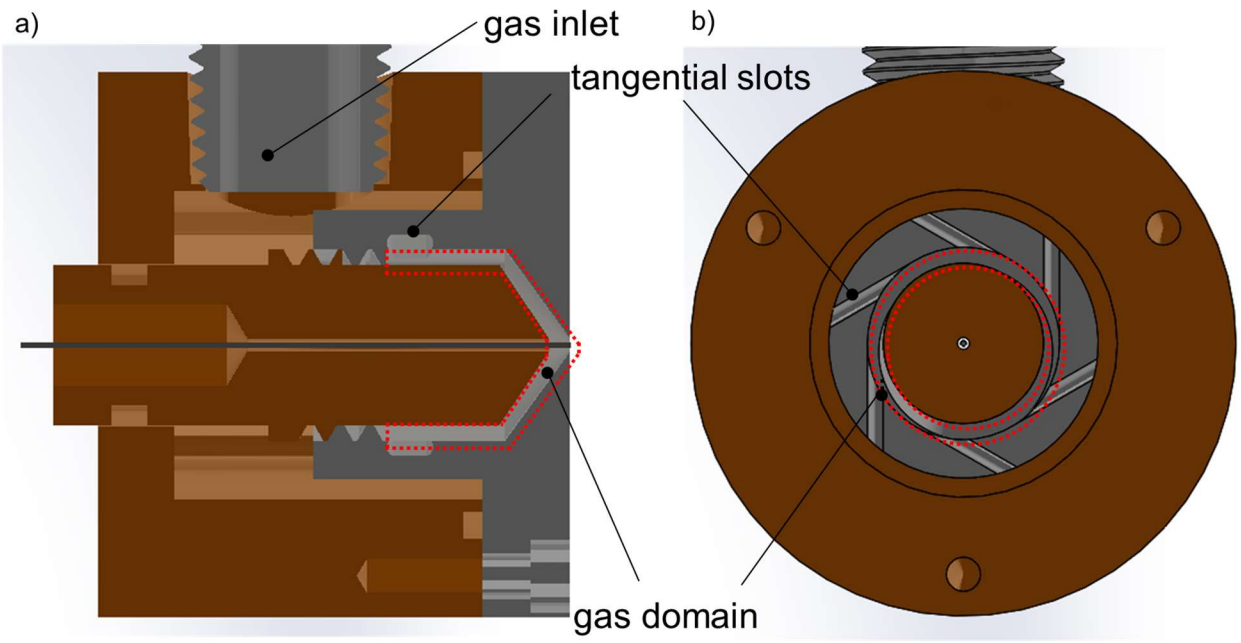


**Figure 1.6. Schematic of the Gen 3 DRILL cross sectional views. The annular fluid domain in which a vortical flow is created is enclosed by the red dashed line. The side view (a) and the front view (b).**

## 1.4 Research objectives

As illustrated in Figure 1.7, the objective of the work presented in this dissertation is to increase the understanding of the behavior of electrosprayed charged droplets via complimentary theoretical and experimental studies focused on:

1. Ability to exploit electrohydrodynamics to manipulate the behavior of electrosprayed charged droplets and, in particular, to assess the spatial size distribution of the droplets and droplets' fate in an ESI plume subjected to external vortical gas flow.

2. The effects of a vortical gas flow on the electrospray aerosol separation as a function of the charged droplet size and charge density and its implication on the spatial size distribution in an electrospray plume.
3. Gas dynamics of coupling between a vortical flow and suction flow and its impact on electrosprayed droplet transport and ion transmission efficiency

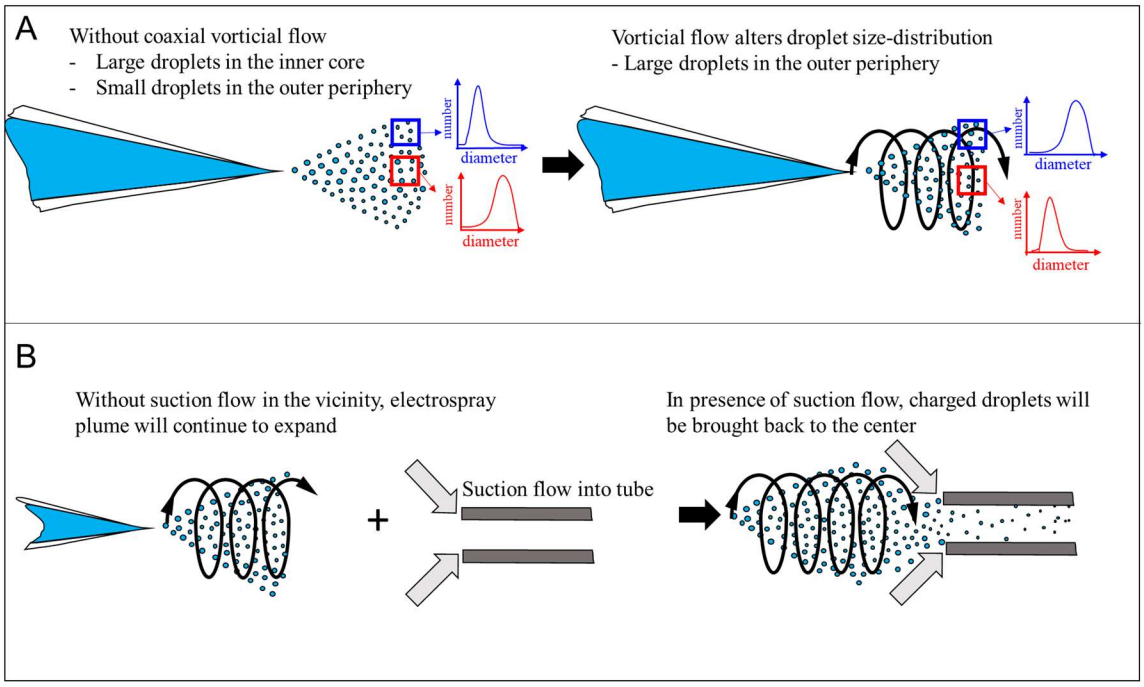


**Figure 1.7. Thesis hypotheses on the effect of a vortical flow on (A) the charged droplet distributions as a function of the droplet size and (B) and aerodynamic coupling to the suction flow and impact to droplet transport and ion transmission. These fundamental results have immediate implications on design of high efficiency DRILL interface for improved sensitivity of ESI-MS detection demonstrated in this thesis via bioanalytical application case studies.**

The research has been performed via a complementary theoretical (modeling and simulations) and experimental approach. Multiphysics modeling and simulations allow prediction of the flow motion and the electric field that impose forces on charged droplets resulting in prediction of droplet dynamics in vortical flow (Objectives 1 and 2).

Experimental flow visualization and supporting electrospray ion current transmission measurements provide both the model validation data and new insight into the effect of flow structure and interactions between the swirl and the suction flows on charged droplet behavior. Simulation results combined with experiments presented in this dissertation provide new understanding of the collective behavior of charged droplets subjected to hydrodynamic conditions characterized by a vortical flow coupled to suction into the MS inlet (Objective 3). The resulting predictive capabilities and engineering intuition provides valuable input and analytical tools for DRILL interface design and operation as part of high performance ESI-MS bio-analytical workflows.

## 1.5 Dissertation Overview and Organization

The vortical ESI-MS interface, DRILL, presents a unique opportunity for significant sensitivity improvements of mass spectrometric analysis as a swirling gas flow induces a shift in droplet trajectories and fates of electrosprayed charged droplets that vary in size and charge. Exploiting this gas dynamics and space-charge droplet interactions, DRILL rejects large primary droplets from transmission into the suction interface, resulting in substantial reduction of solvent-dominant chemical noise. Instead, improvements in capture of small progeny droplets are made possible by DRILL vertical flow, leading to efficient transfer of small droplets and dry analyte ions towards the MS intake for improved sensitivity of analyte detection.

Although vortical flow has been previously used in particle separation/sorting devices [51, 52], its behavior in conjunction with charged droplets in multiphase flow with strong electrodynamic interactions (both due to externally applied electric fields and

charged droplet induced fields) has been unexplored prior to this work. Further, the presence of the coupled suction flow adds an important novel aspect to this work, not only scientifically interesting but also practically useful in applications of complex multiphase flows.

This dissertation is organized as follows. Chapter 2 reports on model development and electrohydrodynamic simulations of charged droplet transport for different gas flow configurations. Combined effects of flow and electric fields on charged droplet dynamics are described. A proxy droplet population consisting of two droplet sizes (representative of primary/large and progeny/small droplets in a typical electrospray plume) is used to assess the behavior of different subsets of droplet population subject to imposed gas flow. Comparison is made among the typical electrospray behavior without any forced gas flow, vortex-free gas jet assisted electrospray, and vortical-jet assisted electrospray. Dependence of droplet trajectories on the droplet size and the resulting separation effects are described. In addition, the effect of varying swirl vorticity on behavior of small and large charged droplets is investigated. Simulation results are compared to experimental ion current measurements reaching the fundamental conclusions about the multiphase charged aerosol transport in vertical flow and providing recommendations relevant to DRILL device applications in ESI-MS.

In Chapter 3, combined effects of vortical flow and flow suction are explored using optical visualization of flow coupling and flow-droplet interactions at the conditions relevant to use of DRILL interface in ESI-MS. Parameters which affect the flow interactions have been comprehensively evaluated, including (1) the relative flow rate of the vortical flow to that of the flow suction, (2) the size of the vertex-generating annulus

relative to diameter of the suction intake aperture, and (3) the distance of the vortical flow source to the suction aperture (flow sink). The results establish the fundamental understanding of the topologically complex, interacting flow behavior, as well as quantitative guidance for the DRILL design and operating parameters (supplied flow rate, vortex generator annulus diameter, distance to MS droplet/ion extraction inlet). The effects of flow interactions are also mapped onto the experimental measurements of ion current transmission with conclusions having direct impact of improved sensitivity and alternative operating modes of DRILL ESI-MS operation.

Chapter 4 focuses on engineering design aspects and bioanalytical evaluation ESI-MS case studies of different DRILL configurations. Coaxial-flow and cross-flow arrangements of the electrospray capillary and vortical flow are critically compared in terms analytical performance (sensitivity/limit of detection and ion throughput) as well as robustness/stability of operation.

Chapter 5 summarizes the results of DRILL application to mass spectrometric analysis of peptides, protein mixtures and fluorinated polymers with varying surface activity to assess the significance of hydrophobic bias and indirectly evaluate the droplet population preferentially transmitted by DRILL. Improvements in ion abundance, signal-to-noise ratio, and a shift in peak distributions are shown to be in agreement with fundamental understanding of charged electrospray aerosol behavior revealed by simulations (Chapter 2) and trends exhibited in ion current transmission measurements (Chapter 3).

In Chapter 5, the dissertation concludes with a summary of key contributions of this work to fundamentals of topologically complex (vortical gas stream coupled to point suction) multiphase flows of charged aerosols and optimal design and operation of the novel atmospheric pressure droplet/ion transmission interface, DRILL, with potential for a broad range of applications from bioanalytical mass spectrometry to ion soft landing functional nanomaterial deposition for energy conversion and storage technologies.

# CHAPTER 2. ELECTROHYDRODYNAMICS OF ELECTROSPRAYED CHARGED DROPLETS IN A VORTICAL FLOW

Understanding the electrohydrodynamics of ion and charged droplet transport in the atmospheric pressure region subjected to vortical flow and with an imposed electric field is essential for successful enhancement of droplet/ion transmission into the MS inlet via improvements in DRILL design and operation. ESI-MS sensitivity is closely related to the size and number of droplets/ions that reach the suction inlet of the MS, and also to efficient desolvation and formation of gas-phase analyte ions. Therefore, prediction of electrosprayed droplet behavior accounting for interactions with gas flow and external (due to imposed electric potential difference) and internal (due to quasi-electrostatic space-charge interactions within the aerosol plume) electric forces is critical for developing design ideas that enhance transmission and desolvation efficiency.

ESI processes result in multi-modal droplet size distributions with three groups: (1) large parent droplets with lower charge density that originate from the jet breakup at the conical liquid meniscus, (2) small offspring droplets which are highly charged and produced from the large parent (primary) droplets from fission after initial solvent evaporation, and (3) fully "dry" gas-phase ions that arise from small highly charged droplets via charge residue or ion evaporation mechanisms. A common assumption is that the initial size of electrospray droplets is uniform, although a bi-modal distribution in the cone-jet spraying regime has also been observed [53]. Theoretical and experimental equations correlate the initial droplet diameter with the liquid flow rate and the liquid

properties (e.g., electrical conductivity, surface tension) [8, 9]. After formation by ES, a primary droplet shrinks via solvent evaporation (without loss of charge), until its radius drops to the critical size defined by the Rayleigh limit, and the droplets become unstable and break up, causing the primary (parent) droplet to produce up to 20 small highly charged droplets [11], as illustrated in Figure 2.1. These small offspring droplets take away only a small amount (~2%) of the mass but a large amount (~15%) of the charge from the parent droplet [11]. The diameter of offspring droplets generated via this asymmetrical fission event is estimated to be $1/10^{th}$ of the diameter of the parent droplet [18] with much greater charge density (~30 fold increase). Both parent and offspring droplet populations continue to experience solvent evaporation and fission events, yielding a heterogeneous electrospray plume of droplets with varying size and charge.

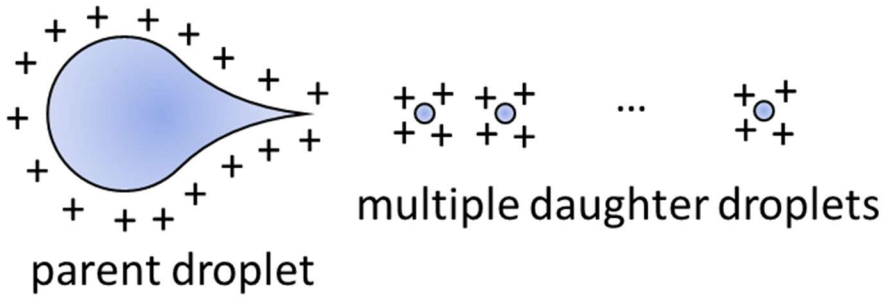


**Figure 2.1.Schematic of the parent droplet undergoing deformation due to imbalance of electrostatic forces and Coulombic fission with generation of daughter droplets**

This chapter presents an electrohydrodynamics model and simulation results of electrosprayed charged droplet transport with a focus on the understanding of charged droplet behavior in a vortical flow as a function of droplet size. The chapter starts by presenting the model for simulation of the vortical flow fields and hydrodynamics of droplet-gas interactions. The governing transport equations and the scheme by which the

external electric field is coupled with charged droplet dynamics (space charge effects) are presented. This is followed by discussion of the model application to predicting behavior of a bi-modal droplet population consisting of large primary droplets and small offspring droplets subject to varying hydrodynamic conditions: (1) suction only, (2) a vortex-free jet coupled to suction (representative of typical ES with an auxiliary gas flow), and (3) a vortical jet coupled to suction (representative of ES with DRILL). The results demonstrate a strong dependence of droplet behaviors and trajectories on the droplet size and flow fields and explains the ability of the vortical flow to separate droplets of different size. The model is applied to a wide range of droplet size populations (200 nm~10 $\mu m$) to investigate the relative importance of the competing forces (electric and drag) as a function of droplet size. Finally, the model predictions of ion current transmission efficiency based on the final droplet distributions for a given droplet size are compared with results of experimental ion current measurements at the suction capillary. The experimental results support the utility of the EHD model for studying dynamics of charged droplet/ ion subjected to interplaying gas and electric fields.

## 2.1 Review of Current Understanding of Electrosprayed Charged Droplet Transport

Understanding the electrohydrodynamics of electrosprayed charged droplets enables prediction of their transport between the source (electrospray capillary) and sink (counter-electrode or extraction capillary) as a function of droplet size. The electrohydrodynamics of charged droplets in an electrosprayed aerosol plume has been investigated experimentally [11, 53, 54] and more recently computationally [55-57]. Gomez and Tang experimentally measured the size and charge distributions that correlate

the charge density with the droplet size: The charge density decreases with increasing droplet size. The work also presented photographs of parent droplets undergoing fission [11] with an elongated tail from which very small offspring droplets eject. The study shed light on some fundamental aspects of electrospray droplets: the validity of the Raleigh stability limit in good agreement with the experimental correlation and important features of droplet fission (e.g., parent droplet deformation, relative size ratio between parent and offspring droplets, number of offspring droplets produced per fission event).

Nemes et al. [53] measured the size, velocity and radial displacements of electrosprayed droplets produced at a micro flow rate (30 $\mu$L/hr) used in conventional electrospray. The measurements were acquired ~13 mm downstream of the ESI emitter, probing ES droplet dynamics in a limited volume of air (~200 $\mu$m in width). Despite limited visibility beyond the probe zone, no detection of smaller droplets in the central probe region suggests information about the spatial droplet distributions including size segregation and greater radial displacements of smaller droplets due to space charge effects.

Use of polarity-sensitive fluorescence spectroscopy combined with a droplet sizing capability [54] enabled profiling of droplet size distributions and solvent fractionation in a spray plume. The results confirmed that the radial heterogeneity of the solvent fractionation across the electrospray plume is correlated with droplet size distributions. The solvent composition in the inner core of the plume closely matches that of the original solution infused. This is attributed to predominant occupancy of large primary droplets with low surface area relative to the volume leading to gradual solvent evaporation. On the other hand, increased fractionation of less volatile solvent (e.g., water) is observed in the periphery of the plume due to small offspring droplets with greater evaporation rate of

volatile organic solvent. The experimental measurements provided a better understanding of physical and chemical properties of droplet size populations in an electrospray plume.

In addition, various experimental studies reveal important factors for charged droplet/ion transport. For example, greater electrospray current results in greater radial plume expansion leading to reduced transmission efficiency of charged droplet/ion into a MS [22, 58]. Some ESI-MS geometric parameters (e.g., ESI emitter-MS inlet distance, inlet inner diameter and shape) [34, 42] play a role in determining electrospray droplet/ion transmission. However, in many experimental setups, these parameters are often interrelated and hard to decouple. Numerical simulations are advantageous in the sense that they allow for assessing the role of each parameter independently without affecting others, which provides insights into MS interface design and performance optimization. More importantly, the results of numerical modeling provide a temporal and spatial evolution of ion/ charged droplet motion which cannot not be acquired via experimental measurements typically observed at discrete locations with small probe volume.

The first simulation work by Ganan-Calvo et al. [56] described different aspects of ESI droplet dynamics by solving the momentum equation for each emitted droplet with consideration of the space charge effect (due to mutual repulsion between charged droplets) and the drag force (due to fluid resistance to droplet motions). The numerical results were compared to experimental measurements of the droplet size distributions and velocities and showed a good agreement. The Lagrangian model of electrosprayed droplet size populations demonstrated several features of electrospray plumes including (1) droplet segregation by size and (2) reduced velocities for droplets at greater radial distance from the plume centerline [56]. The droplet diameters considered for this study were above

$10\mu m$, which corresponded to the size of primary droplets that can be obtained using very high flow rates. Wilhelm et al. [23] adopted the droplet transport model developed by Ganan-Calvo et al. [56] to simulate electrospray consisting of a bimodal size distribution (24 $\mu$m and 2 $\mu$m in diameter) for film deposition on a heated substrate. In addition, droplet evaporation via mass and heat transfer was considered leading to reduction in droplet size during the flight. However, the simulated droplet spatial distribution at the substrate reveals little effect of evaporation on droplet transport. Rietveld et al. [57] considered a smaller diameter droplet range (1~10 $\mu m$) but ignored space charge effects, which are critical to the capturing radial motion of electrosprayed droplets in a plume. The studies, while having some limitations in their treatment of different aspects of electrospray phenomena and charged droplet transport in gas environment, provided a fundamental framework for analyzing other spray configurations.

Recent simulation studies investigated ion trajectories in a gas flow assisted configuration under atmospheric pressure. Simulations of ion (70 Da and 455.6 Da) motion in gas flow with varying gas flow rate predict ion transport phenomena with accuracy using the drag model with a slip correction factor given the small ion size [55]. Comparisons of the magnitude between interplaying forces (electric and drag forces) confirm that the forces influence ion transport with equivalent importance. Simulations of ion trajectories in differential pressure stages (atmospheric to high vacuum) [59] were demonstrated employing different simulation methods (drag model and ion-gas collision model) suited for the pressure regime. The simulation work of ion trajectories in gas flow suggests a potential for extension of the model to prediction of charged droplet trajectories subjected to a complex flow field.

Several commercial software packages are available with various levels of capabilities to simulate charged droplet/ion transport. In SIMION, tracking of charged particles/ions is implemented in electric and magnetic fields imposed by a configuration of electrodes with prescribed voltages and conditions such as RF time-varying electric field. The software is suitable for analyzing charge transport in vacuum environment, e.g., inside the mass spectrometer, but is not capable of hydrodynamic simulations. For simulations of electrohydrodynamics, one needs to couple SIMION predictions with an external CFD solver to calculate the flow fields and import the computed values for flow variables. For this reason, SIMION is frequently used to characterize ion transmission in perfect vacuum. On the other hand, ANSYS Fluent is capable of modeling complex flow fields and has been used for droplet/ ion trajectory simulations at atmospheric pressure [55, 60]. In ANSYS Fluent, electric field simulations are performed using the user-defined scalar (UDS) formalism with custom-written user-defined functions (UDF) by the user [61]. Wang et al [55] implemented the particle-in-cell (PIC) method [62] in a 2D axisymmetric model to simulate space charge effects in a mode of continuous charged droplet injection, but the convergence in 3D can be quite challenging when using ANSYS Fluent. The charged particle tracing module in COMSOL Multiphysics, a commercial finite element software package, features a bidirectionally (to other scalar fields) coupled solver for electrostatics and provides an efficient framework for charged droplet/ion dynamics simulations under combined effects of gas flow and electric fields with consideration of space charge effects [63]. A great advantage of this solver is that a quasi-steady state solution of charged droplet trajectories can be obtained mimicking a continuous droplet

injection mode defined by the number of charged droplets ejected per unit as given by the specified spray current as a boundary condition.

## 2.2 Electrohydrodynamic Modeling of Electrosprayed Charged Droplet Transport

### *2.2.1 Simulation Procedure*

Numerical modeling incorporates governing physics for prediction of the flow and electric fields and the resulting droplet dynamics. In the situation considered, the volumetric flow rate of a surrounding gas flow (in standard liters per minute) is a few orders of magnitude greater than that of the sample liquid (microliters per minute). Therefore, the electrospray is modeled in a sparse two-phase flow, allowing for simplifications in the computation of flow fields – that is the gas velocity is decoupled from the droplet dynamics (i.e., gas flow affects droplet motion, not vice versa). Multiple simulation domains are used to solve decoupled fields in a computationally efficient manner (Figure 2.3). Three simulation domains were constructed to compute the flow field: The first 3D flow model was created based on the interior of the vortex generator structure described in Figure 1.6 and used to predict the velocity field inside the vortex generator and at the annulus/nozzle from which the swirling flow exits. The exit velocity from the vortex generator nozzle was used as the inlet boundary condition of a 2D axisymmetric simulation domain which encompasses the atmospheric pressure region between the electrospray needle and the suction tube, which emulates the mass spectrometer inlet and 3 mm into the MS inlet capillary (Figure 2.2). In all surfaces with prescribed flow, the velocity inlet boundary condition is used and all exits and far-field are assigned the pressure outlet boundary conditions to obtain the steady-state velocity field by solving the laminar, incompressible

Navier-Stokes equations. The flow field from the 2D axisymmetric model was mapped into a 3D domain in which droplet trajectory simulations combined with electrostatics were implemented. Figure 2.2 shows the velocity field in the combined with electrostatic simulation domain. The color scale indicates the swirl velocity resulting from the gas flow rate $\dot{Q} = 1.3$ L/min ($2.17\times 10^{-5}$ m$^3$/s) entering the vortex generator.

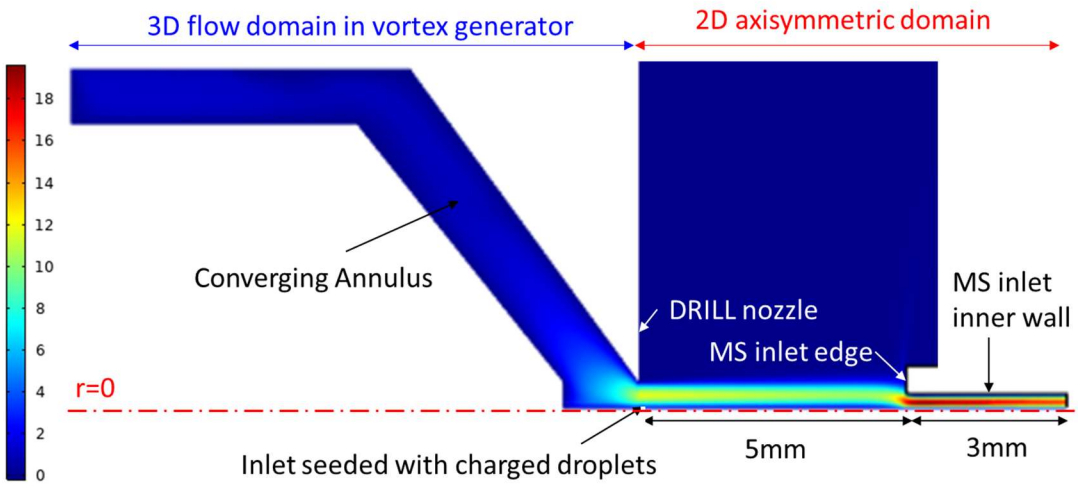


**Figure 2.2. Profile of the fluid domain consisting of the vortex generator structure, the atmospheric pressure region between the electrospray nozzle (source of charged droplets) and suction tube emulating the mass spectrometer inlet, and 3mm ID capillary into the vacuum domain of the mass spectrometer.**

Once the flow field was simulated, the electric field was obtained by solving Poisson's equation with the spatially distributed volumetric charge density of injected droplets acting as the source term. A charged droplet population of varying size and charge was introduced into a simulation domain from a small area equivalent to the cross-sectional area of the electrospray capillary tip (20 $\mu$m ID). Droplet motions and trajectories in Lagrangian domain were obtained from the combination of imposed gas flow and electric fields (with incorporation of space charge effects). The predicted charged droplet

trajectories result in updated space-charge density distributions thus altering the predicted electric field; so an iterative procedure that alternates between the computation of droplet trajectories and the electric field was performed to reach a self-consistent quasi-steady state solution via hybrid Lagrangian and Eulerian simulations. For all simulation results presented in the current chapter, each droplet in the sample droplet population on release from the inlet (electrospray tip) was treated as a representative droplet such that its trajectory is followed by droplets released subsequently at a frequency based on the spray current, forming a string of droplets in Eulerian coordinates. This way, a stationary solution of the electrical potential field and the droplet trajectories was obtained, representing the steady-state droplet behavior. A schematic of the entire simulation procedure is shown in Figure 2.3. All simulations presented in this chapter were performed using COMSOL Multiphysics.

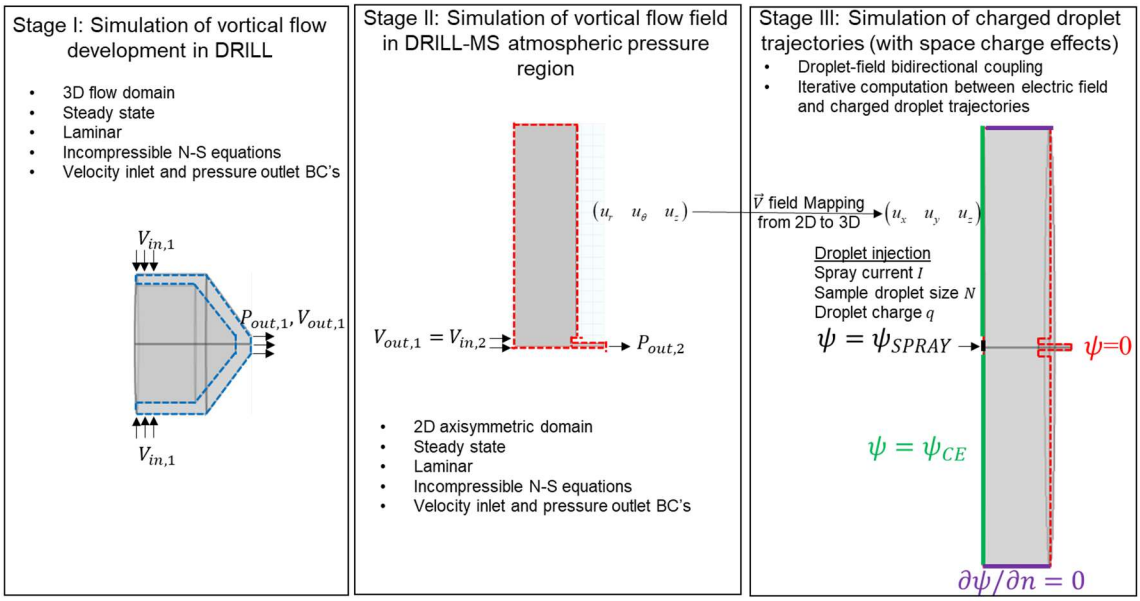


**Figure 2.3. Schematic of the charged droplet transport simulation procedure**

### *2.2.2 Electrohydrodynamics and Charged Droplet Transport*

The laminar vortical gas flow field inside the DRILL interface and the atmospheric pressure region between DRILL-MS is governed by Navier-Stokes equations of motion for an incompressible fluid,

$$\rho\left(\vec{u}\cdot\nabla\right)\vec{u} = -\nabla p + \nabla\cdot\left[\mu\left(\nabla\vec{u} + \nabla\vec{u}^{T}\right)\right] + \vec{F} \tag{2.1}$$

$$\nabla\cdot\left(\vec{u}\right) = 0 \tag{2.2}$$

where $\rho$ is the fluid density, $\vec{u}$ is the velocity vector, p is pressure, $\vec{F}$ is a net body force vector, and $\mu$ is the dynamic viscosity of the fluid. Electrosprayed charged droplets were modeled as point particles with constant charge, electrostatically interacting with the electric field. Droplets were assumed to be spherical, and no change in droplet size due to evaporation effects and Coulombic fission were considered. The 3D Lagrangian modeling of droplet dynamics is based on the Newton's second law of motion expressed as

$$\frac{d}{dt}\left(m_d\frac{d\vec{r}}{dt}\right) = \vec{F}_D + \vec{F}_E \tag{2.3}$$

where $m_d$ is the droplet mass, $\vec{\boldsymbol{F}}_D$ is the drag force, and $\vec{\boldsymbol{F}}_E$ is the electric force. The drag force is experienced during droplet flight in the flow field formed by the interface-generated vortical flow paired with suction into the MS inlet in the vicinity.

$$\vec{F}_D = \frac{1}{\tau_d}m_d\left(\vec{u} - \vec{v}\right) \tag{2.4}$$

Here, $\vec{v} = \frac{d\vec{r}}{dt}$ is the droplet velocity vector, and $\tau_d$ is the droplet relaxation time. The Schiller-Naumann drag correlation [64] (for $Re \leq 1000$) expresses $\tau_d$ as

$$\tau_d = \frac{4\rho_d d_d^2}{3\mu C_D \,\mathrm{Re}} \tag{2.5}$$

$$C_D = \frac{24}{\mathrm{Re}}(1 + 0.15\,\mathrm{Re}^{0.687}) \tag{2.6}$$

where $\rho_d$ is the droplet density, $d_d$ is the droplet diameter, Re = $\rho|\vec{u} - \vec{v}|d_d/\mu$ is the Reynolds number based on the droplet diameter and relative particle-to-gas velocity. The droplet diameters considered for the model vary between sub-micrometer and ten micrometers. The simulated Reynolds numbers were on the order of 0.1 to 10, and hence, use of this drag correlation is appropriate. For droplet diameters $d_d < 5\ \mu m$ comparable to the gas mean free path $\lambda$, slip occurs, and the drag force $\vec{F}_{D,S}$ on small droplets is modified by the Cunningham correction factor $C_C$ [65] given by,

$$\vec{F}_{D,S} = \frac{\vec{F}_D}{C_C} \tag{2.7}$$

$$C_C = 1 + \frac{2\lambda}{d_d}\left(1.257 + 0.4e^{-\frac{1.1 d_d}{\lambda}}\right) \tag{2.8}$$

$$\lambda = \frac{\mu}{p}\sqrt{\frac{\pi R_u T}{2M}} \tag{2.9}$$

where p is the pressure, $R_u$ is the universal gas constant, T is the temperature, and M is the molecular weight. The mean free path for air at STP of 68 nm is used for the simulations presented in this dissertation.

A droplet carrying charge $q$ experiences an electric force while traveling in the electric field $\vec{E}$.

$$\vec{F}_E = q\vec{E} \tag{2.10}$$

The electric field $\vec{E}$ is obtained in terms of the electrical potential $\psi$.

$$\vec{E} = -\nabla\psi \tag{2.11}$$

The electrical potential field is governed by the Poisson's equation expressed as,

$$\nabla \cdot (\varepsilon_0 \nabla\psi) = -\rho_S \tag{2.12}$$

where $\varepsilon_0$ is the permittivity of vacuum, $\psi$ is the electrical potential, and $\rho_S$ is the volumetric charge density. Each charged droplet injected at t=0 was treated as a model droplet whose path is reproduced in space by successive droplets released at the frequency $f_{rel,}$

$$f_{rel} = \frac{I}{qN} \tag{2.13}$$

where $I$ is the spray current, and $N$ is the size of the droplet population injected at t=0. For a mesh element $j$ with volume $V_j$, the average space charge density $\rho_j$ within the mesh element is obtained by integrating the following equation.

$$\frac{d\rho_j}{dt} = \frac{1}{V_j}\sum_{i=1}^{m} f_{rel} q_i \tag{2.14}$$

Here, the $q_i$ is the charge of the $i$th model droplet within the mesh element and $m$ is the total number of the model droplets present in the mesh element. For any given droplet diameter, the droplet charge $q$ was set such that $q$ takes a value between 70% to 100% of the Rayleigh stability limit expressed in Eq (2.13). In the right box of Figure 2.3. Schematic

of the charged droplet transport simulation procedure, the indented boundary on the right side represents the wall of the suction tube/MS inlet (550 $\mu m$ ID, 1/16" OD) and is prescribed a zero potential, $\psi$=0. The electrospray capillary tip is represented by a circular disk area (30 $\mu m$ diameter) located in the center of the left boundary, assigned a spray potential $\psi = \psi_{SPRAY}$ and is concentric with the nozzle from which swirling flow emanates. The center of the electrospray capillary tip is aligned with that of the suction tube/MS inlet. The rest of the left boundary is assigned a specified potential $\psi = \psi_{CE}$. The zero-gradient of the electric potential $\partial\psi/\partial n = 0$ is applied normal to the cylindrical boundary in far-field (2 cm) from the central axis.

### *2.2.3 Assumptions for Model Formulation*

Direct emission of charge/ions from droplets requires significant input of thermal energy. Compared to the surrounding air, the temperature of an expanding electrospray plume is lower by 10 to 30K [24], attributed to droplet cooling due to solvent evaporation. This modest temperature difference and relatively low heat transfer coefficient in gas phase cannot provide sufficient thermal energy to cause direct ion desorption from droplets. Thus, in all simulations the droplet charge was assumed to stay constant.

In addition, charged droplets were assumed to be non-evaporative spheres, and no change in droplet size was considered over the course of the flight time. The assumption holds based on that the vapour in surrounding air quickly reaches the saturation pressure substantially slowing down evaporation of electrosprayed droplets [56]. For any droplet at 80% Rayleigh charge limit, the droplet needs to shrink to 86% of the original droplet size for the first Coulombic fission event to occur. Considering the large droplet carrier flow

velocity, the droplet completes its flight about in 100 $\mu s$. The rate of droplet evaporation can be either heat transfer or mass transfer limited. The temporal evolution of the droplet size is evaluated using the mass-transfer-limited case described by Abramzon and Sirigano [66].

$$\dot{V}_{ev,d} = -\pi d_d \frac{\rho_g}{\rho_d} D_g Sh_d \ln\left(\frac{1-y_\infty}{1-y_s}\right) \tag{2.15}$$

where $\rho_g$ is the average gas phase density, $\rho_d$ is the droplet density, $D_g$ is the diffusion coefficient, $y_\infty$ is the mass fraction of the solvent in the far-field away from the droplet, $y_s$ is the mass fraction of the solvent at the droplet surface, and Sherwood number $Sh_d = 2 + 0.552 Re_d^{1/2} Sc_g^{1/3}$. By the time a 1 $\mu m$ diameter droplet reaches the MS inlet, the droplet will have shrunk to 72% of the initial droplet size, which means it may have experienced at least one Coulombic fission event during the flight time. For the 1 $\mu m$ droplet, one can expect about 30% droplet size reduction within the residence time. For larger droplets, the change in droplet size is less given the same time. For example, a 2 $\mu m$ droplet experiences only 8% size reduction. A few fission events do not lead to significant decrease in the droplet diameter considering that each fission event results in only 2% loss of the initial mass [20]. In conclusion, while solvent evaporation is primarily responsible for the droplet size reduction, for the relatively short droplet transit times from the source (electrospray tip) to the sink (suction tube/MS inlet) considered in this work makes it reasonable to neglect a relatively small shrinkage of droplets without risk of losing an essential physical features of size-dependent separation of droplets in vortical flow when their initial sizes differ by an order of magnitude or more.

Comparisons of the magnitude of interplaying forces acting on different droplet size populations were performed to determine the relative importance between the drag, electric, and Brownian forces. Two droplet sizes are considered: 200 nm and 2 $\mu m$. Figure 2.4 displays the magnitude of forces per unit mass on two size droplet populations at various locations from the ESI tip (z=0) toward the MS inlet (z=5 mm). For the two droplet size populations (200 nm and 2 $\mu$m diameter), the drag and the electric forces are predominant. Particularly, the two forces are at least 2 orders greater than the Brownian force for 2 $\mu$m droplets in both axial and radial directions (Figure 2.4c and d). For 200 nm droplets, Figure 2.4b suggests that the Brownian force may play a role in the radial motion. Therefore, the Brownian force was considered for submicron droplets in a few limited cases. The simulations presented in the remainder of the chapter considered the drag and electric forces unless otherwise noted.

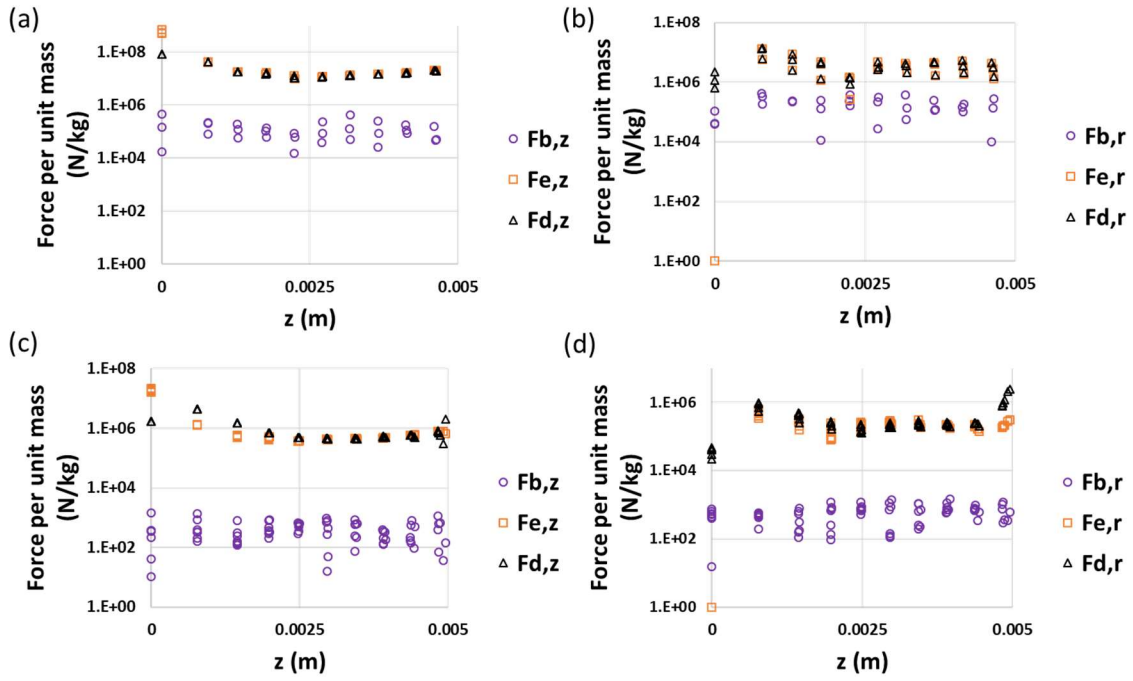

**Figure 2.4. Axial distribution of force magnitudes per unit mass on droplets. Forces (Brownian, electric and drag) acting on 200 nm droplets - (a) axial component and (b) radial component; Forces (Brownian, electric and drag) acting on 2 μm droplets - (c) axial component and (d) radial component.**

### *2.2.4 Simulation and Analysis*

The droplet motion and fates are the result of the combined effects of the flow field and the electric field. In the given DRILL swirl generator geometry, the flow field was simulated for varying gas flow rate. The suction flow rate was set such that it matches a typical suction rate into the MS inlet (1.1~1.6L/min). This way, the DRILL interface generated flow can be metered such that it is fully transmitted into the MS inlet (perfect aerodynamic coupling). The focus of this study is to determine dependence of droplet trajectories/destination and droplet separation on (1) the flow field and velocity magnitude, (2) the droplet size, and (3) the swirling intensity. The simulation results were compared to and validated by the experimental measurements of ion current transmitted into the MS inlet.

#### 2.2.4.1 Simulation of Velocity Field

The DRILL swirl generator geometry used for flow simulations is described in Figure 1.6. The gas flow rate $\dot{Q}$ entering the DRILL device was varied from 0.65 L/min to 1.3L/min. Flow simulations were performed with $CO_2$ as a carrier gas, as it is the gas that was used in ion current measurements and schlieren visualization experiments to be used for comparison. Figure 2.5 shows the swirl velocity profile across the DRILL nozzle radius as a function of supplied gas flow rate. As expected, the swirl velocity increases with increasing flow rate. This is due to reduced boundary layer effects in the annular channel

with greater entering velocity of gas, creating a uniform velocity profile downstream close to that at the entrance.

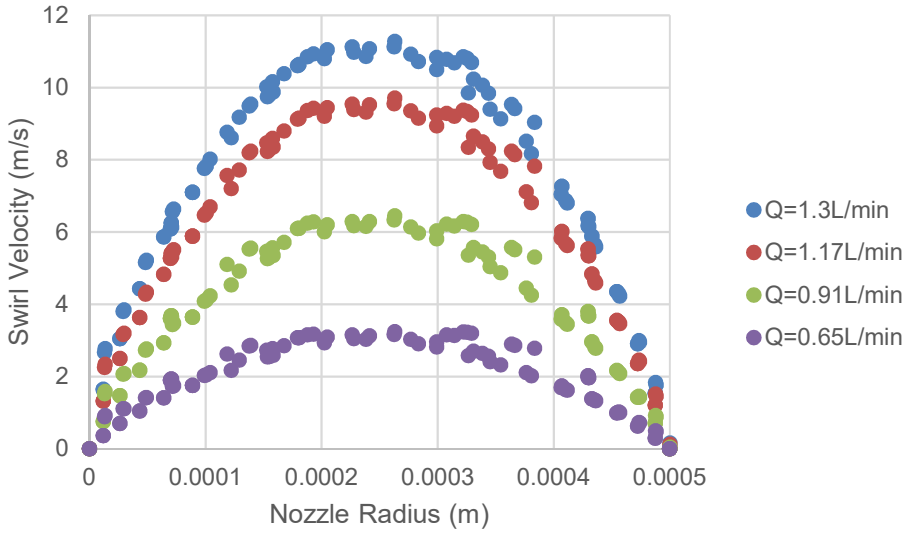


**Figure 2.5. Simulated swirl velocity at the DRILL nozzle/exit of vortex generator as function of the varying flow rate**

The relative magnitude of the swirling velocity to the axial stream velocity is investigated as a function of the flow rate. The intensity of the swirling flow is described by the swirl number *S* defined as [67],

$$S = \frac{\int r u_\theta \vec{u} \cdot d\vec{A}}{\bar{R} \int u_z \vec{u} \cdot d\vec{A}} \tag{2.16}$$

Here, $r$ is the radial coordinate, $v_\theta$ is the swirl tangential velocity, $v_z$ is the axial velocity, $\vec{u}$ is the velocity vector, $\bar{R}$ is half the nozzle diameter (hydraulic radius). Figure 2.6 plots the simulated swirl number at the DRILL nozzle/vortex generator exit (blue) and the suction tube/MS inlet (red) as a function of the gas flow rate. As shown in Figure 2.6, increasing gas flow rate accompanies increase in swirl number at the DRILL nozzle (blue),

indicating that given any increase in flow rate, increase in angular momentum is greater than that of the axial momentum.

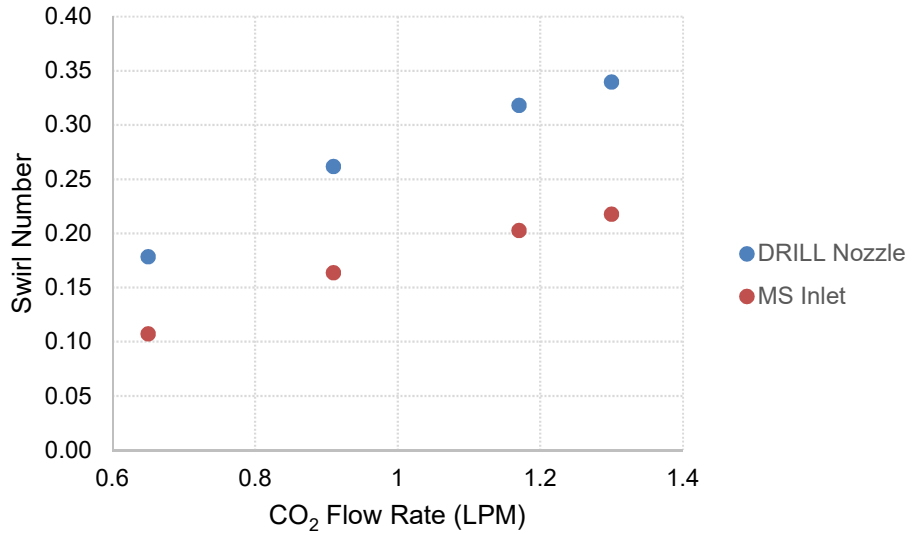


**Figure 2.6. Swirl number with varying gas flow rate at DRILL nozzle and MS inlet**

For all simulations, the separation distance between the swirl nozzle and the MS inlet suction is 5 mm, which ensures that for the entire range of gas flow rates the assumption of laminar flow remains valid (based on schlieren visualization results presented in section 3.2.2.3). It also ensures complete hydrodynamic coupling between the source/jet gas flow and sink/suction tube based on the visualization studies. As described in Figure 2.2, an otherwise expanding vortical flow entering into the confines of MS inlet result in two implications on the coupled flow structure in the DRILL-MS interface domain: (1) The suction limits the radial expansion of the swirling jet (initially 1mm matching the nozzle diameter). At the axial distance of 4.5 mm from the nozzle, the jet coupled with the suction displays a 5 times smaller diameter (~ 2mm) compared to that of the freely expanding jet (~1 cm) without suction. Less expansion of the jet allows for

retention of the swirl velocity with minimum dissipation of the angular momentum until the flow reaches the MS inlet. (2) The MS inlet diameter (550 $\mu$m) is smaller than the nozzle diameter (1 mm) and therefore the swirl velocity increases as the jet is constricted near the entrance of the MS inlet due to the angular momentum conservation. Even though the vortex structure is well preserved from DRILL nozzle to MS inlet and the swirl velocity at the inlet is greater than that at the nozzle, this velocity increase does not result in higher swirl numbers than those present at the DRILL nozzle. This is due to the fact that the relative increase in the axial velocity (increase by a factor of ~4) is greater than that of the swirl velocity (increase by a factor of ~ 1.5). The intensity of the swirling flow represented by the swirl number is closely related to the ability of inertial effects to move larger droplets radially outward. The inertial effects are described by the centrifugal force $F_C$ and vary with the size of charged droplets in rotational motion.

$$F_C = \left(\frac{\pi}{6}\rho_d d_d^3\right)\frac{u_\theta^2}{r} \tag{2.17}$$

Here, $\rho_d$ is the droplet density, and $r$ is the radial position of the droplet relative to the axis of rotation. The outward inertia grows with the droplet diameter to the third power. Therefore, one can expect the inertial effects experienced by larger droplets to be much greater as compared to that experienced by smaller droplets. For example, primary electrosprayed droplets are larger in diameter by an order of magnitude compared to small offspring droplets. The outward inertia felt by those large parent droplets are 1000 times greater than that of small daughter droplets given the difference in size. Increase in the inertial effects follow the power law behavior for any increase in droplet size ($F_C \propto d_d^3$), which is relatively greater over that of drag ($F_C \propto d_d$) and electric forces ($F_C \propto d_d^{3/2}$). The

relative importance of the inertial effects increases with droplet size, causing these droplets to move out further radially from the axis of rotation. This results in separation of larger parent droplets from the stream of small daughter droplets. The outward inertia also depends on the rotational velocity $u_\theta$. Therefore, droplets in an intense swirling flow experience greater inertia in the outward radial direction.

Establishing sufficiently high swirl intensities is needed to create the inertial effects for efficient separation of larger droplets from the central region. In DRILL, an increase in the swirl intensity (or swirl number) can be achieved by an increase in the flow rate. To reach the maximum possible swirl number, one may continue to increase the flow rate into the DRILL interface. However, the flow rate entrained into the MS inlet $\dot{Q}_{Suction}$is not subject to change ($\dot{Q}_{Suction}$ is limited by the MS inlet ID and tube length), and increasing the swirling flow rate $\dot{Q}_{Swirl}$ to a value greater than $\dot{Q}_{Suction}$ is not considered in this study for several reasons (see flow visualization studies in section 3.2.2.3): (1) For $\dot{Q}_{Swirl}$>$\dot{Q}_{Suction}$, droplets are carried by drag away from the MS inlet by the excess flow; (2) For reproducible droplet separation effects, preservation of the laminar vortical flow structure is essential. The redundant flow that cannot be transmitted into the MS inlet develops turbulent flow features as it impinges on and bypasses the MS inlet.

Commercial mass spectrometers typically pump in ambient air at a rate between 1.1 to 1.6 L/min. In the following droplet trajectory simulations, the flow rate of $\dot{Q}_{Swirl}$=1.3 L/min ($2.17\times 10^{-5}$ $m^3/s$) was used as it allows for the maximum swirl intensity achievable for 100% flow transmission given the suction rate. The pressure outlet boundary condition was applied such that the swirling flow is allowed to leave the simulation domain only

through the outlet boundary. The cylindrical far-field boundaries were set to the no-slip wall condition to ensure that no flow exits other boundaries.

#### 2.2.4.2 Domain Size and Meshing for Droplet Trajectory Simulations

As indicated in Figure 2.9, a 3D cylindrical domain is created for droplet trajectory simulations. The effects of the size of the domain and the mesh on charged droplet fates were investigated, according to which justifications were made for selection of the computationally efficient domain size and meshing. The ion current, the rate of charged droplets (100 nm and 1 $\mu$m in diameter) arriving at different locations on the counter-electrode, is directly correlated to the droplet fates and used as a measure of sensitivity to the domain and mesh size.

Figure 2.7 compares the ratio of ion current collected by the suction tube (out of the total spray current) varying cylindrical domain sizes (2 cm, 4 cm, and 8 cm in diameter) and minimum mesh sizes (6 $\mu$m, 8 $\mu$m, and 16 $\mu$m). The "transmitted through the suction tube" portion of the ion current represents the fraction of charged droplets that is not lost to any electrode but hits the "outflow (off-tube) boundary" of the simulation domain. The remainder of the ion current is lost to the suction tube (either on the inner wall or near the corner of the inner diameter of the suction tube), resulting in the same droplet end fates. Final droplet distributions reveal that only a slight shift in the droplet (radial) position may cause the droplets to hit either the inner wall or the corner of the inner diameter of the suction tube differing only by a few microns in radial distance. Therefore, the "transmitted through the suction tube" portions of the ion current are compared between varying domain and mesh size. As shown in Figure 2.7 (a), the "transmitted through the suction tube" ion

current is lowest using the smallest domain size (2 cm in diameter) due to greater dispersion of droplets in the radial direction. In the smallest domain, the electrical potential rapidly decays toward the cylindrical boundary subject to the zero-potential gradient normal to the plane. This sharp gradient causes greater outward displacements of droplet within a smaller axial distance. On the other hand, the "transmitted through the suction tube" ion current ratio using the 4 cm and 8 cm diameter domains are comparable, indicating convergence. Moreover, the "transmitted through the suction tube" ion current is the important portion of the current that can potentially makes it into the end of the ion transfer capillary and impacts the mass spectrometric analysis. For the simulations presented in this chapter, the cylindrical domain in 4 cm diameter was used as it best represents the actual electrical condition in DRILL-MS.

Figure 2.7 (b) shows comparisons of the ion current transmission ratio varying minimum mesh size such that the number of mesh elements in the domain increases by a factor of 2 to 3. The "transmitted through the suction tube" portion varies little with decrease in minimum mesh size, showing convergence in the droplet end fates. The element size selected for the simulations discussed in the chapter corresponds to the most refined mesh size available in the built-in physics-controlled meshing functionality (The result is indicated as orange).

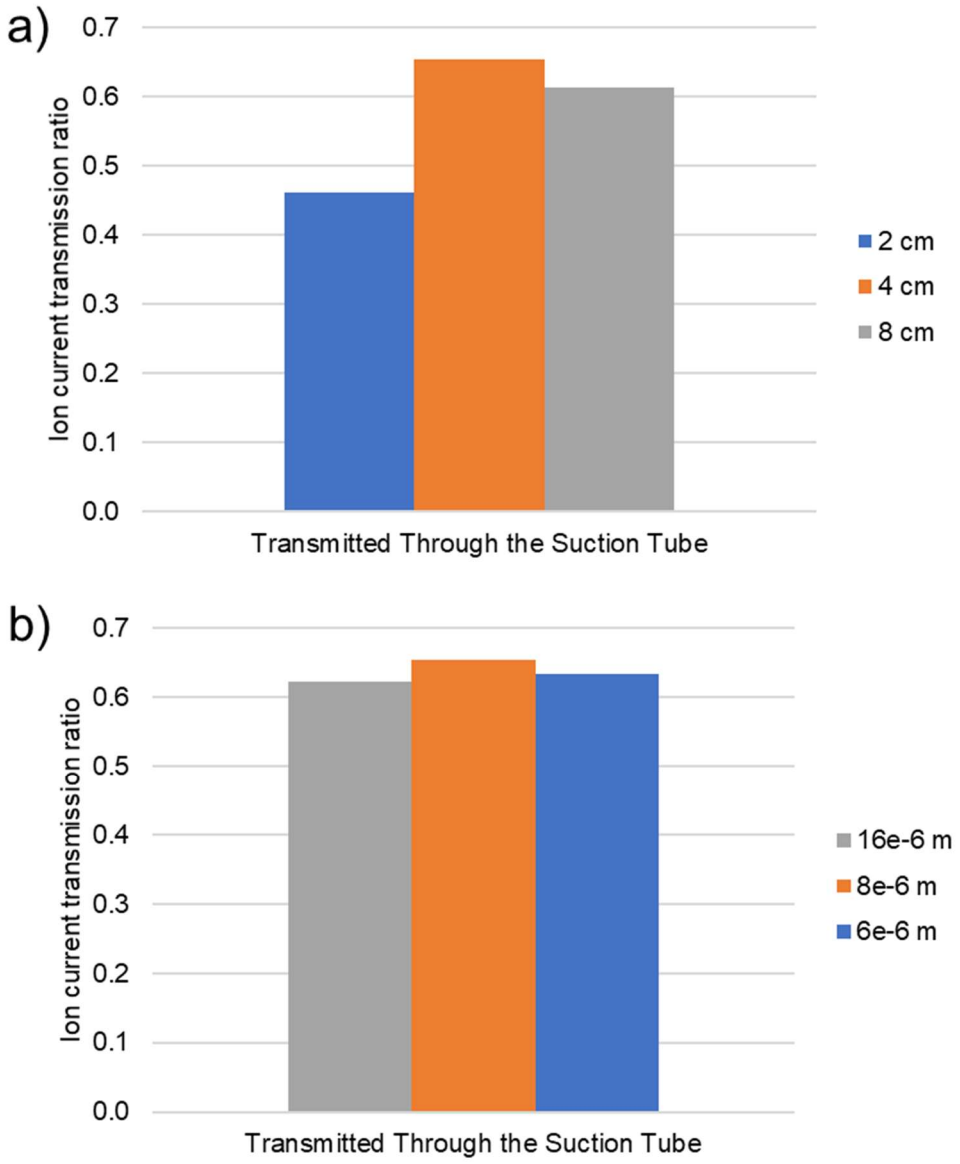


**Figure 2.7. Simulated ratio of ion current collected by the suction tube varying (a) domain diameter and (b) minimum mesh size.**

Figure 2.8 compares the electrical potential distributions along a line crossing the axis of the cylindrical domain at the axial distance z=4 mm and z=5 mm with varying domain size (The inlet of the suction tube is at z=5 mm). The slight variations in electrical potential in the central region are attributable to varying diameter of the cylindrical boundary and radial distributions of charged droplets. Still, the difference in potential

distribution between domain diameters 4 cm and 8 cm is low (<5%), resulting in comparable end fates of droplets.

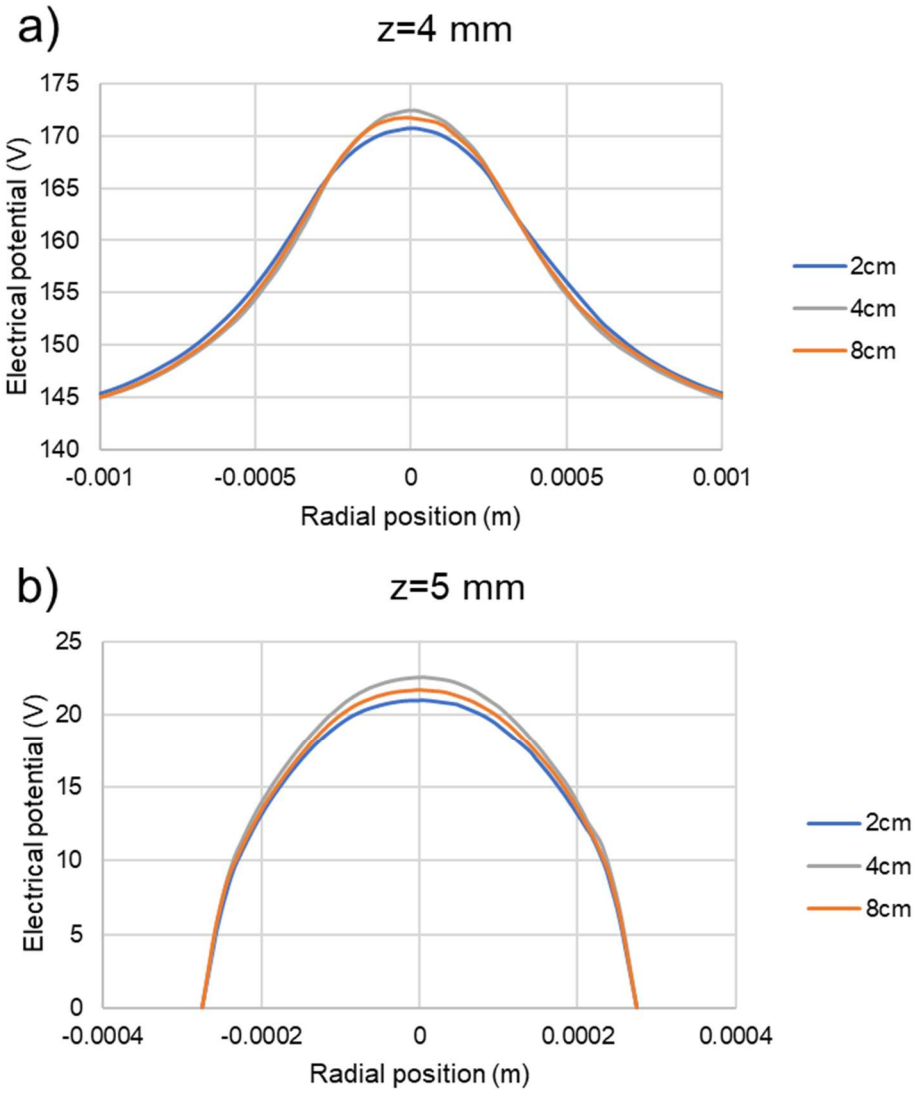


**Figure 2.8 Comparison of radial electrical potential distributions using three domain sizes of 2 cm, 4 cm, and 8 cm in diameter at axial position (a) z=4 mm and (b) z=5 mm downstream from the DRILL nozzle.**

2.2.4.3 Simulation of Droplet Separation in a Vortical Flow

The flow model is used as a key element for investigating the effects of varying flow conditions on the charged droplet trajectories and fates. In particular it is used to demonstrate the role of the outward inertia on the motion of a differently sized droplet populations in a vortical flow. Vortical flow advantageously leads to greater displacements of larger primary droplets from the core of the ESI plume than that experienced by smaller daughter droplets, a situation opposite that present in typical ESI (both with and without auxiliary gas flow). Results from simulations with a droplet population consisting of two droplet sizes, representing larger primary droplets and smaller offspring droplets, demonstrate that a swirling flow can significantly alter the droplet trajectories in a manner that depends strongly on the droplet size.

Previous experimental investigations led to some correlations that can be used for selection of the droplet sizes in the simulations. The size of electrosprayed droplets have been measured in numerous experimental studies using optical techniques such as PDA [11, 68] or Fraunhofer diffraction analysis [54, 69]. However, droplets smaller than 1 $\mu m$ in diameter are too small to be measured using the optics-based techniques with visible light illumination. Therefore, in many experimental studies, the measurements were conducted for electrospray at high liquid flow rates to produce droplets that are large enough to be detected optically. Often, there is also lack of information about the set of experimental conditions that can be correlated to the measured droplet size (i.e. solvent properties, spray current). Therefore, it is hard to determine the relevance of these measurement data to the conditions used for the actual bioanalytical characterization experiments. To estimate the size of electrosprayed primary droplets with charge $q$, the relationship reported by Tang and Gomez [70] is useful in the sense that the droplet

diameter is correlated to the measurable experimental conditions, the solution flow rate $V_f$ and the measured spray current *I*.

$$d_d = \left( \frac{6}{\pi} q \frac{V_f}{I} \right)^{\frac{1}{3}} \tag{2.18}$$

If a 100% Raleigh charged droplet is assumed, one can arrive at the following relationship.

$$d_d = \left( 24 \left( \frac{\varepsilon_0 \gamma}{2} \right)^{\frac{1}{2}} \frac{Q}{I} \right)^{\frac{2}{3}} \tag{2.19}$$

Considering the typical experimental conditions for bioanalytical ESI-MS analysis at nanoelectrospray flow rates ($Q$<1 $\mu$L/min and $I$<100 nA), the initial primary droplet size ranges between 1 and 2 $\mu m$. A primary droplet experiences iterative solvent evaporation and fission to generate multiple offspring droplets that are about 1/10$^{th}$ of the parent droplet in diameter [18].

Based on this understanding of electrospray aerosol generation, the representative droplet population used for the initial simulation study is binary and includes hundreds of 2 $\mu m$ and 200 nm droplets, corresponding to parent and daughter droplets, respectively. The droplet population is introduced at a release frequency based on the spray current using Eq. (2.13). The number ratio between parent and daughter droplets was set so that the number of daughter droplets released per unit time is 10 times greater than that of the parent droplets, to attempt to capture the reality that each parent droplet produces multiple (up to 20) daughter droplets every fission event, but fission events do not occur immediately after droplet production [20]. For each droplet size, the charge assigned corresponds to 80% of

the Rayleigh limit. The total spray current was set to $I$=60 nA, which closely matches the experimental current measurement for the sample solution used in bioanalytical studies (Chapter 5).

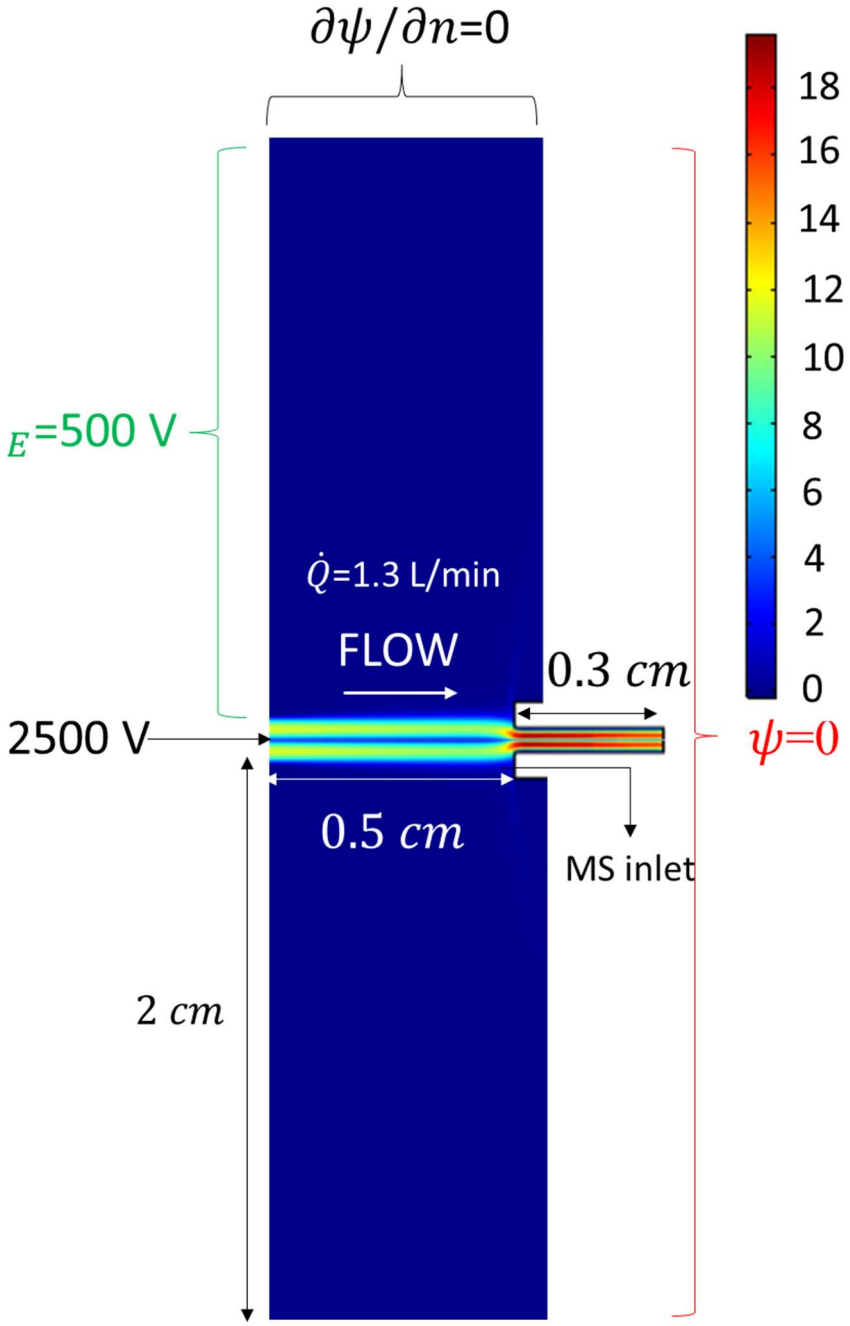


**Figure 2.9. Geometry of the 3D simulation model for electrosprayed charged droplet trajectories and the boundary conditions for electrostatics. A sample of charged droplets are released from the center of the bottom boundary. The contour plot indicates the swirl velocity field corresponding to $\dot{Q}_{Swirl}$=1.3 L/min.**

Figure 2.9 displays the geometry of the droplet trajectory simulation domain and the boundary conditions for electrostatics. For all simulation results presented in this chapter, the velocity field corresponding to $\dot{Q}_{Swirl}$=1.3 L/min ($2.17\times 10^{-5}$ $m^3/s$) was applied to the inlet boundary condition of the droplet trajectory simulation domain. The 3D cylindrical simulation domain includes the atmospheric pressure region (4 cm diameter) between the DRILL nozzle/vortex generator exit and suction tube/MS inlet, including 3 mm long protrusion into the MS inlet tubing. The pressure outlet boundary condition applied to the top surface of the MS vacuum interface allows the gas flow to enter the MS inlet without a loss. The electrical conditions applied to the electrode surfaces are as follows: $\psi_{MS}$=0 V, $\psi_{SPRAY}$=2500 V, and $\psi_{CE}$=500 V.

The electrical potential field was computed with incorporation of the space charge density term $\rho_S$ as shown in Eq (2.12). The space charge effects are responsible for radial growth of the electrospray droplet plume and greatly depend on the emitted spray current: The greater the spray current, the greater the ESI plume radius due to increased mutual repulsion between electrosprayed droplets with same-sign charge (Figure 2.10).

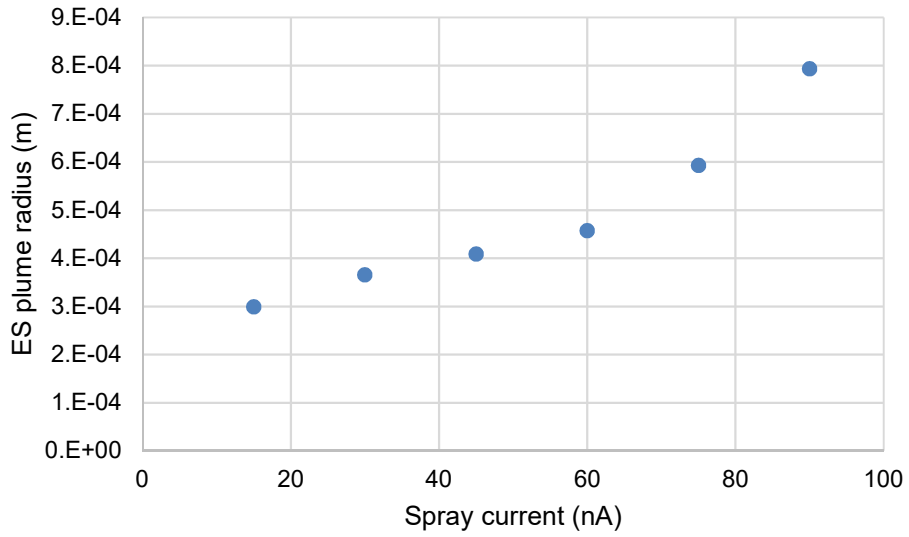


**Figure 2.10. Simulated vortical jet assisted ESI plume radius 5 mm downstream of the emitter vs spray current in vortical jet asssisted ESI. The electrospray droplet diameter used is 2 $\mu$m.**

Figure 2.11 demonstrates the final radial distributions (a to c) and the flight trajectories (d to f) of 2 $\mu m$ (parent) and 200 nm diameter (daughter) droplets and demonstrates a clear dependence on which of three flow conditions is being simulated: (1) electrospray into a vortical flow at $\dot{Q}_{Swirl}$=1.3 L/min ($2.17\times 10^{-5}$ $m^3/s$), (2) typical electrospray with no forced flow (stagnant gas), and (3) electrospray into a vortex-free axial jet at $\dot{Q}_{Vortex-free}$=1.3 L/min ($2.17\times 10^{-5}$ $m^3/s$). For clarity of visualization, the trajectories of only 30 droplets of each droplet size are plotted. Figure 2.11 (a) shows the radial size distributions of the charged droplets subject to the vortical flow at the final time step, $t$~100 $\mu$s. Here, all the small offspring droplets (blue) are densely distributed inside the inner "capture" diameter of the MS inlet, which means that they enter the MS inlet tubing without being lost elsewhere. On the other hand, the final radial locations of the large primary droplets (red) are between the tubing inner and the outer diameters,

indicating that all larger droplets are lost to the edge of the MS inlet tube. This is good evidence of size-selective droplet separation by the vortex-induced outward inertia (centrifugal force) producing an inversion in the distribution of droplets based on size, standing in stark contrast to the result for standard electrospray with no gas assist illustrated in Figure 2.11 (b).

In standard electrospray with no gas assist, larger droplets occupy the central region of the plume while smaller droplets are moved to the periphery. Although the number of larger droplets that are predicted to enter the MS inlet is small, as many of them impinge on the edge or the periphery of the MS inlet, the likelihood of capture of the smaller daughter droplets is even smaller, with most smaller droplets lost to the periphery. Droplets behavior is very size dependent. As droplets depart from the spray capillary tip, they experience very high electric forces due to a large electrical potential gradient ($\partial\Psi/\partial r \sim 8\times10^6$ V/m). This field accelerates both small and large droplets rapidly, imparting speeds of 70-100 m/s, but only the subsequent motion of larger droplets is dominated by the droplet inertia imparted by this initial acceleration. Momentum keeps larger droplets moving at a speed 2 to 3 times faster than smaller droplets, which slow down due to drag as they depart the region of intense acceleration. Therefore, the residence time for larger droplets is short, and larger droplets experience outwardly accelerating space charge effects for less time, reducing the resulting radial dispersion. Small droplets, which also experience the intense electric field and reach a high velocity near the spray tip slow down much more quickly as a result of drag. As a result, smaller droplets spend a greater length of time in the atmospheric pressure region while traveling toward the MS inlet, and thus are moved to the outer periphery of the ESI plume by the radially directed component of the electric

field, which is mostly a results of space charge in the plume. The simulated droplet size segregation in typical ESI is shown in Figure 2.11 (e).

Figure 2.11 (c) demonstrates the simulated radial distributions of droplets subject to a vortex-free gas jet. The axial and radial inlet velocity fields used are identical to those of the swirling flow, but the swirl velocity component is removed. Here, the final radial distributions of all droplets are within the inner diameter of the MS inlet, indicative of 100% droplet transmission into the inlet. In this case, the droplets carried by the gas jet (moving at an average axial speed of 27.5 m/s) travel at a speed approximately 3 to 10 times greater than those predicted for the no assist-gas condition. As demonstrated in Figure 2.11f, the fast-moving droplets experience less radial expansion resulting in good focusing of the ESI plume into the MS inlet orifice. Particularly, the smaller droplets segregate in the inner region of the plume in contrast to ESI with no-gas assist. The motion of smaller droplets quickly adapts to the flow field, moving at the speed of the gas jet. Therefore, small droplets experience space charge effects for less time and hence, less radial expansion. Likewise, larger droplets move faster compared to no assist gas jet condition to and so also do not spread out as much, although the effect on them is not as strong. Larger droplets are imparted greater momentum by the strong radially directed electric field near the emission point, and this creates some outward motion. Due to their greater inertia, they cannot as easily change direction, which explains their distribution over a greater radius. Nonetheless, the vortex-free gas jet allows for increased transmission of both small and larger droplets by focusing the plume. With this flow structure, one introduces a greater number of large droplets into the MS inlet along with effective capture of small droplets. While this increases abundance and signal intensity of the analyte ions,

it does not necessarily lead to improvements in detection limits of analyte ions as large droplets carry significant parasitic ions from unevaporated solvent and impurities that collectively contribute to reduced quality of MS spectra and increased chemical noise.

In this sense, a swirling flow offers a great advantage, enabling selective transport of smaller droplets and elimination of larger droplets from the electrospray plume as shown in the simulated droplet paths in a vortical flow (Figure 2.11d). It is worth noting that complete separation of larger droplets from the small droplet population does not occur within ~3.5mm from the droplet emission point. The highly accelerated motion near the droplet emission point causes larger droplets to move in the original direction by inertia, and this tendency appears to be predominant within 2mm from the origin. Beyond this distance, the outward inertia imparted by the vortical flow becomes effective moving larger droplets outward for separation to occur. As a result, only the small offspring droplet population enters the MS vacuum interface, providing favorable conditions for efficient droplet desolvation. Figure 2.11g shows the different droplet behaviors in the vortical flow. The smaller droplet follows the gas streamlines closely and turn sharply to enter the MS inlet under the influence of drag while the larger droplet's momentum results in its loss to the inlet wall.

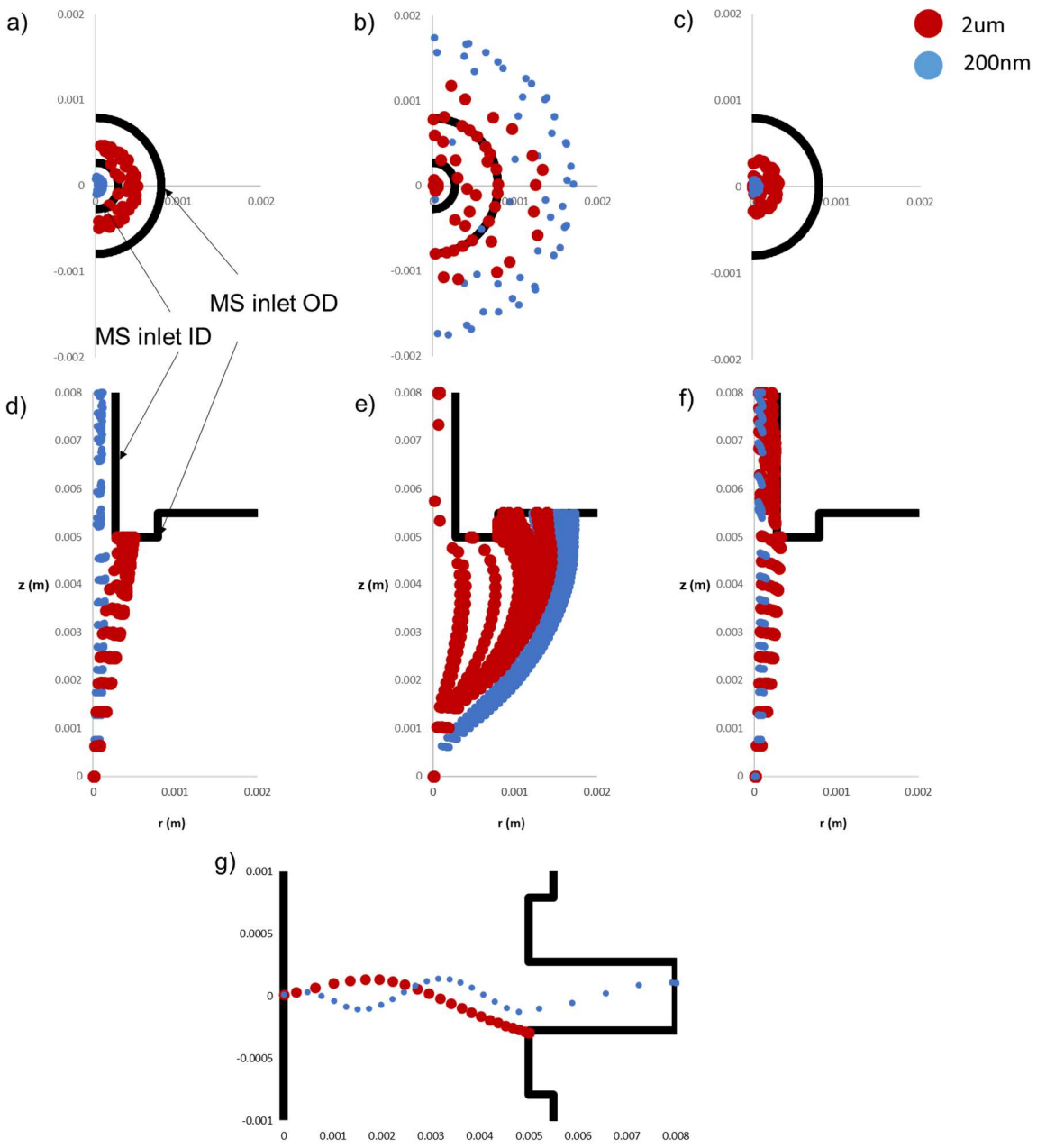


**Figure 2.11. Simulated radial distributions and trajectories of 30 randomly selected 2 $\mu$m (red) and 200 nm (blue) droplets subject to a vortical flow (a, d), no flow (b, e), and a vortex-free axial jet (c, f). (g) Comparison of simulated trajectories between 2 $\mu$m (red) and 200 nm (blue) droplets in vortical flow. Simulation parameters: I=60 nA, $\psi_{MS}$=0 V, $\psi_{SPRAY}$=2500 V, and $\psi_{CE}$=500 V, $\dot{Q}_{Swirl}$=1.3 L/min, and $\dot{Q}_{Vortex-free}$=1.3 L/min.**

2.2.4.4 Simulation of Droplet Radial Distributions

The droplet trajectory simulations demonstrate the ability of a vortical flow to alter droplet size distributions in ways not attainable in typical electrospray, resulting in size distribution inversion - small offspring droplets occupy the inner core, and larger primary droplets occupy the outer periphery. Here, a set of simulation results is presented to investigate the inertial effects on a wider range of droplet size populations (200nm to 10 $\mu$m), particularly focusing on extending the upper range of droplet sizes of relevance to high flow rate ESI-MS workflows commonly used in pharmaceutical screening applications. This is done by comparing the final droplet distributions between three different ESI conditions: vortical jet, vortex-free axial jet, and no gas flow assisted ESI. Each simulation only considers a sample droplet population of a single droplet diameter. The droplets are assigned charge corresponding to 80% of the Rayleigh limit for the given droplet diameter. The simulation parameters used are: $I$=60 nA, $\dot{Q}_{Swirl}$=$\dot{Q}_{Vortex-fre}$ =1.3 L/min (2.17× $10^{-5}$ $m^3$/s), and $d_d$=200 nm, 500 nm, 1 $\mu$m, 2 $\mu$m, 5 $\mu$m, and 10 $\mu$m

Figure 2.12 shows the simulated radial distributions at the final locations of two submicron droplet diameter populations 200 nm and 500 nm, respectively. In both cases, all droplets subject to the vortical and the vortex-free jets are distributed within the MS sampling orifice ID indicative of successful capture. With the assist gas jets, the submicron droplets closely follow the surrounding gas flow at the similar speed to the gas with reduced space charge effects and, hence, lesser radial displacements. This allows for 100% transmission of the small droplets with higher desolvation efficiency into the MS inlet, which may increase transfer of analyte ions into gas phase. In the submicron droplet range, no droplet loss occurs regardless of the assist gas flow structure. On the other hand, in absence of any assist flow, the small droplets are distributed over a much greater radius,

causing losses of the droplet populations without entering the MS inlet. Only a small portion enters the MS orifice, and the rest are lost.

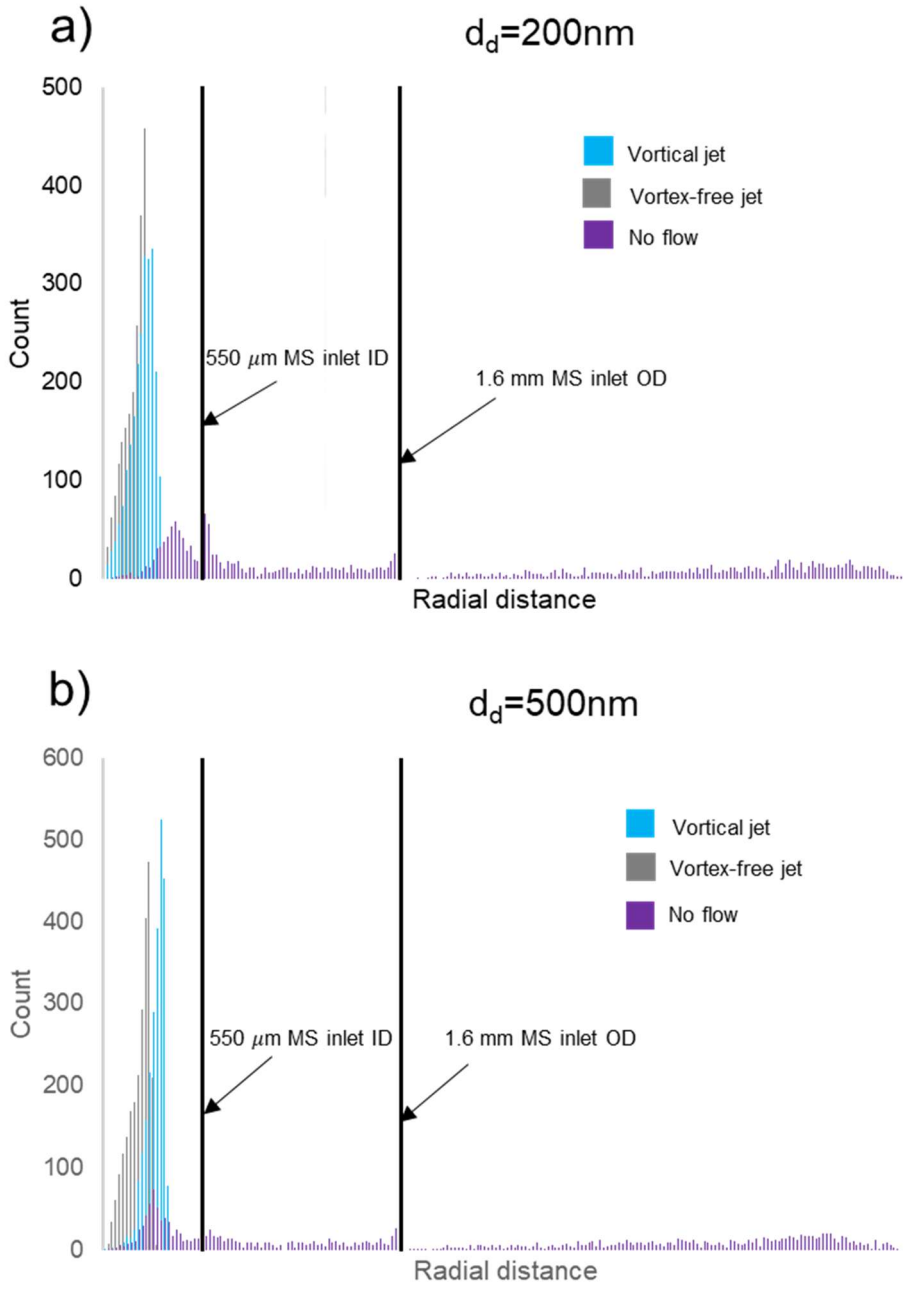


**Figure 2.12 Simulated droplet radial distributions of (a) 200 nm and (b) 500 nm diameter droplet populations.**

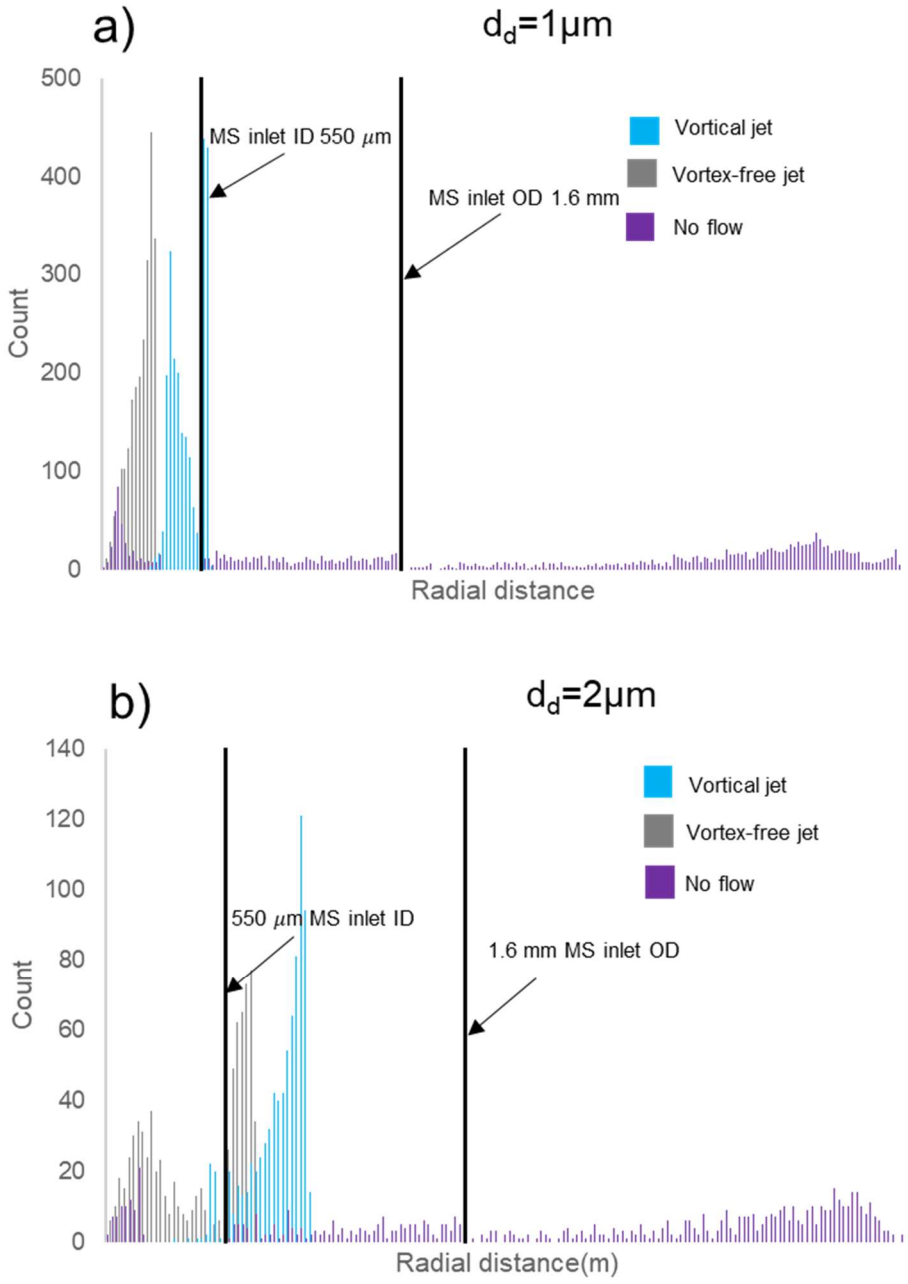


**Figure 2.13. Simulated droplet radial distributions of (a) 1 $\mu$m and (b) 2 $\mu$m diameter droplet populations.**

Figure 2.13 displays the simulated radial distributions of droplets at the final locations for 1 $\mu$m and 2 $\mu$m diameters, respectively. Unlike smaller submicron droplets, these ~1 $\mu$m diameter droplets demonstrate distinctly different radial distributions

depending on the structure of the assist flow. Most 1 $\mu$m droplets subject to the vortical jet are distributed closer toward the inner wall of the MS inlet, and some are excluded from entering the MS inlet. In the vortex-free jet, the same size droplets segregate in a smaller area close to the center, indicating the onset of the effects of the vortex-induced outward inertia for the micron-droplet size. When the droplet diameter increases to 2 $\mu$m, the inertial effects become more pronounced as most droplets are excluded from being captured by the MS sampling orifice. In contrast, a higher number of 2 $\mu$m droplets still make it into the orifice in vortex-free jet assisted spray. Without any assist flow, droplets are widely spread out with relatively lower transmission into the MS inlet due to longer droplet residence in air and increased plume extent.

Figure 2.14 shows the simulated (final) radial distributions of 5 $\mu$m and 10 $\mu$m diameter droplets. These droplet sizes are relatively large and are representative of primary droplets in micro-flow rate ESI. Most 5 $\mu$m droplets end up between the MS inlet ID and the OD with the vortical and vortex-free assist jets, with fewer 5 $\mu$m droplets entering the MS inlet in the vortical jet compared to the vortex free jet. As the droplet size increased to 10 $\mu$m, the radial distributions look close to one another between the vortical jet and the vortex-free jet assisted ESI, showing less dependency on the surrounding gas flow. Based on this, one can infer that the vortical-jet-induced inertial effects become less important for droplet sizes between 5 $\mu$m and 10 $\mu$m as the larger droplet motion is determined more by the initial momentum imparted by the rapid acceleration under the high electric force near the emission point.

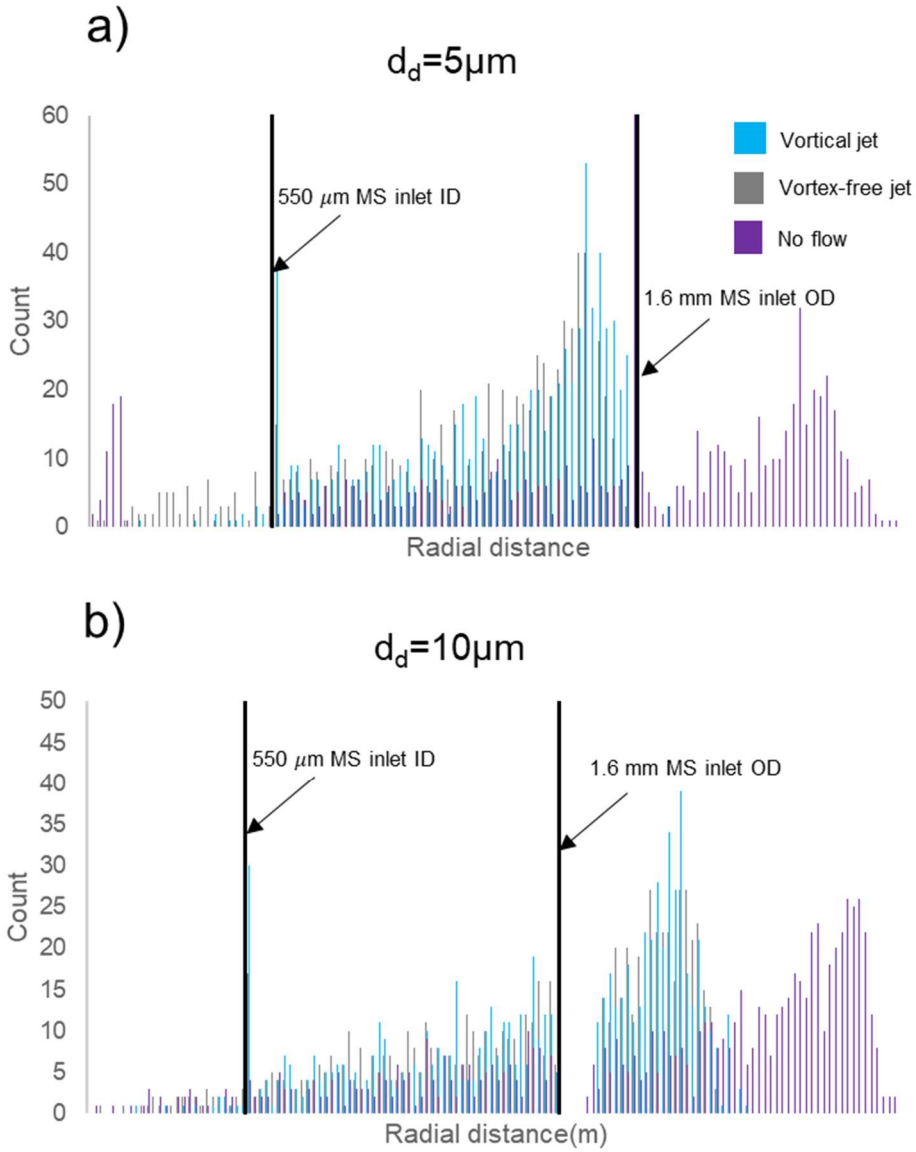


**Figure 2.14. Simulated droplet radial distributions of (a) 5 $\mu$m and (b) 10 $\mu$m diameter droplet populations.**

To evaluate the droplet transmission efficiency, one can define the % ion survival rate as the fraction of the total ion current injected with electrospray droplets that is collected by the MS inlet. Measuring the % ion survival rate is meaningful in the sense that the ion survival rate represents the portion of the total ion current that can reach the MS detector to produce MS signals. From the simulation results above, one can compute the

ion survival rate by taking the ratio between the electric current hitting the cross-sectional area within the MS inlet ID and the total spray current. The simulated % ion survival rate is plotted in Figure 2.15 for varying droplet dimeters subject to different electrospray conditions.

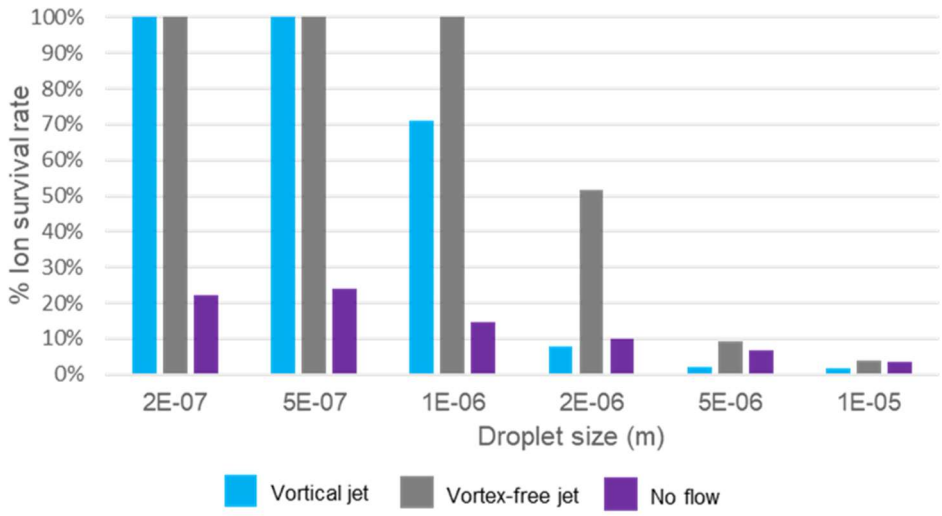


**Figure 2.15. Ion survival rate as a function of droplet size varying ESI condition**

As shown, all submicron droplets enter the MS inlet with assist gas flows regardless of it being vortical or vortex-free. With the vortical jet, however, the ion survival rate decreases significantly for the droplet size ≥1 $\mu$m. The 100% transmission of submicron droplets is attributed to the dominance of drag for these small droplets, which follow the flow into the MS inlet when assist gas prevents space charge repulsion from driving them radially outward. The motion of larger droplets (>5$\mu$m) is strongly influenced by the initial momentum imparted by the electric field near the droplet emission point, which drives them outwardly in the radial direction. For the intermediate droplet size range (1 $\mu$m<$d_d$<5 $\mu$m), the combined effects of electric repulsion, inertia and gas-guided transport all work together to determine droplet fate.

The simulation results above lead to the important conclusion that droplet separation effects by swirl can be leveraged for droplet diameters for which this interplay is important for flows of the swirl number used for these simulations. An important question is whether a change in the swirl intensity would broaden the droplet size range for which the inertial effects can be taken advantage of for effective population segregation. Figure 2.16 shows the effects of the swirl intensity (expressed as swirl number) on droplet radial distributions at their final locations. In this simulation, the flow field varies such that the corresponding swirl number ranges from 0 to 0.51. If the averaged droplet radial location falls within the area under the dashed line, which indicates the interior of the MS inlet, one may anticipate that a droplet of this specific size is likely to enter the MS inlet. There is little dependence of the (averaged) final distributions on increasing swirl number for small submicron droplets, and all droplets in this size range enter the MS inlet. The effects of the outward inertia by high swirl number flows appear pronounced for the intermediate size range between 1 $\mu$m and 5 $\mu$m. In presence of the strong vortex (S=0.51), most droplets in this size range are excluded from being sampled by the MS inlet. As the droplet diameter increases to 10 $\mu$m, an increase in swirl number no longer leads to a significant change in the average droplet location. In this situation, the motion and trajectories largely depend on the droplet inertia at the point of emission, where initial motion trajectory is set by the direction of the intense electric field with minimal impact of the outward inertia imparted by the vortical flow field.

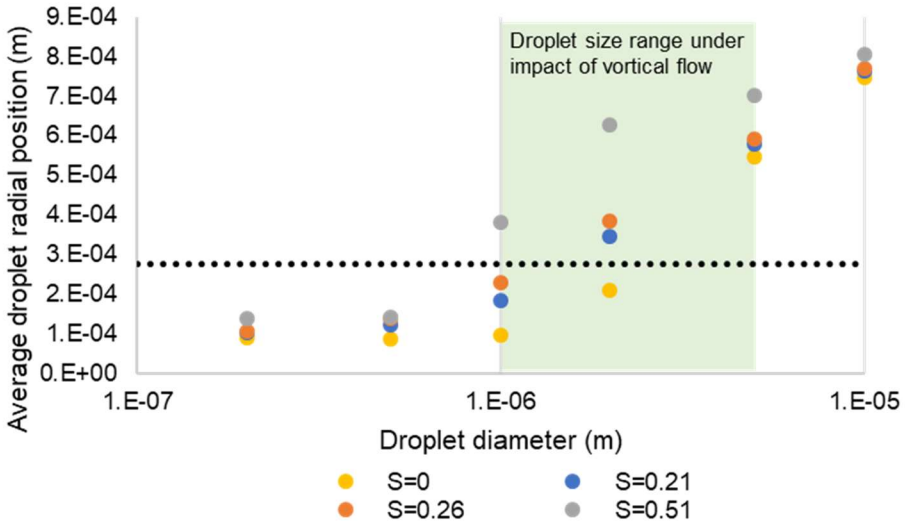


**Figure 2.16. Simulated averaged droplet final radial position as a function of droplet diameter varying swirl number**

### *2.2.5 Validation of the EHD Model*

Complementary ion current measurements were performed to evaluate the validity of the electrohydrodynamic modelling approach and simulation results. The ion current represents the sum of electrosprayed charged droplets and ions hitting the location for which a current measurement is performed. Figure 2.17 shows the experimental setup for the ion current measurements. A mock MS inlet (1.6 mm OD, 550 $\mu$m ID) of 3 cm length was aligned with the nozzle from which a swirling gas flow emanated. It is worth noting that the minimum 3 cm length of the suction tube in this setup (vs 3mm tube length in the simulation) was needed for the tube fitting connection to the vacuum pump. The flow rate entrained into the suction tubing (connected to a vacuum pump) was verified prior to experimentation to be 1.3 L/min ($2.17\times 10^{-5}$ $m^3/s$) using a GFM flow meter (1 L/min to 15 L/min flow range, Aalborg, NJ, USA). The suction tube geometry and the flow rate mimic the characteristics of the inlet interface of the Orbitrap mass spectrometer used in

the analytical studies of this dissertation (Chapter 5). The distance between the nozzle and the suction tube was 5 mm. Kapton dielectric tape was applied to the outer surface of the suction tubing, and insulating paint to its front edge, so that the ion current transmitted to the inside only could be measured. Both the spray needle and the suction tubing were connected to picoammeters to measure the spray current (leaving the electrospray needle) and the current received by the suction tubing. The ion current transmission efficiency was computed by comparing the current measurements at the spray tip and the inside of the suction tubing. The gas flow rate in the vortex generator was set to 1.3 L/min ($2.17\times 10^{-5}$ $m^3/s$) corresponding to a predicted swirl number S=0.33.

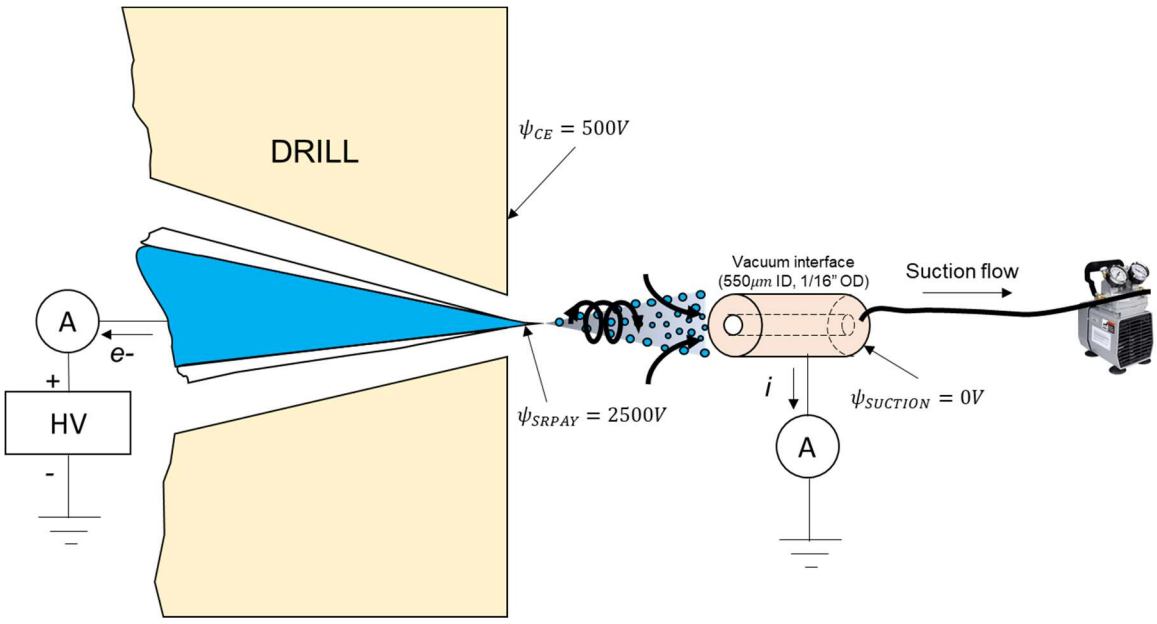


**Figure 2.17. Experimental setup for ion current measurements**

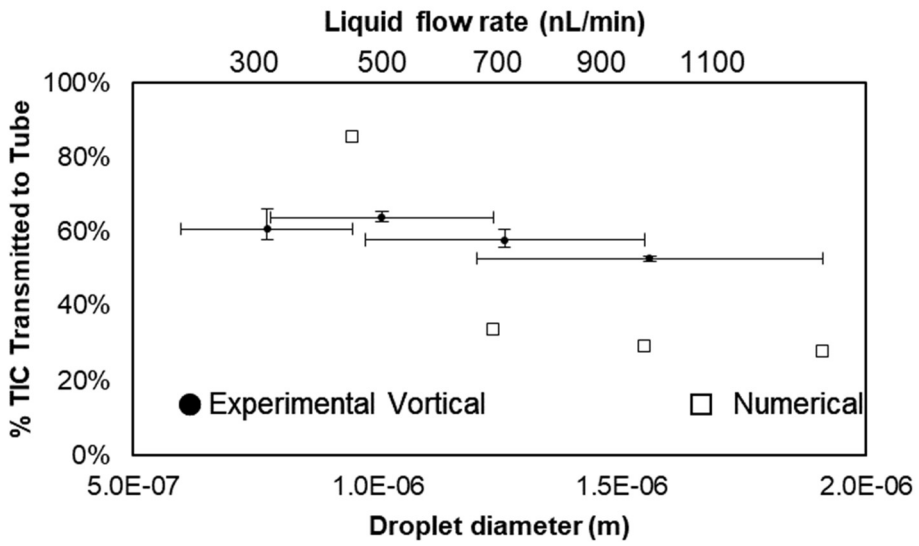


**Figure 2.18. % total ion current (TIC) transmitted into the suction tubing as a function of droplet size: Experimental (filled circle) and numerical (square).**

Figure 2.18 compares the simulated ion current transmission efficiency to the experimental measurements of vortical jet assisted ESI. The primary droplet size was estimated according to Eq (2.19) using the liquid flow rate $Q$ and the measured spray current $I$. The flow rate varied from 300 nL/min to 1000 nL/min to create varying droplet sizes of $O$(1 μm) diameter. The average spray current was measured to be ~60 nA. The horizontal error bar represents the estimated droplet size range assuming 50% to 100% of the Rayleigh limit. The upper and lower bounds of the vertical error bar indicate the maximum and minimum measurements, respectively. Simulation parameters used were identical to those used in the experiment. According to the simulations results, the efficiency of the ion current transmission to the MS inlet tubing steeply drops as the droplet size increases from submicron to a micron range. Then, the transmission efficiency gradually decreases with further growth in droplet size. The experimental data support the model predictions in that the measured transmission efficiencies are within the predicted

values, showing the decreasing trend with increasing droplet diameter. However, the experimental measurements do not show a sharp increase as the estimated droplet size decreased to submicron. The most likely explanation is that in the experiments there is a greater length of inlet tube on which droplets can be lost after capture by suction.

Despite the discrepancies arising from the broad range of the estimated droplet size and the different tube lengths used for simulations and the experiment, the experimentally measured ion current transmission efficiencies overlap the trend predicted by the simulations. Moreover, the model manifested its utility to effectively investigate the effects of interplaying electrohydrodynamic forces on droplet behaviors that strongly depend on the droplet size and charge. The unique capability for charged droplet population size inversion has been substantiated and comprehensively explored with the help of simulations, providing both an insight into fundamental physics of the interplay of electric and hydrodynamic forces and inertia on droplet trajectories and engineering guidance on design and operation of vortical flow gas dynamic interface (DRILL) for improved ion transmission and sensitivity of analysis by ESI-MS.

# CHAPTER 3. CHARACTERIZATION OF COUPLED EFFECTS OF A SWIRLING FLOW AND A SUCTION FLOW

The behavior of a vortical jet flow, alone and in combination with co-axial electrospray and suction through a small aperture, are experimentally investigated using optical visualization and ion current measurements. Schlieren photography, previously successfully employed for flow visualization between an ion source and mass spectrometer inlet [71, 72], is used to assess the vortical flow structure and source-to-sink gas-dynamic coupling as function of (1) the vortical jet characteristics (flow rate, diameter and swirl number), (2) suction characteristics (flow rate and diameter), and (3) the distance between the nozzle and the suction tube inlet. The main focus is to identify conditions for preserving the laminar structure of the vortical jet flow (important for effective size-selective separation of electrosprayed droplets) and onset of turbulence, as well as optimizing the gas flow "transmission" from source to sink. Additionally, optical flow measurements allowed the impact of electrosprayed droplets on the vortical jet flow structure to be determined, and the result indicating a negligible influence due to a significant mismatch of the liquid (electrospray) and gas flow rates and momenta. These findings are important for design of the DRILL interfaces, as it allows one to decouple the electrospray and gas flow considerations, and also supports an assumption of one way (gas-to-droplet) coupling in the model discussed in Chapter 2. Complementary ion current measurements provide insight into the effects of the flow-controlling parameters on charged droplet transport into the suction tube and their ultimate fate (i.e., transmission into a mass spectrometer for analysis vs loss to the ambient and tube external surfaces).

## 3.1 Schlieren Flow Visualization

Schlieren flow visualization is an optical technique that enables observation of phenomena where there is a spatial variation in the optical density of the medium. The first schlieren method was performed by Robert Hook in 1665 [73] to demonstrate the light-dark boundary in the image of a candle flame using a lens and another candle as a light source. The method was further developed by Toepler [74, 75] who invented a practical apparatus for schlieren visualization, including a knife-edge cutoff, a distinguishing feature of the schlieren technique from other optical approaches. The fundamental principle of this visualization technique is bending of light beams due to changes in refractive index (or optical density) of a fluid. (3.1)

The refractive index $n = c_o/c$ is a relative measure of the speed of light in a vacuum $c_o$ to the speed of light in the medium, $c$. The refractive index of an ideal gas depends on the medium density as approximated by Eq (3.2).

$$n = k\rho + 1 \tag{3.2}$$

where $k$, the Gladstone-Dale coefficient [76], is 0.00023 $m^3/kg$ for air at standard condition, and ranges between 0.0001 $m^3/kg$ and 0.0015 $m^3/kg$ for other gases [77]. The refractive index of common gases at standard temperature and pressure tend to vary only in the third or fourth decimal place. For example, the refractive indices of air and argon are $n = 1.000292$ and $n = 1.00028$, respectively. The refractive index of carbon dioxide, at $n = 1.0001$ is sufficiently different from that of air; this makes $CO_2$ a good choice "working fluid" for schlieren imaging of flow from a source into an air environment.

Figure 3.1 depicts a basic Schlieren apparatus which consists of a light source, two lenses, a knife edge, and a viewing screen. The beam from the point light source is collimated by the first lens and refocused by the second lens. The beam strikes on the viewing screen that projects an inverted image of the test section. To this point, without a knife edge, the system only shows the image of opaque objects as silhouettes in the test section. Transparent schlieren objects are not seen until a knife edge is installed at the focal point of the second lens.

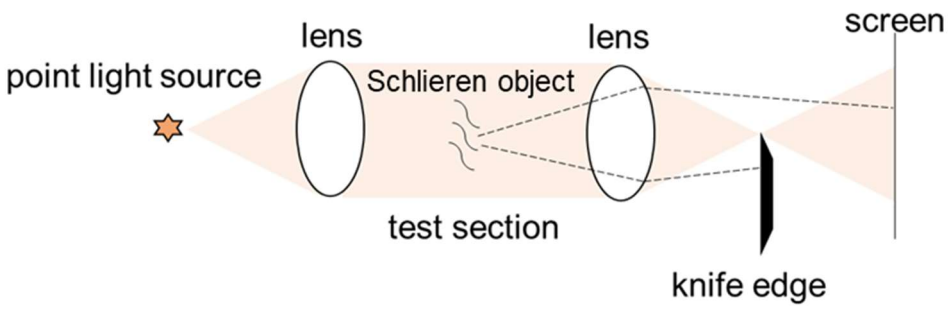


**Figure 3.1. Diagram of a simple Schlieren system [77].**

The ray bent from the upper point of the schlieren object in Figure 3.1 travels without hitting the knife edge and brightens the point on the screen. On the other hand, the ray deflected from the lower point of the object hits the knife edge, creating a darkened point against a bright background. The contrast between the lightened and darkened areas enables observation of the difference in refractive index originally invisible to human eyes. The knife edge orientation affects beam refractions within the plane perpendicular to the beam propagation. For example, a horizontal knife edge enhances the ability to detect the vertical components of density variation. On the other hand, only the horizontal refractive index gradient is visible using a vertical knife edge.

## 3.2 Visualization of Interactions between a Swirling Jet Flow and Suction

Schlieren imaging offers powerful capabilities to investigate the coupled effects of the DRILL generated vortical jet flow and a suction such as a MS inlet. The schlieren imaging experiments are conducted using an suction capillary in lieu of an inlet to a mass spectrometer for two reasons: (1) the mass spectrometer operating requirements prohibit introduction of gases other than air and nitrogen limiting the ability of schlieren visualization to distinguish the fine flow details of the flow structure due to small refractive index mismatch; (2) logistic and practical challenges in incorporating the schlieren imaging system within the laboratory space occupied by a mass spectrometer. Therefore, a suction mimicking the front end of a mass spectrometer with the matching flow rate was fashioned via stainless-steel tubing connected to a vacuum pump. The suction flow rate was measured to be 1.3 L/min ($2.17\times 10^{-5}$ $m^3/s$) using a flowmeter prior to optimal flow characterization.

### *3.2.1 Experimental Setup*

As schlieren lenses require the best quality possible, use of parabolic concave mirrors which allows a larger field of view for the same cost is popular. The off-axis mirror arrangement, a z-type system, is displayed in Figure 3.2 and used for the experiments. The schlieren set-up consists of two 1.1 m focal length concave mirrors of 10.8 mm diameter (Edmund Optics Inc., NJ, USA) and a 150 W halogen light source (Schott-Fostec, LLC, MA, USA). A 1 mm diameter hole in an aluminium foil tape is applied to the housing of the lamp to create a point light source. The test section is placed between the two mirrors with a minimum distance of about two focal lengths. A horizontal razor blade is placed as

a beam stopper at the focal length of the second mirror to block about 50% of the light rays. The single horizontal blade orientation produces enhanced visualization of features in the vertical direction revealing flow boundaries and shear layers. Photographs are captured using a Sony ILCE-7RM3 digital camera body with a zoom lens (Sony FE 70-300 mm f/4.5-5.6 G OSS Lens). The shutter speed is set to 1/800, the f/number to 5.6, and ISO to 100. The camera is connected to a computer on which Image Edge software is used to remotely control the camera setting and transfer images for further processing. Four background images are taken before starting the flow visualization and averaged to produce a reference image which is subtracted as a background from the flow images. Then, the intensity of each pixel in the resulting images was multiplied by a factor of 10 to enhance contrast of the flow features revealed by the schlieren. This post-processing is implemented using macro-coded scripts in ImageJ. Appendix A demonstrates the effects due to post-processing image enhancement.

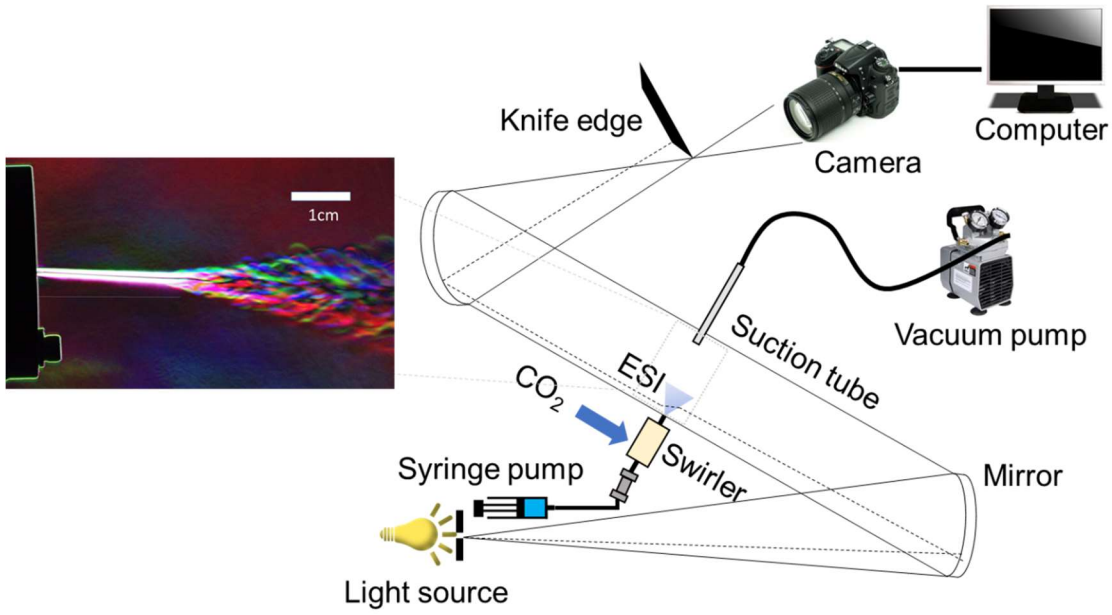

**Figure 3.2. Schematic of schlieren visualization system. Inset: Schlieren image (after post-processing) of a swirling flow generated by the DRILL interface.**

A suction system comprises of a stainless-steel capillary (1.58 mm OD, 0.55 mm ID, 3 cm length) in a Swagelok tube fitting (bored-through reducer, 1/16" to 1/4" tube OD), which is connected to a 1/4" ID tubing leading to a vacuum pump (DOA-P704, Gast Manufacturing, MI, USA). The pump is set to draw flow with the volumetric rate of 1.3 L/min ($2.17\times 10^{-5}$ $m^3/s$). This flow rate is chosen based on the measured suction rate of of the Orbitrap mass spectrometer [78] and personal communication with the MS manufacturer (Thermo Scientific, San Jose, CA, USA). The suction inlet capillary is affixed to a *xy* translation stage directly facing the vortex generating nozzle of DRILL for control of alignment and precise adjustment of the distance between the source of jet (exit of the nozzle) and the flow sink (the inlet to the suction capillary). Dry bone grade carbon dioxide is used as the working fluid for jet as it gives a substantial contrast in density (and therefore the refractive index) from the surrounding air. The flow rate entering the vortex generator is measured by a GFM flow meter (1 L/min to 15L/min flow range, Aalborg, NJ, USA) and controlled by a regulator upstream of the flow meter to establish a desired flow rate with a resolution of 0.1 L/min ($1.7\times 10^{-6}$ $m^3/s$). In all experiments, the $CO_2$ flow rate was varied from 0.4 L/min ($6.8\times 10^{-5}$ $m^3/s$) to 1.3 L/min ($2.17\times 10^{-5}$ $m^3/s$), with the maximum corresponding to the suction flow rate.

While $CO_2$ can be a good working fluid for schlieren visualization, the $CO_2$ gas is heavier than $N_2$ gas which is the actual gas used in DRILL (The $CO_2$ gas density is ~58% greater than $N_2$ gas in STD atmospheric condition). In case of horizontal gas jets ejecting from DRILL, the density difference of $CO_2$ from surrounding air causes the gravitational

effects to deflect the jets. Froude number $F_r = \overline{U}/\sqrt{h\Delta\rho g/\rho}$ [79] characterizes the deflection of the jet due to the difference in density between the working fluid and air: the larger Froude number, the smaller the deflection. Here, $\overline{U}$ is the average axial velocity, $h$ is the vertical thickness, and $\rho$ is the density of the working fluid. For $\dot{Q}$=1.3 L/min ($2.17\times 10^{-5}$ $m^3/s$) and the initial jet diameter of 1 mm, Froude number is 451 and 1947 for $CO_2$ and $N_2$ gas jets, respectively. The Froude number for the $CO_2$ jet is lower than that for $N_2$, which indicates a greater bending of the $CO_2$ jet will occur compared to that of the $N_2$ jet. However, in both cases, the inertia at the nozzle exit is 2 to 3 orders of magnitude larger than the gravitational force. Therefore, using both gases, a significant bending of the jet with the high exit velocity will not occur near the nozzle exit. For the flow rate range investigated in the experiments (0.4 L/min to 1.3 L/min), no noticeable deflection of $CO_2$ jets is observed within a few centimeters from the source. This allows one to translate the visualized phenomena with $CO_2$ to the actual DRILL operation without expecting major discrepancies.

The ion currents were measured concurrently with the flow visualization both at the electrospray needle, using a high voltage 9103 Autoranging picoammeter (RBD Instruments, OR, USA), and different segments of the suction tubes separated by dielectric inserts, using a low voltage Keithley 6485 picoammeter. Electrospray is produced using a fused silica emitter with a tapered tip of OD=ID=15 $\mu m$ (FS360-75-15-N-20). A KD Scientific syringe pump (model KDS 100; Holliston, MA, USA) is used to infuse 50:50 methanol/water with 0.1% acetic acid at two flow rates are used: 300 $\mu$L/min and 500 $\mu$L/min with accuracy $\pm$ 1% of the reading.

### *3.2.2 Results and Discussion*

A laminar swirling flow is essential to attaining the level of hydrodynamic control needed to manipulate droplet trajectories. Using schlieren visualization, one can determine the location at which the transition to turbulence occurs and the coupling of the vortical jet and suction flows, which are the two important aspects of conserving the flow structure needed for droplet separation and effective transport into the mass spectrometer. The study focuses on understanding the effects of different geometric and operating conditions, and the results reveal that transition to turbulence strongly depends on the flow rate and the relative position between the nozzle and the suction interface greatly impacts the ability to fully capture the flow via vacuum drag. The jet flow rate from the source exceeding the suction rate into the sink results in flow bypass and associated loss of electrical current (charged droplets) to the surrounding. Jet flows with smoothly developing shear boundary layer maintain a small diameter and show an improved coupling into the suction interface and directed transfer of charged droplets. When the flow is partially captured, creation of turbulent flow features including eddies and mixing layers appear around the suction interface. These chaotic characteristics of the flow may lead to losses of small droplet populations whose motion is greatly affected by the carrier gas flow. The results from the experimental flow characterization provide useful insight into DRILL-ESI-MS operation (flow rate, relative distance, positioning, etc) to maximize the inertial separation effects enabled by a vortical flow while maximizing the flow source-to-sink coupling and droplet/ion transfer for mass spectrometric analysis.

#### 3.2.2.1 Characterization of Vortical Jets

The effect of varying flow rate on free (i.e., no suction) swirling jets is investigated by the Schlieren visualization. The studies reveal turbulent flow features including the more rapid jet expansion and time varying flow structures.

Figure 3.3 shows example of schlieren photographs of vortical jets emanating from the 1 mm diameter nozzle (flow rates from 0.4 to 1.3L/min.) The ESI emitter (360 $\mu$m OD) protrudes 1 mm past the nozzle orifice coaxially. The effect of increased flow rate on the jet expansion and greater mixing is apparent. To create the RGB (red/green/blue spectral component) image for each flow rate, three photographs are taken consecutively with an appropriate spectral filter and combined using 'merging multi-channels' functionalities of ImageJ. In laminar well-ordered steady flow, red, green, and blue light components perfectly overlap, yielding white schlieren image. Spaghetti-like color-coded features indicate unsteady nature to the flow and turbulence.

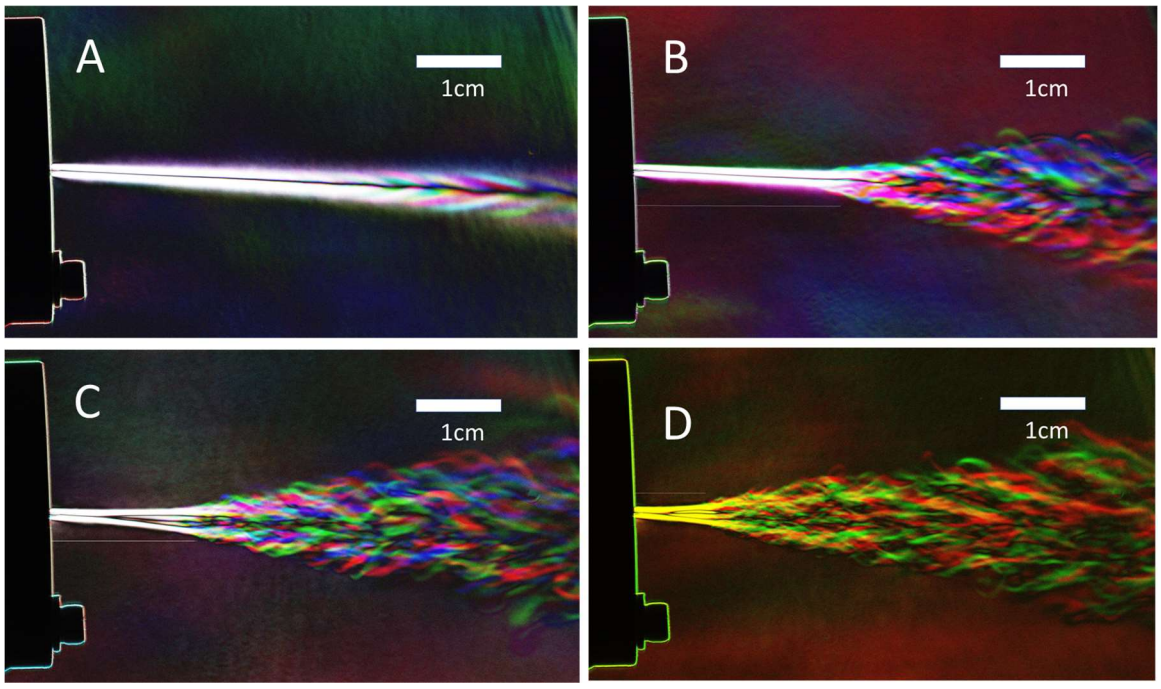

**Figure 3.3. Schlieren images of vortical jets emanating from the 1mm diameter nozzle. $CO_2$ flow rate used was (A) 0.39L/min, (B) 0.65L/min, (C) 0.91L/min, and (D) 1.3L/min. The simulated swirl numbers S are 0, 0.1, 0.16, and 0.33, respectively.**

Immediately after exiting the nozzle the jet boundary is smooth and the jet diameter grows slowly, indicative of laminar flow. For each flow rate a transition point exists beyond which turbulent features appear: these are unsteady flow features and a more rapid growth of the jet boundary, or colloquially, "rainbow spaghetti". The turbulence onset distance, $d_{TO}$, is determined for each flow rate using the schlieren images to estimate the location of first appearance of visible turbulent flow features.

A few factors that may cause alteration in $d_{TO}$ are considered to observe any dependence on parameters other than the flow rate used. For example, flow over an object such as the ESI emitter may be disturbed leading to a change in $d_{TO}$ vs no emitter condition. Therefore, measurements of $d_{TO}$ displayed in Figure 3.5 are implemented for the baseline case (1) no emitter and for varying emitter (capillary OD=360 $\mu$m) position relative to the nozzle orifice exit - at (1) 0 mm, (2) 1 mm, and (3) 2 mm past the nozzle. Previous experimental studies that investigated different flow characteristics associated with swirling jets reported greater lateral spreading [80] with enhanced mixing [81] as compared to vortex-free jets. In addition, the first appearance of the shear layer rolling up into vortex rings in the vortical jet, indicative of laminar-to-turbulent transition, was observed in half of the distance compared to that for the vortex-free jet with comparable *Re* on the order of $10^4$ [80]. Although the *Re* range investigated in the previous work is far greater than that of the swirling jets (*Re* up to 3400) explored in this dissertation, similar flow features are observed in the schlieren images in Figure 3.4 in comparing a vortical jet to a vortex-free jet at the same flow rate introduced from the same diameter nozzle (1 mm). The vortex-

free jet in Figure 3.4 was created using a union with multiple inlets orthogonal to the annular gas domain in Gen 3 DRILL (Figure 1.6) in replacement of tangential inlets. The schlieren image of the vortical jet in Figure 3.4a clearly displays rapid divergence of the flow to a greater radius vs a vortex-free jet (Figure 3.4b) and much earlier onset of turbulence.

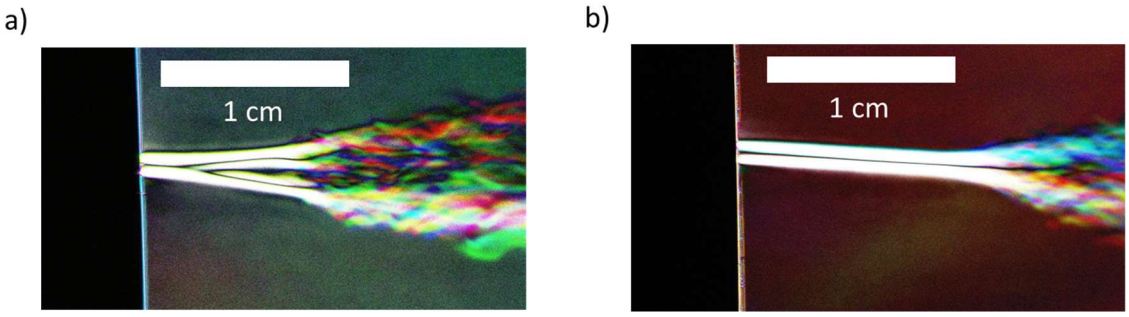


**Figure 3.4. Schlieren image of (a) vortical jet and (b) vortex-free jet. Both flows exit the 1 mm nozzle at the flow rate of 1.3 L/min corresponding to *Re*=3422. Capillary emitter is inserted into the nozzle with the tip flush at the nozzle orifice.**

Figure 3.5 compares the measured $d_{TO}$ between vortical jets (filled circle) and vortex-free jets (empty circle) with varying flow rate. Each data point represents the measurement value from using different emitter extension lengths. In Figure 3.5a, the turbulence onset distance of both flows drops sharply with increasing flow rate for $\dot{Q} <$ $ca.$ 0.8 L/min ($1.36\times 10^{-5}$ m$^3$/s). As the flow rate increases further, $d_{TO}$ declines more gradually, and for $\dot{Q}$ =1.3 L/min ($2.17\times 10^{-5}$ m$^3$/s), the average $d_{TO}$ is measured to be $d_{TO}$=8.4 mm. For flow rates < *ca.* 1 L/min, greater variations in the $d_{TO}$ measurements are observed depending on the relative emitter position.

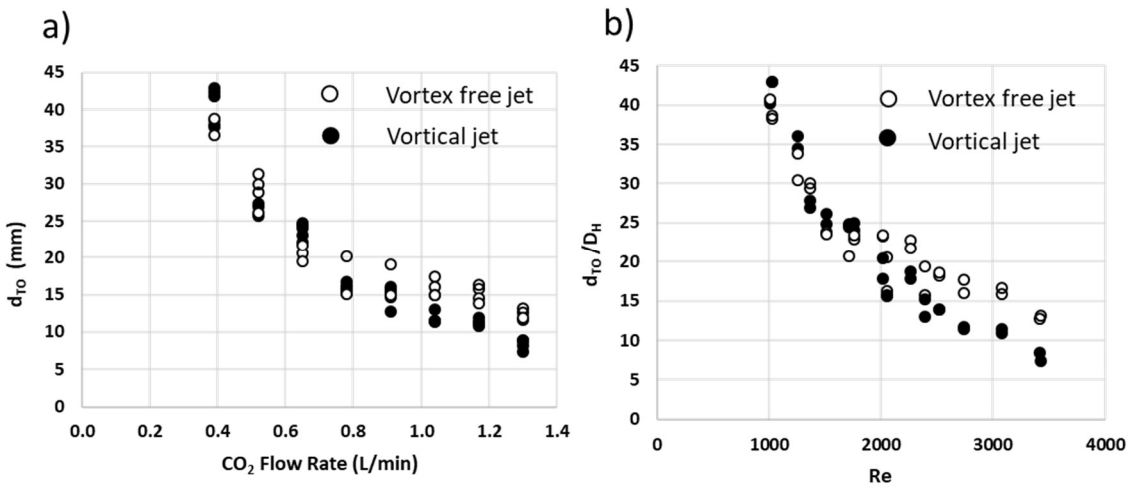


**Figure 3.5. Comparison of distance to turbulence onset ($d_{TO}$) between vortical jets and vortex-free jets (a) $d_{TO}$ vs. $CO_2$ flow rate (L/min), (b) $d_{TO}/D$ vs. Re. Different data points correspond to various electrospray emitter (capillary OD= 360 $\mu$m) position, protruding out of the nozzle to 0mm (flush), 1mm, and 2mm.**

To observe the effect of swirl on turbulence onset, the measured $d_{TO}$ of vortical jets (filled circle) are now compared to those of vortex-free jets (empty circle) emanating from the same 1mm nozzle (Figure 3.56a). The $d_{TO}$ measurements from the two flows overlap for $\dot{Q}$<1 L/min. For flow rates > 1 L/min, $d_{TO}$ from the vortical jets drops below further compared to the vortex free jets, showing complete separation between the two measurement data sets. This appears more obvious in Figure 3.5b which displays the data in non-dimensional form $d_{TO}/D_H$ as a function of Reynolds number $Re$, $Re = \dot{Q}D_H/\nu A$ where $\nu$ is the gas ($CO_2$) kinematic viscosity, $D_H$ is the hydraulic diameter, and $A$ is the annular flow area of the nozzle. The earlier transition to turbulence for vortical jets becomes apaprent at $Re$>2500 as compared to vortex-free jets. On the other hand, vortical jets for $Re$<2500 with the predicted swirl number S<0.16 result in no discernible difference in $d_{TO}/D_H$ compared to vortex-free jets. This is in contradiction to other visualization studies of swirling jets with lower Re=1000 and S>0.4 [82], which reveal small scale

random vortices in the shear layer at much shorter distances vs non-swirling jet (S=0), suggesting earlier turbulence onset. The possible causes of the discrepancies between the previous observation [82] and the results presented in Figure 3.5 are twofold: (1) The swirl number for $Re$<2500 is too low (S<0.16) to result in distinct impact on transition to turbulence. (2) The intensity of swirling created with the supplied gas flow rate $\dot{Q}$ <1 L/min in this specific DRILL geometry is less than the predicted value (S=0.16). The slice images of the swirling jet using a laser scattering technique (Images are found in Appendix B) appear to support the latter as the swirling flow patterns became clearly visible for $\dot{Q}$~1 L/min. Specific to use of this vortex generator, one may expect the vortex-induced inertial effects to become more pronounced for $\dot{Q}$ >1 L/min. For inertial droplet separation in rotational flows, turbulence with unpredictable and chaotic flow characteristics should be avoided due to reduced control over the droplet motion. In terms of DRILL operational guidance in ESI-MS applications, this data can be used to determine a maximum nozzle to MS suction distance beyond which the vertical jet would become turbulent.

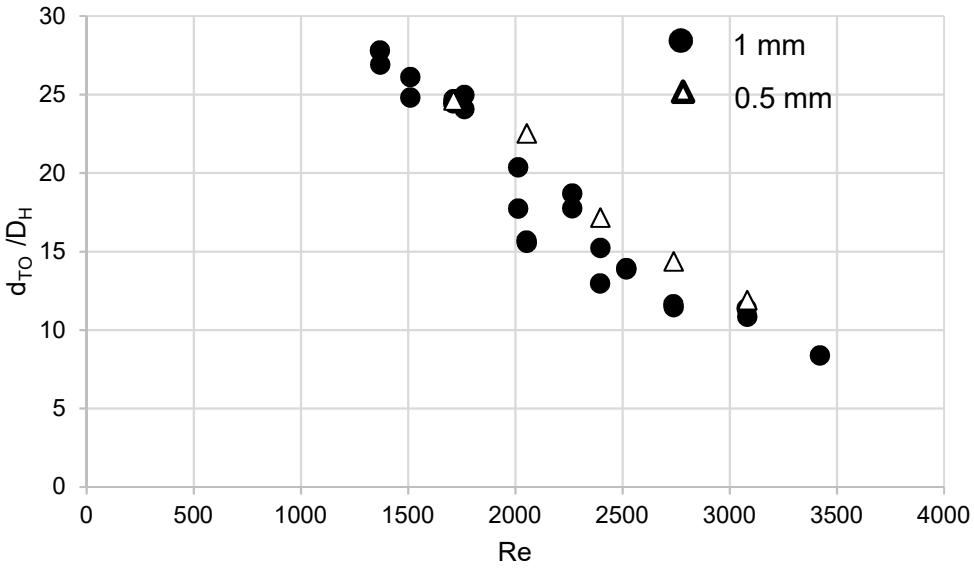

**Figure 3.6. Normalized turbulence onset distance $d_{TO}/D_H$ vs $Re$. The swirling jet emanates from the nozzles with diameter of 500$\mu m$ (labeled with triangles) and 1mm (labeled with circles).**

The same experiment is conducted with a smaller jet nozzle ($D = 0.5$ mm) and results are presented in Figure 3.6. Each data point corresponds to different emitter extension lengths from the 0.5 mm and 1 mm diameter nozzles, respectively. Using the small diameter nozzle with no emitter placed the nondimensionalized $d_{TO}/ D_H$ data agree well with the trend exhibited by those using the larger nozzle (1 mm diameter), suggesting a correlation between the two non-dimensionalized quantities, $d_{TO}/ D_H$ vs $Re$.

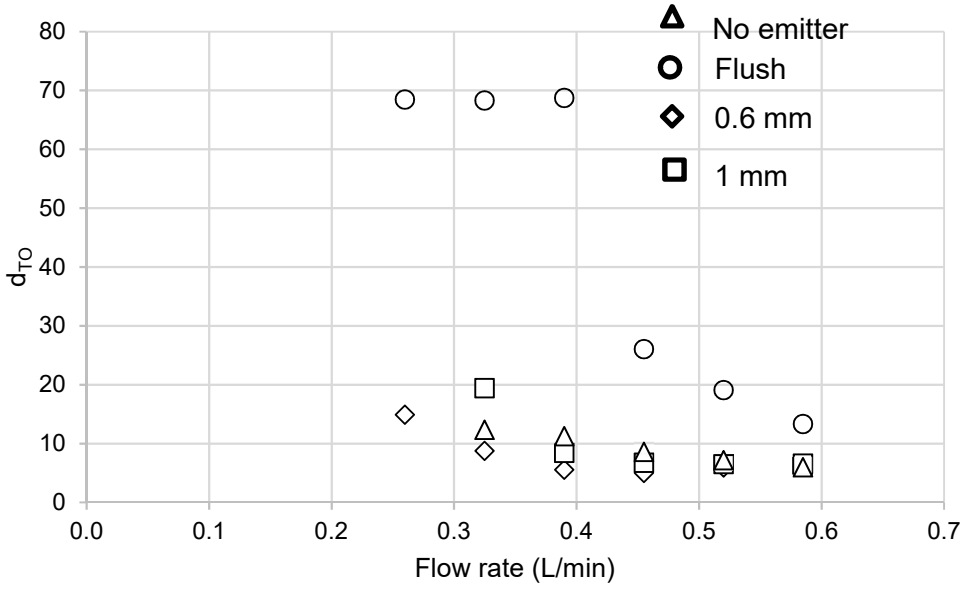


**Figure 3.7. Turbulence onset distance $d_{TO}/D_H$ vs supplied flow rate leaving the nozzle with diameter 500$\mu m$. Displayed are the results using no emitter (labeled with triangles), the ESI emitter (360 $\mu$m OD) flush with the nozzle (circles), extending 0.6 mm (diamonds), and 1 mm (squares) past the nozzle.**

On the other hand, $d_{TO}$ measurements vary significantly with the emitter position as indicated by larger differences between the data points in Figure 3.7. The variability of measurements using the small nozzle diameter ($D=0.5$ mm) is attributable to the high ratio

(up to 0.72) between the emitter outer diameter and the nozzle diameter, which present a challenge in control of co-axial alignment of fairly flexible capillary within a small orifice of the nozzle exit. The studies presented in the remainder of this chapter use vortical jets created by the 1 mm diameter nozzle to produce flows whose $d_{TO}$'s that behave consistently independent of the emitter position.

#### 3.2.2.2 Effects of Electrosprayed Charged Droplets on Turbulence Onset

To investigate the effects of the electrospray (ES) on the laminar to turbulent flow onset in gas jets, electrospray produced at two different liquid flow rates (300 nL/min and 500 nL/min) is introduced into the vortical jets. The ES emitter is positioned flush with the 1mm diameter DRILL nozzle. The average spray current is 62 nA, which is in a range of that used for many ESI-MS processes for bioanalytical studies. The turbulence onset distance, $d_{TO}$, is measured with varying gas and liquid flow rates. Figure 3.8 compares the $d_{TO}$ measurements (normalized by the DRILL hydraulic diameter) acquired in presence of sprayed ES droplets to that for no electrospray (but with the emitter capillary remaining in place). There are slight variations in $d_{TO}$ at low *Re* depending on the liquid flow rate used, indicative of weak two way coupling between electrospray droplets and gas flow for lower Re<2000. This may be associated with the increased influence of viscous effects of flow over droplets at lower Reynolds numbers.

For *Re*>2000, ES has no apparent impact on $d_{TO}$. This supports one-way coupling between ES droplets and the flow field. In other words, the effects of the charged droplet motion on the flow are negligible, which is an important simplification used for DRILL modeling as discussed in Chapter 2.

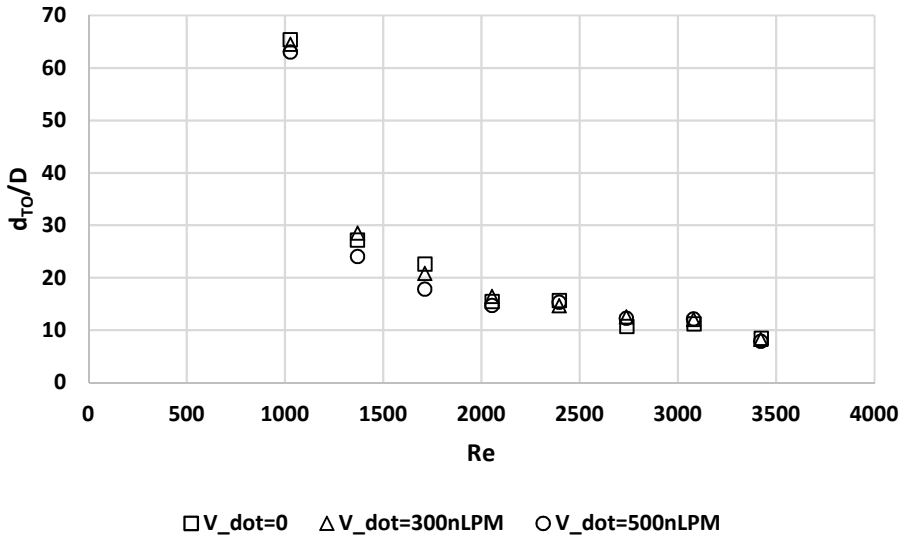


**Figure 3.8. Effect of electrospray on onset of turbulence in vortical gas jet. Results compare the ES liquid solution flow rates of 300nL/min (triangles) and 500nL/min (circles) vs no-spray baseline case (squares). ESI emitter flush with the nozzle.**

To determine if the conclusion that ES has little to no effect on turbulence is more generally true, the experiments were repeated with ES droplets from an emitter extending 1 and 2mm from the nozzle. Figure 3.9 compares the normalized $d_{TO}$ measurements with varying ES droplet emission locations for the fixed solution flow rate $\dot{V}$ =500nL/min. Again, the results indicate that the location of droplet emission does not alter the transition to turbulence.

Overall, the effects of the electrospray with flow rate on the order of 100 nL/min the gas flow with Re>2000 is observed to be negligible: rate of jet growth and turbulence onset are hardly perturbed by the rate and the location of electrospray emission especially for Re>2000. This appears to be attributed to several orders of magnitude difference in the volumetric rates between the liquid droplet emission (nL/min) and the gas flow (L/min).

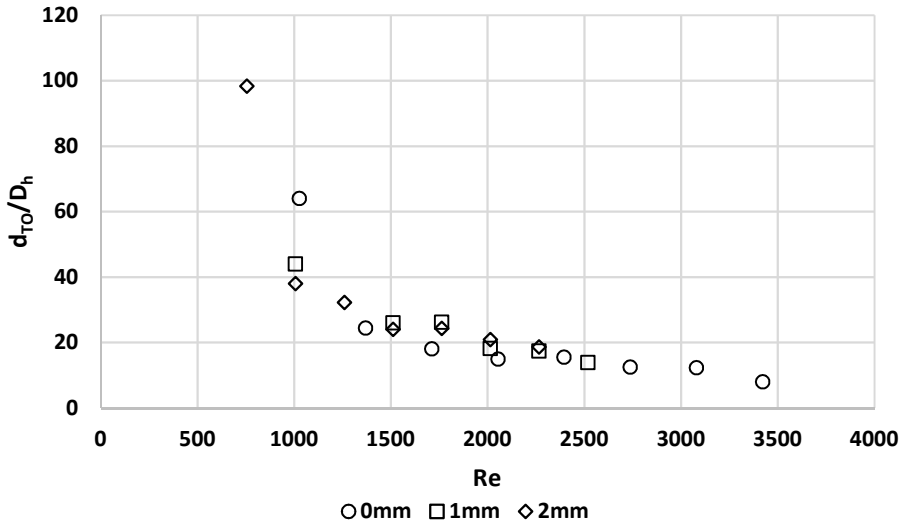


**Figure 3.9. Effect of electrospray source location on onset of turbulence in vortical gas jet. Results compare varying ES droplet emission points measured from the exit of the nozzle: flush/0mm (circle), 1mm (square), and 2mm (diamond) past the nozzle.**

3.2.2.3 Coupled Effects of a Vortical Jet and Suction

The presence of suction in the vicinity of a vortical jet can have a significant impact on the flow structure, in particular by keeping the jet from expanding and dissipating its momentum, and also by enhancing the swirl strength at the suction inlet. In full coupling of a swirling jet and a flow suction (Figure 3.10a), the jet experiences little growth in diameter and maintains the swirl velocity while traveling to the suction interface. If the swirling component of the momentum is retained, then if the jet enters a smaller inner diameter suction tube, conservation of angular momentum causes the swirl velocity to increase. This coupling of the two flows enables retention and even enhancement of the inertia experienced by droplets in outward direction, which is a fundamental principle that DRILL exploits for droplet separation by size. On the other hand, incomplete coupling of

the two flows (Figure 3.10b) results in a partial loss of mass and momentum dissipation, accompanying reduced hydrodynamic control for inertial separation and droplet transport.

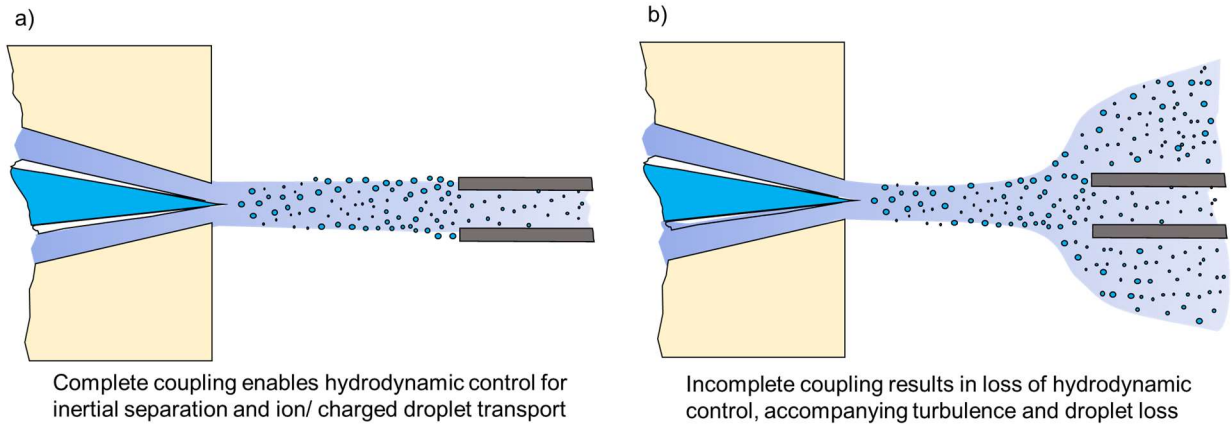


**Figure 3.10. Impact on charged droplet transport of (a) complete coupling and (b) incomplete coupling between a vortical jet flow and suction.**

Schlieren images are useful to characterize the coupling of a vortical jet in conjunction with suction, including the role played by flow rate, separation distance and axial alignment.

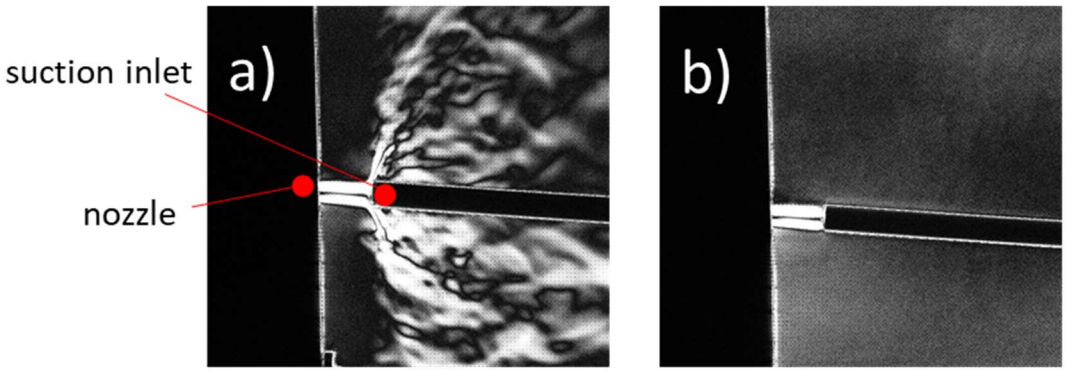


**Figure 3.11. Schlieren photographs of the swirling jets without (a) and with (b) suction. The suction tubing is aligned with the 1mm in diameter DRILL nozzle at a distance of 3mm. The DRILL gas (CO2) flow rate used is 1.3L/min.**

The effect of suction on the jet expansion appears quite significant as illustrated in Figure 3.11. In Figure 3.11a, the mock MS inlet (suction) tube (right) is at 3mm from the DRILL nozzle (left), but no air is being actively drawn into it ($\dot{Q}_{Suction}$=0). As the swirling jet ($\dot{Q}_{Swirl}$=1.3L/min) impinges on the suction tube (with no suction OFF), it deflects and expands sharply around the tubing edge in highly turbulent stream. In Figure 3.11b, the vacuum pump connected to the suction tune is activated to draw the gas at the same rate as the swirling jet (1.3 L/min), and the jet is clearly fully captured. The flow boundary is smooth, and the diameter nearly constant with jet exhibiting a solid rod like structure on the schlieren image.

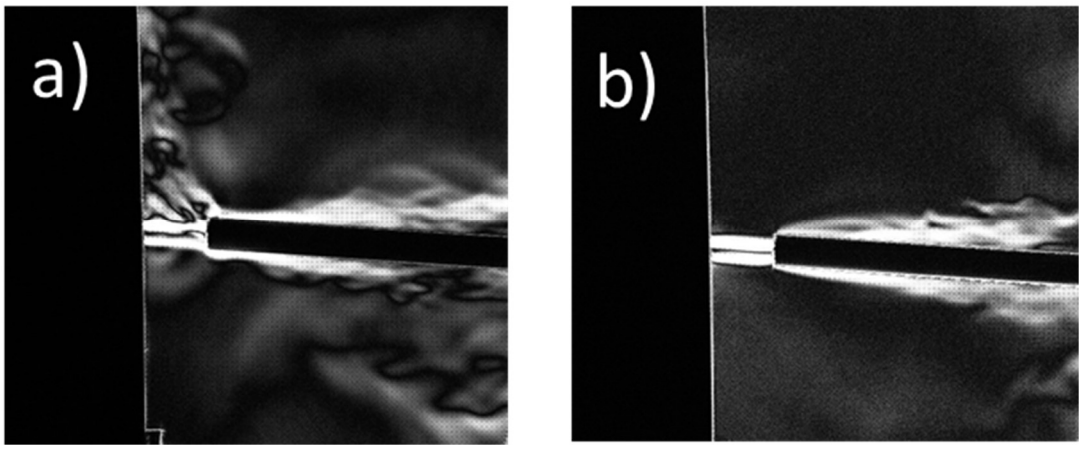


**Figure 3.12. Schlieren photographs of the swirling jets in off-axis positioning relative to the suction tube - without (a) and with (b) suction. The suction tube is placed at 3mm from the DRILL nozzle. The DRILL gas flow rate used is 1.3L/min.**

When the suction tube is shifted off-axis slightly from its completely aligned position with respect to the DRILL nozzle (Figure 3.12) the ability of the suction to capture the entire jet is lost demonstrating the importance of precise alignment between the flow source and sink when DRILL is used in ESI-MS workflows.

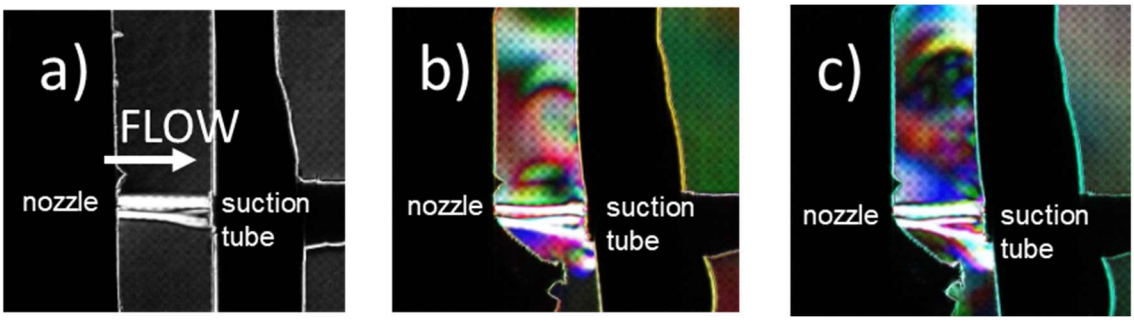


**Figure 3.13. Schlieren photographs of coupling between the swirling jet and flow suction assessing the impact of the flow rate mismatch: The suction flow rate is set to 1.3 L/min (same for all cases) and the vortical gas jet flow rate increased from (a) 1.3 L/min to (b) 1.43 L/min and to (c) 1.56 L/min.**

To investigate the effects of the relative gas flow rate in DRILL (vortical jet source) and the suction tube (flow sink) on the flow capture efficiency, the vortical jet flow rate is incrementally increased above the suction rate (1.3 L/min). In Figure 3.13a, the flow rate of the jet is set to 1.3L/min so that it matches that of the suction. Despite a slight growth in flow diameter near the suction inlet, the swirling jet is completely collected by the suction tube (located at a distance of 6mm from the nozzle). At an increased flow rate of 1.43 L/min, the flow expands to a barrel shape (Figure 3.13b), causing a partial loss of mass and momentum dissipation of the flow into the ambient air. With an additional flow rate increase to 1.52L/min (Figure 3.13c), the jet diameter increases to a greater diameter a few millimeters before the suction tube, and a significant portion of the flow rebounds off the wall in the periphery of the suction orifice and is dissipated to the surrounding air. It can be concluded that complete transmission of the gas jet with the flow rate exceeding the suction rate is not possible if (1) jet flow rates exceed that of the suction and (2) the suction interface is at an extended distance from the jet source, leading to rapid growth in jet diameter with possible transition to turbulence (Figure 3.13c), even if the matching of the two flow rates (jet and suction) allows for complete capture of the flow. Only at the

conditions that preserve both the laminar structure of the vortical jet and establish a perfect match between the source and sink flow rates, as well as adequate axial alignment of the jet and suction tune, the strong and spatially coherent swirling "rod" like flow structure could be achieved that provides a dual benefit of an effective inertial sorting of droplets in drug-induced centrifugal motion and effective transmission of smaller (retained in the jet core) droplets into a suction section of the mass spectrometer. In fact, incomplete coupling of the flows is shown to decrease the charge transmission efficiency of the electrical current into the suction tube/vacuum interface, as discussed later in this chapter.

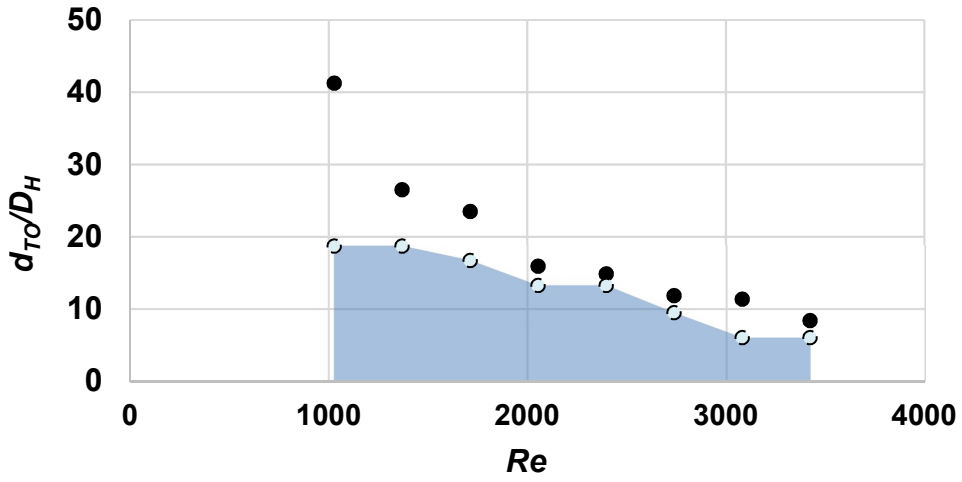


**Figure 3.14. Comparison between the non-dimensional turbulence onset distance (filled circles) and the maximum distance (blank circles) at which complete flow coupling is possible as a function of Reynolds number. The suction flow rate is set constant at 1.3 L/min while the vortical jet flow rate was varied from 0.4 to 1.3 L/min. The suction tube diameter is 550 $\mu$m.**

Effective coupling also depends on the distance between the nozzle and suction, with higher flow rates requiring less separation. In Figure 3.14, the turbulence onset distance (filled circles) for a given *Re* is compared to the maximum distance at which the jet and suction coupling appears complete (blank circles). For the entire range of swirling

jet Re numbers associated with a 1 mm nozzle and flow rates from 0.4 L/min and up to the maximum vacuum pump capacity (1.3 L/min) coupling places a more stringent limit on the maximum distance than avoiding turbulence. For example, a swirling jet with $Re$=3000 emanating 10 mm from the inlet to the suction tube cannot be fully captured while the flow has yet to transition to turbulence at the location of the suction inlet. In other words, in Figure 3.14 as long as the nozzle-to-inlet distance is within the shaded area (blue), the vacuum interface fully captures the flow which will be laminar. At $\dot{Q}$=1.3 L/min, it is observed that the suction interface cannot fully collect the flow growing to a diameter greater than 3 times the suction tube ID, providing quantitative design guidance for the nozzle size which determines the initial jet diameter. In this work, we only investigated the suction tube of 550 $\mu$m ID and the flow rates up to 1.3 L/min to match the characteristics of the inlet interface of the Orbitrap mass spectrometer used in the analytical part of this dissertation (Chapter 5). In reference to Figure 3.5b, one can infer that the strength of the vortex in rotational flow becomes significant for the vortical jets with $Re$>2700 as their behavior begins to deviate from the vortex-free jets as quantified by the earlier transition to turbulence. Therefore, one may expect a flow with $Re$ > 2700 to demonstrate pronounced inertial separation effects associated with increased effect of vorticity. In this *Re* range, the maximum distance of 6-10 mm is allowed between the nozzle and the suction interface for full capture of the flow. The maximum distance possible for complete coupling is desirable for ESI-MS applications as it allows: (1) prolonged droplet evaporation leading to increased production of ion/smaller droplet populations favorable for MS analysis, (2) effective droplet separation as complete removal of larger droplets from the ESI plume

does not occur within 3.5 mm from the source according to the simulation results (Chapter 2).

### 3.2.2.4 Effects of Jet-to-Suction Flow Coupling on Charged Droplet Transport

Current measurements are used to obtain insight into the fates of electrosprayed droplets/ions injected into the jet. Figure 3.15 displays the schematic of the setup used to measure the current to three different locations. The current measurement on the suction tube is due to the electrospray droplets/ions getting to the inner wall of the tube, and the measurement on the aluminium plate due to the droplets/ions lost without entering the vacuum interface. In addition, the current to the bend electrode is from the charge that is successfully advected by the suction without being lost to other electrodes upstream (this portion would possibly contribute to useful MS signal).

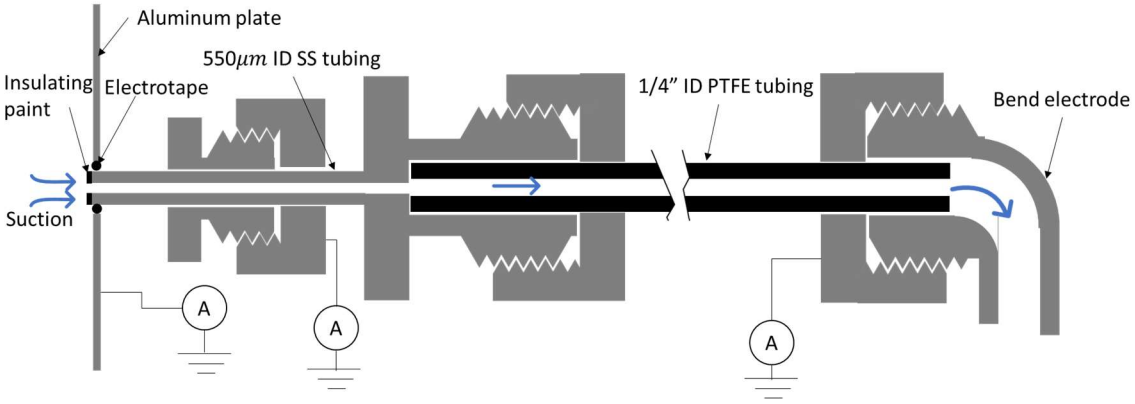


**Figure 3.15 Schematic of the current measurement setup consisting of the suction tube, the plate electrode, and the bend electrode.**

Figure 3.16 demonstrates the clear effect of the suction on the current transmission. Here, the nozzle is 6mm away from the vacuum interface, and an aluminium plate electrode is added to the periphery of the suction tube to collect any current lost (i.e., no entered the

tube). (The plate is electrically isolated from the suction tube). In the top left image, the vacuum pump is off with no air entrainment into the tube. The jet flow with $\dot{Q}$ = 1.3L/min fails to enter the tube without suction and is dispersed to the surrounding air along with charged electrospray droplets it carries. In this situation, most spray current ends up on the plate electrode (grid), and little current is measured inside the tubing (blue fill). With the suction turned on and gas being entrained at 1.3 L/min into the suction tube, nearly 60% of the spray current is measured inside the tube inlet. On the other hand, the current collected by the plate electrode significantly decreases as more droplets/ions are dragged into the suction tube. This illustrates strong dependence of the charged droplet/ion fates on the dynamics of the carrier gas flow.

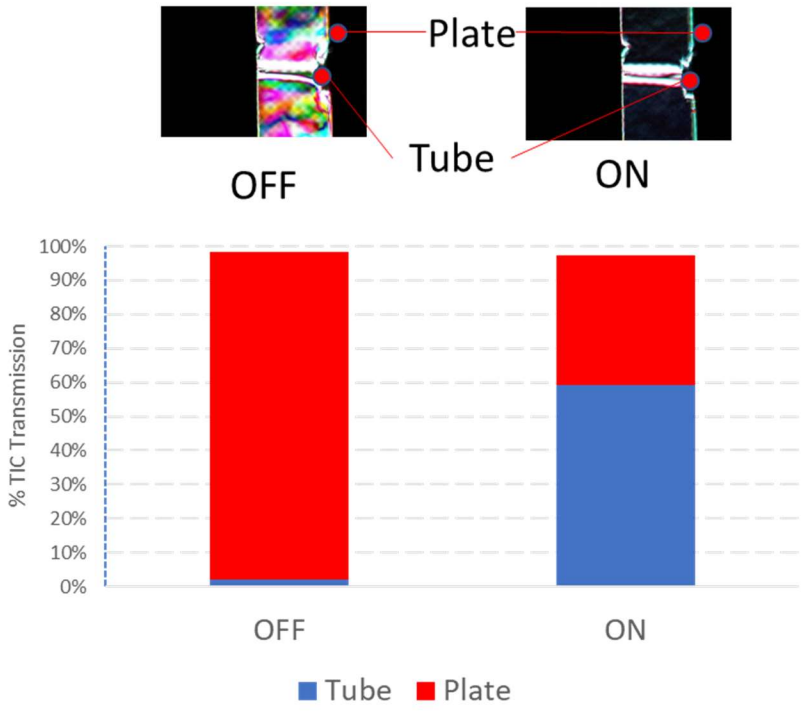


**Figure 3.16. Comparison of normalized current collection by the tube and the plate electrodes. The vacuum pump is initially OFF (left) and turns ON (right). The flow rate is 1.3 L/min for both suction and vortical jet, and the nozzle is at 6mm from the inlet to the suction tube.**

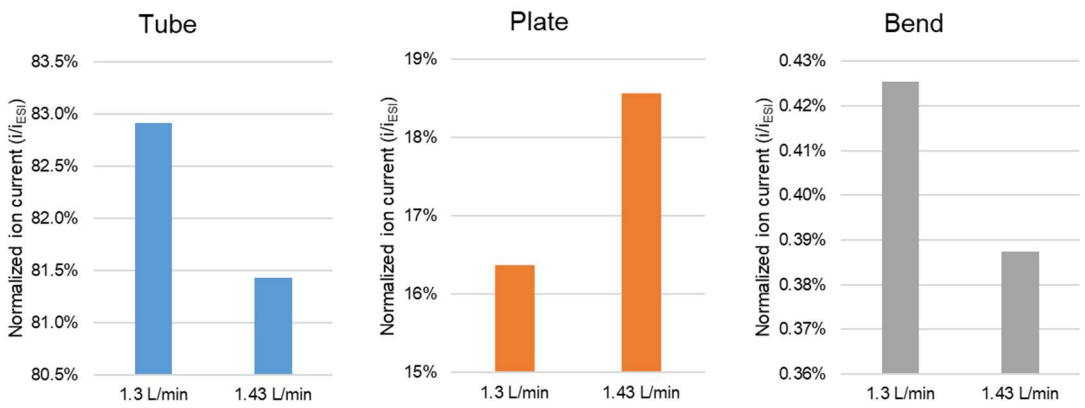


**Figure 3.17. Normalized ion current ($i/i_{ESI}$) to various electrodes (tube, plate, and bend) for $\dot{Q}$ = 1.3 L/min and 1.43 L/min. The current to the bend is the "useful" current that could improve the signal in mass spectrometry.**

Figure 3.17 shows the change in ion current to different locations/components as the flow rate increases by 10% (from 1.3 L/min to 1.43 L/min) above the vacuum pump suction flow rate (1.3 L/min). A measured ion current to each component (tube, plane and bend) accounts for the sum of ions and charged droplets hitting the specific component per unit time. The normalized ion current is defined as the ratio of the collected ion current to the spray current. With increasing gas flow rate, the spray current increases due to greater velocity of charged droplets. Therefore, pairwise comparison of normalized ion currents between two different flow rates provide the information on the effects of the flow rate on ion/charged droplet fates. As shown in Figure 3.13, when excess flow ($\dot{Q}$ = 1.43 L/min) is provided, complete coupling between the flow source (swirling jet) and sink (suction) is not possible. This corresponds in Figure 3.17 to an increase in the portion of the total current collected by the plate electrode from ~16.4% to ~18.5% and decreased currents to the suction tube and the bend electrode 30 cm downstream of the suction inlet, making it clear that the excess (beyond the suction capacity) flow rate causes a loss of transmission of droplets/ions and ultimately reducing the ion signal detected by the mass spectrometer.

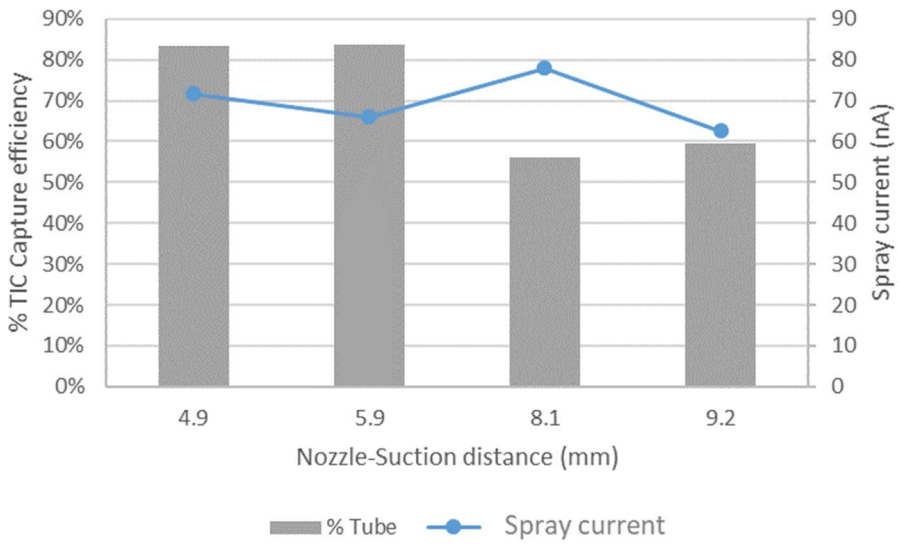


**Figure 3.18. Ion current transmission efficiency with varying distance between the jet nozzle and the suction tube. The flow rate for gas jet and suction is the same 1.3 L/min.**

Figure 3.18 compares the ion current transmission efficiency with varying nozzle-to- suction tube distance from 4.9 mm to 9.2 mm at a condition of matched jet/suction flow rate (1.3 L/min which corresponds to *Re*~3400). As indicated in Figure 3.14, the flow is fully coupled for separation distances of 4.9 mm and 5.9 mm. The corresponding ion transmission efficiency is above 80% at these two distances. In contrast, for separation distances of 8.1 mm and 9.2 mm complete coupling is not achieved (Fig. 3.12), and the ion transmission efficiency into the suction tube drops to ~60%. The transmission efficiency is slightly greater for a separation distance of 9.2 mm than for 8.1 mm. The most likely explanation due to the lower overall electrospray current for the larger separation distance (ES current for 9.2 mm is ~30% lower than that for shorter separation distances, as the intensity of the spray inducing electric field is reduced by increased distance between the emitter and counter electrode). With decreased spray current (except when the separation distance increases from 5.9 mm to 8.1 mm increases due to elevated electrical potential

difference needed for electrospray, the spray current increases) space charge effects are lessened and the ESI plume experiences less radial expansion, thus allowing more ions to enter the suction interface. Nevertheless, a significant drop in ion transmission efficiency is observed as the nozzle moves from the full flow capture region (d=4.9 mm and 5.9 mm) to partial capture region (d=8.1 mm and 9.2 mm) in terms of jet source to suction separation distance.

### *3.2.3 Implications of Flow Visualization on DRILL Design and Operation*

The combined capabilities of optical visualization and current measurements provide valuable insight into the vortical ESI-MS interface design and operation. Given the DRILL geometry, schlieren images of the jets and transition to turbulence assessment suggest a sufficiently strong swirling motion for the flow rate $\dot{Q} > 1$ L/min, which is essential for droplet inertial separation effects. In addition, the suction/sink flow rate imposes a limit on the maximum input/source flow rate to achieve complete coupling between the swirling jet and the flow suction. Complete coupling of the jet and suction flows (which occurs at the distances shorter than transition to turbulence) places an upper limit on the distance between the jet originating nozzle and the suction tube, the maximum value of which provides the ideal conditions for improved droplet desolvation and sufficient droplet separation with greatest benefit to DRILL ESI-MS applications. For the geometry and suction flow rate investigated, the maximum separation distance for compete coupling occurs when the jet diameter grows beyond approximately 3 times suction tube ID. For the specific flow rate $\dot{Q}$ = 1.3 L/min realized at the vacuum (suction) interface of the Orbitrap mass spectrometer, the distance between the DRILL vortex generator nozzle and MS inlet should be kept within ~6 mm. Ion current measurements suggest that the ion/

charged droplet transport strongly depends the flow coupling between the vortical jet and the suction. Optimal ion current transmission into the mass spectrometer (measured at the bend electrode in Figure 3.17) is achieved by complete flow coupling, which is correlated with the matching flow rate, on-axis alignment between the flow source and sink, and the separation distance shorter than the maximum value at which the jet growth is too large to be fully converged into the suction tube.

# CHAPTER 4. VORTICAL FLOW INTERFACE (DRILL) DESIGN FOR ELECTROSPRAY IONIZATION MASS SPECTROMETRY (ESI-MS)

With the advent of soft ionization techniques, mass spectrometry has assumed a prominent role in biomedical research, with applications ranging from fundamental biochemical studies such as protein characterization and kinetic measurements, to basic research in cell biology, and extending to applied fields such as biomarker discovery, disease diagnosis, and metabolite profiling. New ion sources, sample preparation methods, and improvements in mass analyzers have been introduced to further the growth in applicability of MS and to meet the demand for greater flexibility and higher quality of data. A key limitation of any bioanalytical technique is the limit of detection (LOD), which is directly related to the ability to convert an analyte at vanishingly small concentrations into a detectable signal. In the current workhorse ionization method for biochemical applications, electrospray ionization (ESI), an estimated 80% of analyte ions that are electrosprayed into the MS inlet are lost due to incomplete desolvation. Elimination of incomplete desolvation therefore offers a minimum expected five-fold improvement in the LOD. In fact, for many analytes, the improvement in LOD will be much greater due to the nature of signal suppression in ESI-MS. This is due to the fact that in general, more hydrophobic molecules have higher ionization efficiencies than hydrophilic ones unless sufficient desolvation occurs; insufficient desolvation can result in no detection at all, even when analyte concentrations are above those that should produce a measurable MS signal.

Current methods for ion transmission and desolvation prior to introduction into the mass spectrometer's internal vacuum deal with the conflict arising from the increased spread of charged droplets with time, and the need for longer residence time for greater desolvation, through a combination of three approaches: (i) increasing desolvation rate via increased temperature of the gas surrounding the droplets; (ii) inwardly directed flow to oppose droplet cloud expansion (caused by electrostatic repulsion) utilizing aerodynamic flow focusing; and (iii) selective positioning, e.g., off-axis, of the MS inlet to increase the likelihood of collecting highly charged and mostly desolvated droplets. DRILL adopts the first principle to as limited an extent as possible to preserve the electrospray ionization softness, and completely abandons the second and third approach, instead introducing novel and more effective strategies enabled by the exploitation of vortical flow.

The effect of a vortical flow, which induces a pseudo-body force directed radially outwards, is an efficient mechanism to separate and sort electrosprayed charged droplets subjected to a rotational motion. This chapter is dedicated to presenting the device designs used for vortex generation, and droplet separation and transport in the context of integration into ESI-MS workflows. Lessons learned during MS characterization led to different DRILL designs, from Gen 1 to Gen 3, aiming at capturing the opportunities for improvements in analytical outcomes and more robust operation. The first embodiment of DRILL device, 'Gen 1', decoupled the vortical flow creation unit and the droplet sorting unit with electrospray injection normal to the translational jet flow. Vortex generation in Gen 1 is similar to hydrocyclone separators [83] with tangential inlets for gas entrance and a conical outlet for vortex convergence. The geometry used for Gen 1 provides a baseline structure, and the successive generations of DRILL design (Gen 2 and Gen 3) are derived

with modifications aimed for enhanced ability to produce stable electrospray and increased transmission of ion current into the MS inlet.

## 4.1 Gen 1 DRILL

### *4.1.1 Device Description*

Figure 4.1c displays the Gen 1 prototype used for establishing the conceptual understanding and design fundamentals (via simplified modeling of key phenomena) and performing foundational MS experiments to validate the basic DRILL concepts. It is a cylindrical device with the total length of 15 cm and the diameter of 5 cm. It consists of two units for flow creation and droplet sorting (Figure 4.1a). The flow-creation section in the back (#2) allows gas entrance directed tangentially into the annular gap between the inner cone (#5) and the outer union (#3) for swirling flow development (Figure 4.1b). Then, the flow converges into the droplet sorting unit to increase its angular velocity due to momentum conservation (Figure 4.1d). In the droplet sorting unit, the electrospray plume is introduced from the orthogonally oriented spray emitter (#4) into the converging vortex, and charged droplets are carried by the vortical flow to leave the device through the 2 mm ID front (or exit) electrode tube (#9) facing the MS inlet. Multiple adjustments in electrode positions and the converging annulus between the inner cone (#3) and the outer converging joint (#6) are possible leading to alterations in the velocity and electric fields guiding the trajectory of electrosprayed droplets. The modular design allows for many operational configurations/ degrees of freedom for manipulation of droplet trajectories. Design ideas, modeling and realization of the Gen 1 DRILL are primarily contributed by Dr. Peter Kottke [84] and discussion is included here for continuity of presentation, as it provides the

foundation for evolution of Gen 2 and Gen 3 devices, the original contributions of this thesis research.

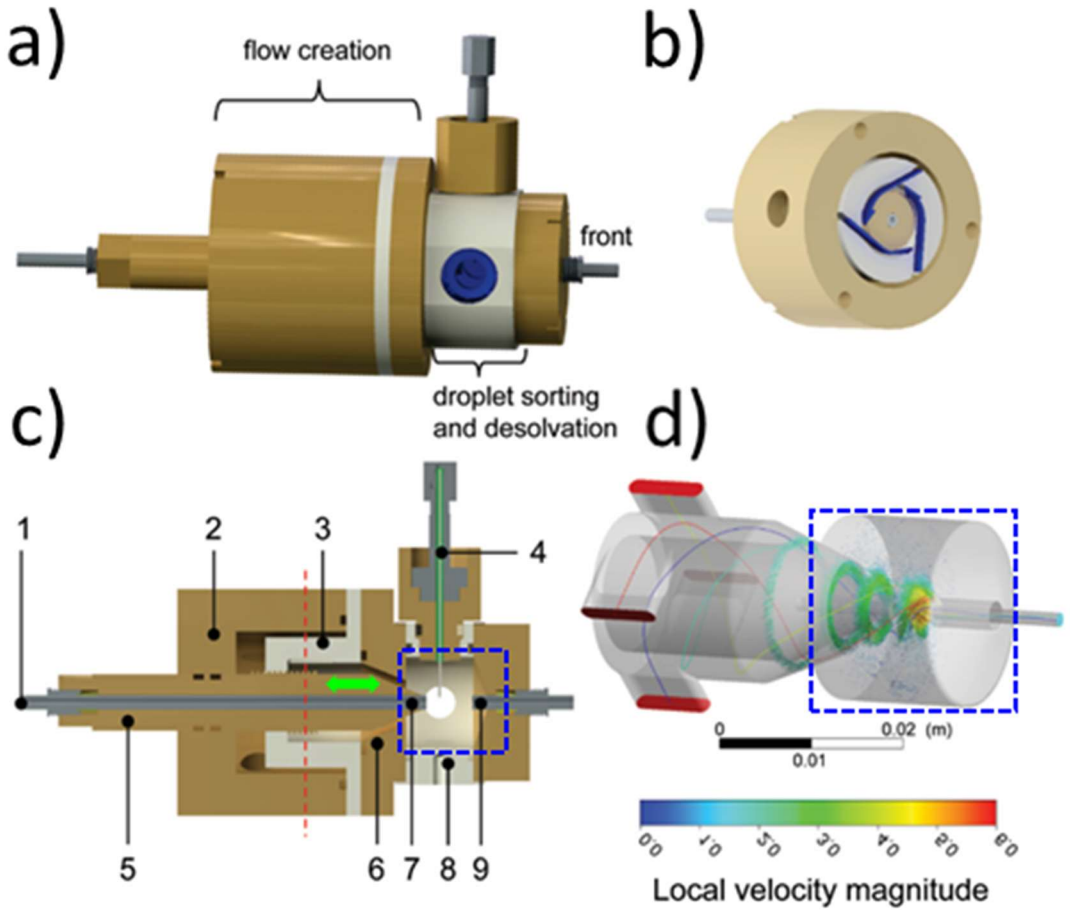


**Figure 4.1. (a) Schematic of Gen 1 DRILL prototype (courtesy of Peter A. Kottke). (b) Cross section of the vortical flow generation unit corresponds to the red dashed line shown in c. (c) Cross sectional view of assembled Gen 1 DRILL. (d) Vector field and velocity magnitude map of the swirl converging into the droplet sorting unit.**

Figure 4.2 displays the setup of Gen 1 DRILL in front of an LTQ Orbitrap mass spectrometer. Ultra high purity (UHP) nitrogen is supplied via a port on the back from a pressurized gas cylinder. Pressure of the gas supply to DRILL is controlled from 2 kPa to 3.5 kPa (gage pressure) using a Swagelok backpressure regulator and monitored via a pressure gauge (max range 20 kPa).

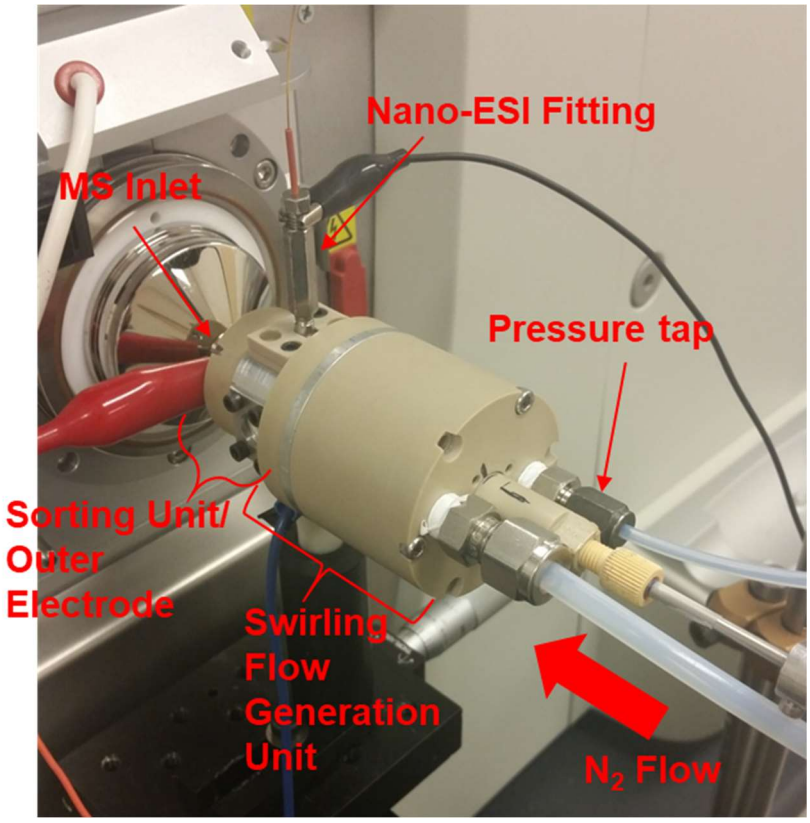


**Figure 4.2. Setup of Gen 1 DRILL facing an LTQ Orbitrap mass spectrometer**

*4.1.2 Flow Field in Gen 1 DRILL*

The flow rate of gas entering the DRILL device is related to the pressure difference across DRILL, $\Delta P$ by

$$\dot{Q}_{gas} \approx A_{tube}\sqrt{\Delta P / \rho_{gas}} \tag{4.1}$$

The entering swirl velocity is estimated using $v_{\theta,entrance} \approx \dot{Q}_{gas} / A_{swirler}$. The swirler area $A_{swirler}$ is adjustable via a threaded union allowing for fine-tune positioning of the inner cone (green arrow in Figure 4.1c). As the swirling flow enters the 2 mm ID front tube, the radius of rotation decreases to the tube ID, maximizing the swirl velocity at the entrance to

the front tube. According to the conservation of angular momentum (neglecting viscous dissipation), the exit swirl velocity is determined using

$$u_{\theta,exit} \approx u_{\theta,entrance} \frac{r_{swirler}}{r_{exit}} \tag{4.2}$$

The flow field in Gen 1 DRILL is solved using ANSYS Fluent with pressure inlet and outlet boundary conditions based on the experimental pressure measurement in DRILL (~3.5 kPa). The simulation results are highlighted in Figure 4.3 showing the spatial evolution of the swirl and axial velocities in the region near and inside the exit tube. The simulated maximum swirl and axial velocities occur at the entrance of the front tube, and the trend agrees to the prediction using Eqs (4.1) and (4.2) within an order of magnitude.

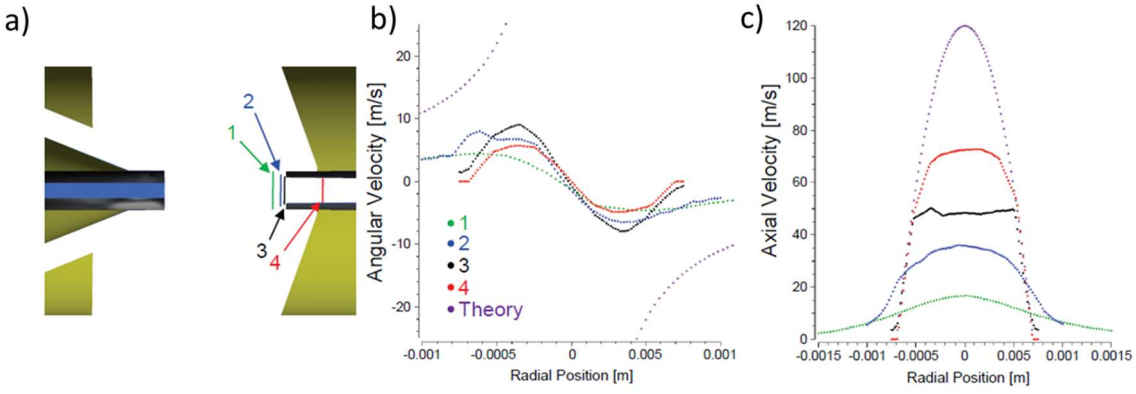


**Figure 4.3. (a) Schematic of the locations within DRILL for which flow variables are extracted. The region shown in (a) corresponds to the blue dashed box in Figure 4.1c. Positions range from just under 1mm away from the front electrode tube inlet, inside the sorting unit (1 – green) to almost 2mm inside the front electrode tube (4 – red). (b) Comparison of predicted angular velocity shown using Eq (4.2) to simulated swirl velocity at locations 1 – 4. (c) Comparison of axial velocity predicted by assuming flow rate determined by 3.5kPa pressure drop at the front electrode tube inlet using Eq (4.1) to the simulated axial velocity at locations 1 – 4.**

### *4.1.3 Electric Field Control in Gen 1 DRILL*

A unique aspect of Gen 1 is that the device contains four electrodes that can be individually biased with electrical potentials: the potential applied to the emitter, $V_{spray}$, the potential applied to the outer shell electrode, $V_{shell}$, the potential applied to the back electrode $V_{back}$, and the potential applied to the front electrode, $V_{front}$. The combination of the electrical biases needs to produce the electric field at the emitter capillary tip with magnitude $E_{ESI}$ for electrospray to occur, which is estimated as [44],

$$E_{ESI} = \sqrt{\frac{\gamma}{l_s \varepsilon_o}} \tag{4.3}$$

where $\gamma$ is the surface tension of the solvent being sprayed, and the length scale, $l_s$ is given as $\frac{r_c}{2cos\theta}$. $r_c$ is the spray capillary radius, and $\theta$ is the spray cone half angle. Due to the absence of the capability to measure the electric field inside the device, the electrical potential fields are evaluated numerically using a user-defined scalar in ANSYS Fluent. The numerical method used neglects space charge effects such as that due to the presence of a charged droplet plume. The numerical procedure used is presented in Appendix C.

For any given geometry, simulations predict the electric field strength at the ESI tip as a linear combination of the DRILL electrode potentials (Appendix C). The ion current is experimentally measured at the capillary tip with the geometry held constant over a wide range of DRILL electrode potentials. Figure 4.4 plots the measured spray currents vs the predicted electric field strength at the tip. Each data point is a result of a unique combination of four electrical potentials. The spray condition and spray currents appear to be primarily functions of the local field strength at the tip regardless of different potential combinations. This suggests that different combinations of electrical potentials may be

exploited to direct ions to the desired trajectories without altering the electric field intensity locally near the tip as required for electrospray.

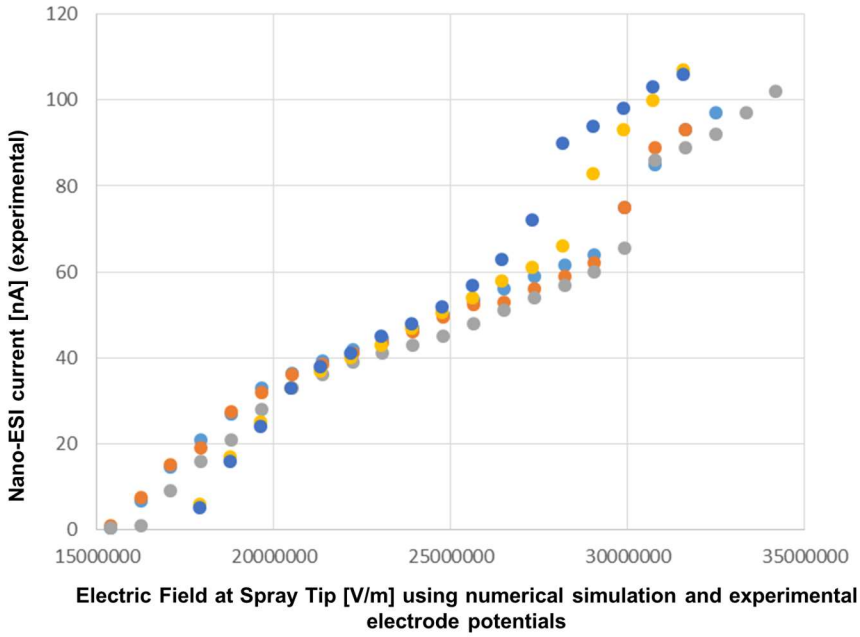


**Figure 4.4. Experimental validation of approach to maintaining electric field strength at the required magnitude for electrospray from capillary emitter tip while changing DRILL potentials, which can be used for control of droplet motion.**

### *4.1.4 Droplet Sorting in Gen 1 DRILL*

The trajectories and fates of electrosprayed charged droplets are the result of the coupled effects of the flow and electric fields in DRILL. Fluent's discrete phase model is used to obtain the droplet trajectories as shown in Figure 4.5 (note that simulations are simplified as they ignore the space-charge effects associated with a plume of charged droplets). The geometry and the flow/electrical conditions used match those for the experiments discussed in Chapter 5. Simulations show that droplets greater than 3$\mu$m are flung outwards due to the centrifugal force, end up landing on the exit tube, and are lost

[84]. On the other hand, smaller droplets are rapidly carried towards the front tube by the drag force and leave DRILL to enter the mass spectrometer. The inertial effect in Gen 1 is demonstrated to prevent larger droplets (> 3 $\mu$m in diameter) from leaving DRILL, leading to selective transfer of small droplets into the exit tube and subsequently to the mass spectrometer for analysis.

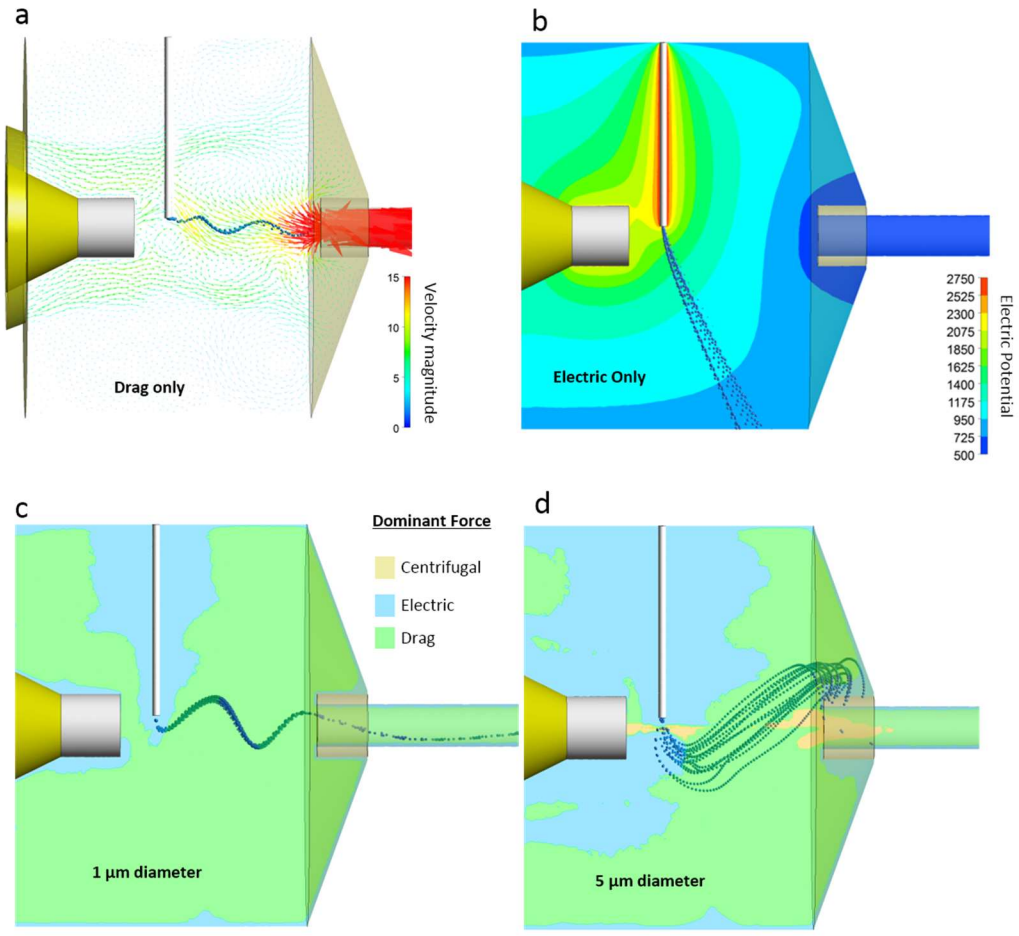


**Figure 4.5. Simulated droplet fates demonstrating the roles of different forces. (a) Droplets with zero charge and mass follow the fluid flow, indicated via the vector arrows on the symmetry plane of DRILL, and all would exit DRILL (b) charged, massless droplets with zero drag would be driven to the outer shell by the electric field within DRILL. With all forces considered, droplet fate depends on size. Panels (c) and (d) display the spatial distribution of the most dominant force indicated in solid colors, the inertial effect that leads to the centrifugal pseudo-force (yellow), the electric force (blue), and the drag force (green).**

These simulation results are supported by electrical current measurements on the DRILL electrodes using a picoammeter that show more than 80% of the electrospray current ends up on the front electrode tube, with this loss increasing with increasing gas flow rate into DRILL. This is attributed to the effect of intensified swirling, which drives droplets outwards and prevents them from entering the DRILL exit tube facing the MS inlet. Additional losses of ions occur between the exit tube and the MS inlet due to flow dispersion and plume expansion, leading to poor ion transmission efficiency into the MS inlet (< 5%). As a result, Gen 1 DRILL demonstrates a sevenfold lower rate of populating the Orbitrap mass analyzer with ions as compared to conventional ESI without DRILL. Figure 4.6 shows a comparison of ion fluxes measured in the Orbitrap with varying analyte concentration via the three infusion methods, Gen 1 DRILL, direction infusion with the same ESI emitter, and a commercial Flex ion source. The low ion flux with Gen 1 DRILL results in a reduced MS signal, which motivates a need for design improvements aiming to increasing the fraction of electrospray droplets transmitted from DRILL into a mass spectrometer while still achieving an increase in the quality of droplets delivered.

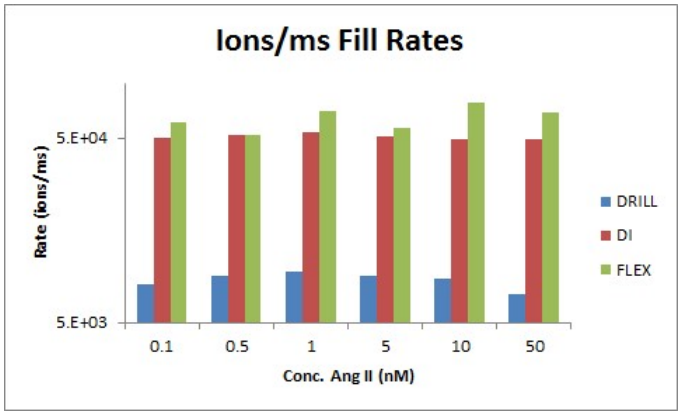


**Figure 4.6. Comparison of ion fill rates between Gen 1 DRILL, direct infusion (DI) and Flex ion source in Orbitrap mass spectrometer.**

Another improvement needed is related to low electrospray stability indicated as the relative standard deviations (RSD) of analyte ion currents. Figure 4.7 compares the extracted ion chromatograms corresponding to three analyte peaks for Ultramark 1621 (MS calibration mixture) between ESI and Gen 1 DRILL. With Gen 1 DRILL, the higher RSDs indicate reduced electrospray stability in DRILL vs baseline ESI. This lower stability is presumably attributable to an effect of the orthogonal orientation of the electrospray and bulk motion of the flow and motivates a shift to electrospray oriented coaxially with the flow in Gen 3 DRILL to yield a more stable MS signal with low RSD.

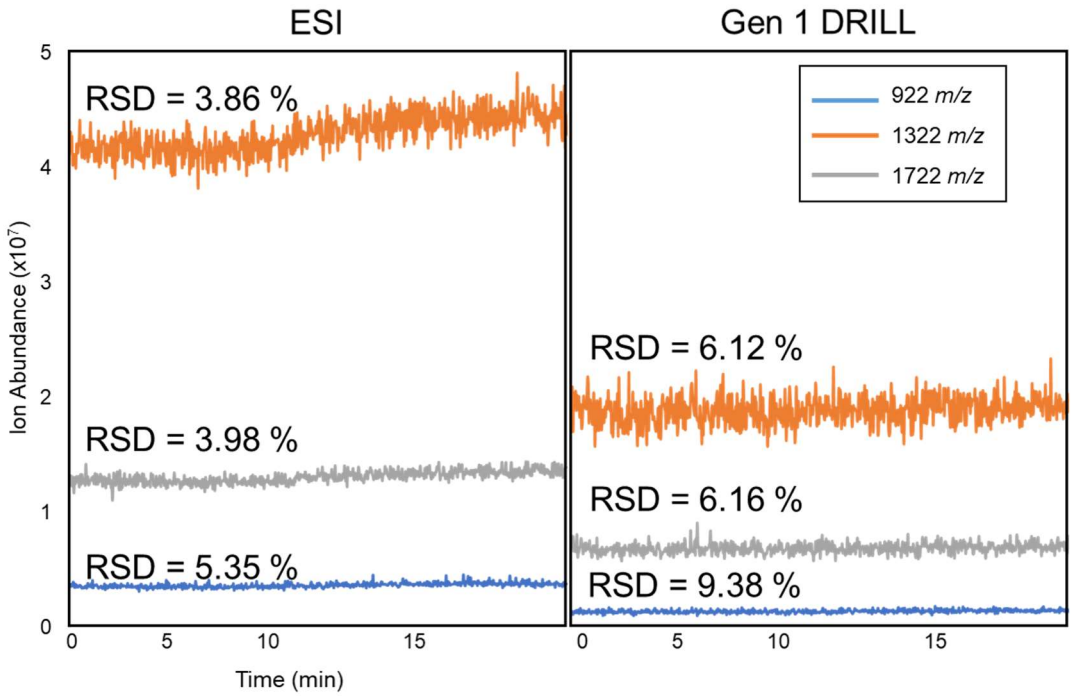


**Figure 4.7. Comparison of extracted ion chromatograms of 922 m/z, 1322 m/z, and 1722 m/z from Ultramark 1621. The sample flow rate used is 1 $\mu$L/min.**

While Gen 1 DRILL successfully demonstrates inertial droplet separation for enhanced capture of smaller droplets (Chapter 5), further enhancements in ion transmission

and electrospray stability are sought for a boost in MS signal intensities and to achieve more reproducible and robust MS data acquisition.

## 4.2 Gen 2 DRILL

The next generation DRILL device, called ‘Gen 2’, inherits many of the Gen 1 DRILL features but without the front tube and the concave front-end (Figure 4.8a) thus opening the flow for free expansion outside of the DRILL sorting unit. The main goal of the Gen 2 DRILL design is to improve the current transmission into the MS by eliminating major losses of the electrospray current observed in Gen 1 DRILL. Here, the swirling flow carrying the electrosprayed droplets is directly coupled to the MS inlet without passing through the front tube: The swirling gas stream exits DRILL through the large cross-sectional area of the outer shell with some fraction of the gas and a portion of the desireable small, highly charged electrospray droplets being sucked into the MS inlet by vacuum draw. Results obtained with Gen 2 DRILL also provide some insight into the impact of the coupling between the swirling flow with the suction flow into the MS.

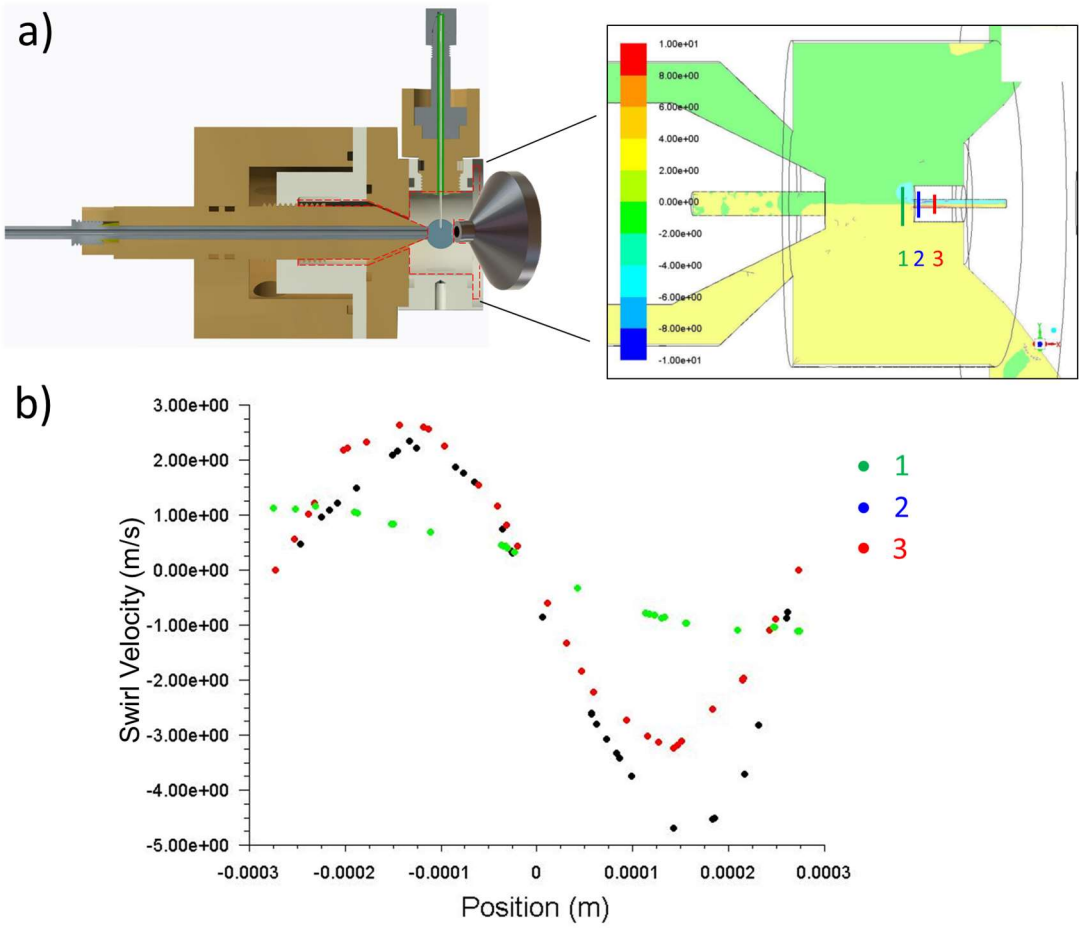


**Figure 4.8. (a) Gas flow region in Gen 2 DRILL: red dotted outline corresponds to the right panel. Positions range from 1 mm away from the MS inlet (1 – green) to 1 mm inside the MS inlet (3 – red). (b) Simulated swirl velocity at locations 1 – 3.**

Figure 4.8c displays the swirl velocity at the locations ranging from 1 mm away from the MS inlet (1 – green in the expanded view of Figure 4.8a) to 1 mm inside the MS inlet (3 – red). In this model, the boundary conditions are set such that the swirling jet flow rate matches the suction rate (1.6 L/min). The swirl velocity at 1 mm before the MS inlet is lower (~1 m/s) compared to that in Gen 1 DRILL but increases up to 5 m/s as the flow sucked into a small ID MS inlet. Low swirl velocities lead to reduced inertial effects, allowing an increased fraction of electrospray droplets to enter the MS inlet, although at a detrimental effect of reduced size-selective droplet sorting. As a result, the ion flux via Gen

2 DRILL to the orbitrap analyzer is measured to be at least two-fold greater compared to that via ESI, increasing MS signal intensities. This is the key advantage of the Gen 2 design over Gen 1 with ~7 times lower ion flux vs ESI due to major ion current losses on the front electrode tube.

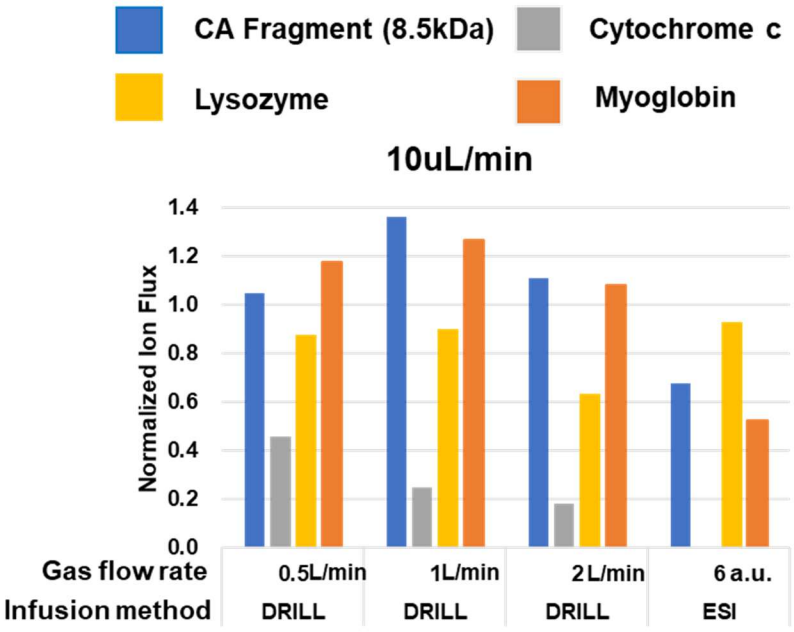


**Figure 4.9. Deconvoluted protein peak intensities normalized to those without DRILL swirling flow. Sample solution containing different protein mixtures was infused at 10 $\mu$L/min. The ion flux on the y-axis is normalized to that with zero flow rate in DRILL.**

Despite increased ion flux which leads to increase in MS signal intensity, no significant improvement in signal-to-noise ratio (SNR) is observed using Gen 2 DRILL vs ESI (Figure 4.10). More discussion of DRILL performance for increase in SNR and MS sensitivity will follow in Chapter 5. However, it is worth noting that high SNR is desirable as it improves the ability of MS to distinguish the analyte signal from the background noise. SNR, as a measure of abundance in analyte ions relative to local noise level, can be an indicator to determine MS sensitivity. In Figure 4.10, the slightly higher SNR using Gen 2

DRILL at lower gas flow rates suggests lack of inertial droplet separation that leads to efficient transmission of analyte ions and small droplets with less amounts of species that contribute to elevated noise level (e.g., background ions, solvent molecules). Even at higher gas flow rates, the 2-fold improvements in SNR using higher gas flow rates (>7 L/min) vs ESI are still lower than 10-fold improvements achieved in Gen 1 DRILL (in reference to Figure 5.3). Less improvements in SNR via Gen 2 DRILL vs Gen 1 DRILL motivate design modifications to achieve pronounced inertial sorting effects while ensuring improved ion transmission.

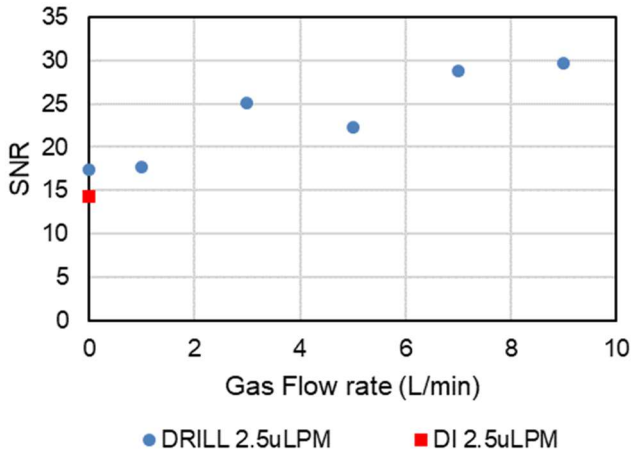


**Figure 4.10 Signal-to-noise ratio (SNR) of 50 nM cytochrome-c protein at m/z=885$^{+14}$ with varying gas flow rate in Gen 2 DRILL vs direct infusion (DI). The liquid flow rate used is 2.5 $\mu$L/min.**

## 4.3 Gen 3 DRILL

With Gen 2 DRILL, a preliminary investigation into the effects of the relative flow rate between the swirling flow and the suction into a mass spectrometer is performed so that the finding can guide DRILL design for improved ion transmission for MS analysis.

As discussed in Chapters 2 and 3, efficient transmission of flow into the MS is advantageous for increasing the total current and most likely improved transmission of analyte ions into MS. Figure 4.9 clearly shows the effects of the relative flow rate between the two flows on the MS signal response for a mixture of four intact proteins (8.5 kDa carbonic anhydrase, cytochrome c, lysozyme, and myoglobin). The spectral intensity peaks for three proteins out of four increase with increasing gas flow rate to 1 L/min but drop with further increase in flow rate to 2 L/min. Given that the flowrate into the MS inlet is between 1 L/min and 1.6 L/min, the optimal analyte detection may occur when the source swirling flow rate closely matches the suction rate. This expected trend of the MS response to varying flow rate is confirmed in results on Figure 4.9 and provides useful DRILL design and operation input for the design features allowing for improved flow transmission. These are incorporated into Gen 3 DRILL design as described next.

Gen 3 DRILL presented in Figure 1.6 (Chapter 1) is a cylindrical device 30 mm long and 36 mm in diameter. The device has two major modifications as compared to the previous two generations of DRILL: (1) the electrospray capillary is placed coaxially with the MS inlet for enhanced spray stability and (2) a swirling jet exits the aperture/ nozzle of diameter close to that of the MS sampling orifice, allowing for improved flow transmission and entrainment of the electrospray plume. Electrospray in Gen 1 and 2 DRILLs is introduced normal to the vortical flow and is often accompanied by undesirable phenomena such as pulsation and liquid accumulation at the spray tip, causing poor spray stability and MS signal degradation or complete loss. In Gen 3 DRILL, an electrospray capillary emitter is inserted into the 1/32” diameter hole in the center of the inner cone to be concentric with the vortex generating nozzle and held in place by a finger-tight fitting

in the back so that the extension of the emitter tip from the nozzle can be finely adjusted for most effective gas-spray coupling. The concentric emitter – nozzle arrangement is an important improvement over the configuration in the early generation DRILLs yielding more stable and reproducible electrospray. The converging vortex created in the annular channel exits 1 mm diameter nozzle facing the MS inlet (0.6 mm ID) directly.. The nozzle diameter is an important design feature to prevent swirling jet growth radially to an extent much greater than that of the MS inlet. The swirling jet that leaves Gen 3 DRILL has the initial jet diameter comparable to the MS inlet ID, allowing for retention of vortex and efficient flow transmission. This is an improvement over previous DRILL generations in which the swirling flow exits a larger nozzle making it more difficult to achieve complete coupling with the MS suction. The flow rate of gas entering the swirler is monitored by a mass flow meter and controlled by a pressure regulator upstream of the flow meter such that the flow rate matches the suction rate into the MS inlet. DRILL is clamped on an XYZ micro-translation stage for fine-tuning of the alignment and the distance between the nozzle and the MS inlet.

With these design modifications, Gen 3 DRILL demonstrates significantly improved signal stability and transmission of ions into the mass spectrometer. Ion current chromatograms acquired via baseline electrospray (no DRILL) and Gen 3 DRILL are shown in Figure 1.6. With coaxial electrospray in Gen 3 DRILL, the corresponding ion chromatograms are much steadier, exhibiting up to a six-fold lower relative standard deviation (RSD) as compared to baseline ESI-MS. In MS analysis, spray stability is correlated to spectral quality and analytical performance as suggested by numerous investigations on the effects of different spray modes [85, 86]. Establishing electrospray

with improved stability is a key to reproducible and precise measurements of analyte ions, especially for long analytical runs in HPLC-ESI-MS of complex biological samples.

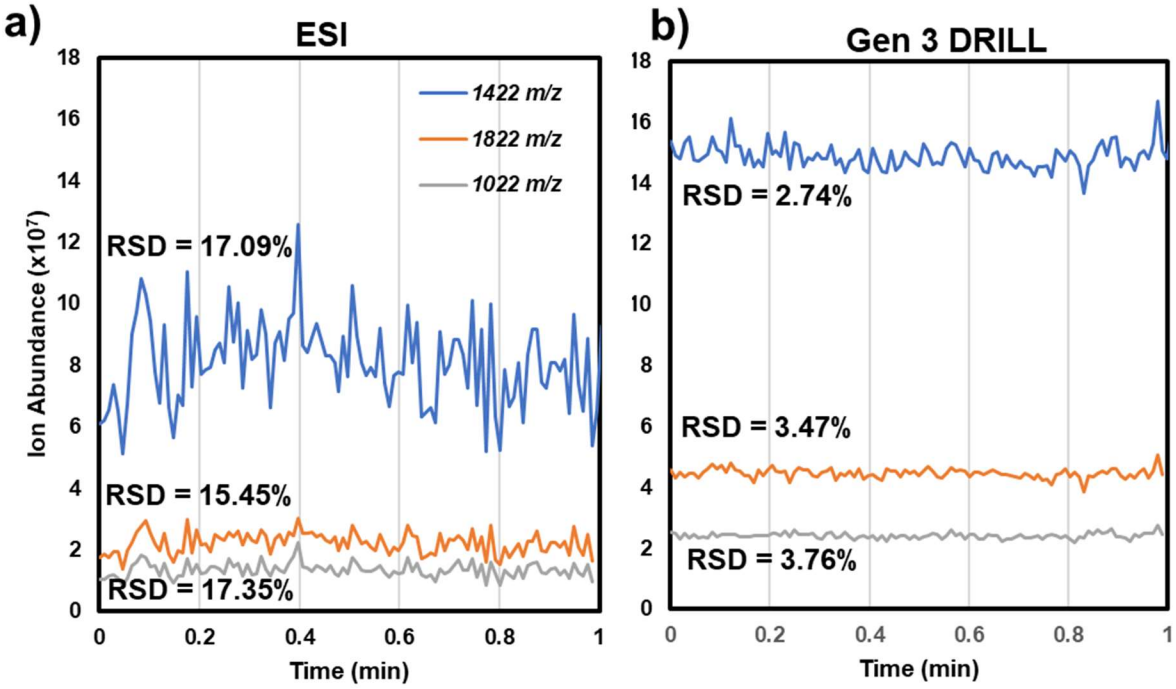


**Figure 4.11 Comparison of extracted ion chromatograms of mass-to-charge ratio m/z = 1022, 1422, and 1822 from Ultramark 1621. The sample flow rate used is 500 nL/min. (a) Baseline ESI-MS demonstrates chromatograms with much greater relative standard deviations (RSD), i.e., lower robustness and stability, as compared to (b) Gen 3 DRILL, which shows remarkably low RSD across all m/z of species analyzed.**

# CHAPTER 5. DRILL ESI-MS CHARACTERIZATION AND APPLICATION CASE STUDIES

The application of the DRILL interface to mass spectrometry has been demonstrated by analyzing peptides, proteins, and a mixture of fluorinated polymer molecules with varying physico-chemical properties. The beneficial effects of droplet inertial sorting and separation using a vortical flow in DRILL on the analytical performance of ESI-MS, which manifested both in higher signal-to-noise ratio (SNR) and also improved (lower) limit of detection (LOD), are demonstrated. Also, DRILL's capability for selective transmission of smaller droplets is exploited to induce a shift in analyte peak distributions with increased abundance of hydrophobic ions.

The DRILL interface has been successfully demonstrated in conjunction with a number of mass spectrometers, including Time-of-Flight MS (micrOTOF, Bruker Daltonics), Orbitrap MS (LTQ-Orbitrap XL, Thermo Fisher Scientific), and Triple-Stage Quadrupole MS (TSQ Vantage, Thermo Fisher Scientific). These application case studies of the DRILL interface provide evidence of the improvement obtained in ESI-MS workflows by exploiting the benefit of charged droplet separation based on size, which enables selective capture of small, highly charged droplets to produce improved quality of MS spectra. Of particular significance, the MS case studies highlight DRILL's ability to produce an order-of-magnitude improvement in LOD and SNR [84].

Additionally, MS case studies with mixtures of peptide/proteins (e.g., angiotensin I and II, MRFA, neurotensin, cytochrome c, carbonic anhydrase) at different concentrations

and fluorinated polymer molecules (Ultramark 1621) with different surface activity (hydrophobicity) provide data that links the fundamental theoretical (Chapter 2 and 4) and experimental (Chapter 3) studies on inertial separation/ sorting in DRILL to their resulting effects on the analyte detection in mass spectrometry applications. Unless otherwise noted, all analytes are added to a solution containing 50%:50% methanol/water with 0.1% formic acid (v/v).

## 5.1 Improved Signal-to-Noise Ratios and Limit-of-Detection

Several representative peptides and proteins have been identified with the Gen 1 DRILL interface coupled to a triple quadrupole (TSQ) mass spectrometer and an Orbitrap mass spectrometer. Sensitivity is enhanced, indicated by both higher signal-to-noise ratios and lower limit of detection.

Figure 5.1 compares the mass spectra of a 5 $\mu$M sample of equine heart cytochrome-c (12000 Daltons) via ESI to Gen 1 DRILL-ESI at 2 $\mu$L/min using a TSQ mass spectrometer. Cytochrome-c is a peripheral protein bound to the mitochondrial membrane in the respiratory chain of all aerobic organisms. The protein has been used as a model molecule for structural characterization of large biomolecules due to its high similarity in structure with other variants [87]. Figure 5.1 depicts the peaks that correspond to the charge states from +10 to +19. (The charge state indicates the number of positive or negative charges attached to an analyte ion.)

In Figure 5.1b, the mass spectrum obtained via DRILL-ESI-MS shows cleaner spectra with reduced noise as compared to standard ESI-MS. These mass spectral characteristics are associated with ions derived from small offspring droplets, extracted

from the electrospray plume by DRILL, and leading to substantial reduction of the background noise that is associated with incomplete desolvation and residual chemical contaminants.

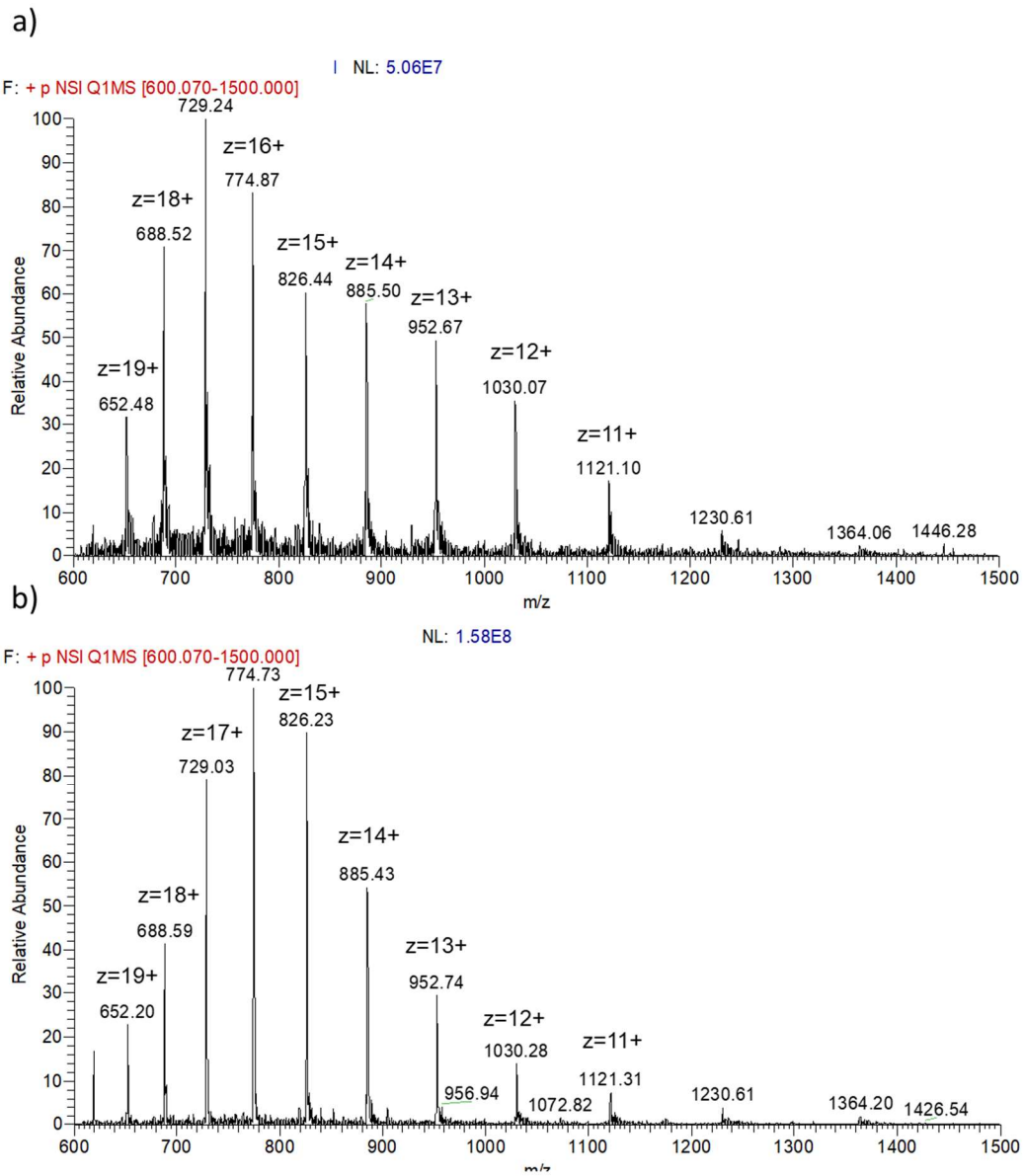


**Figure 5.1. Mass spectrum from a triple quadrupole mass spectrometer for 5$\mu$M cytochrome c in 50:50 (v/v) water/methanol with 0.1% acetic acid via (a) ESI and (b) Gen 1 DRILL-ESI. The sample flow rate used is 2$\mu$L/min.**

Charge state distributions of protein ions carry information about protein conformations (e.g., folding, denaturation) in the solution phase [88, 89], and in turn, droplet populations from which the analyte ions are derived. In an ESI plume, the solvent composition within electrosprayed droplets vary depending on the droplet size [54]. Large primary droplets with lower evaporation rate maintain the aqueous vs organic solvent composition close to its initial 50%-50% state in which protein unfolding is induced leading to increase in charge binding sites. On the other hand, volatile organic solvents (e.g., methanol) preferentially evaporate from small offspring droplets with higher desolvation efficiency, and hence small droplets are enriched with water [54]. In more aqueous small droplets, cytochrome-c molecules preferentially assume a folded state which reduces available charge binding sites, resulting in a shift to lower charge states (higher m/z) in the MS spectra [54] (Figure 5.2b). Fenn [10] suggested that formation of gas-phase ions with low molecular weight (<30kDa [90]) is believed to be a result of direct emission of analyte molecules. Ion evaporation may occur when the repulsive interaction between the electric field on the droplet surface and surface excess charge attached to the molecule is intense enough to separate the analyte from the droplet surface.

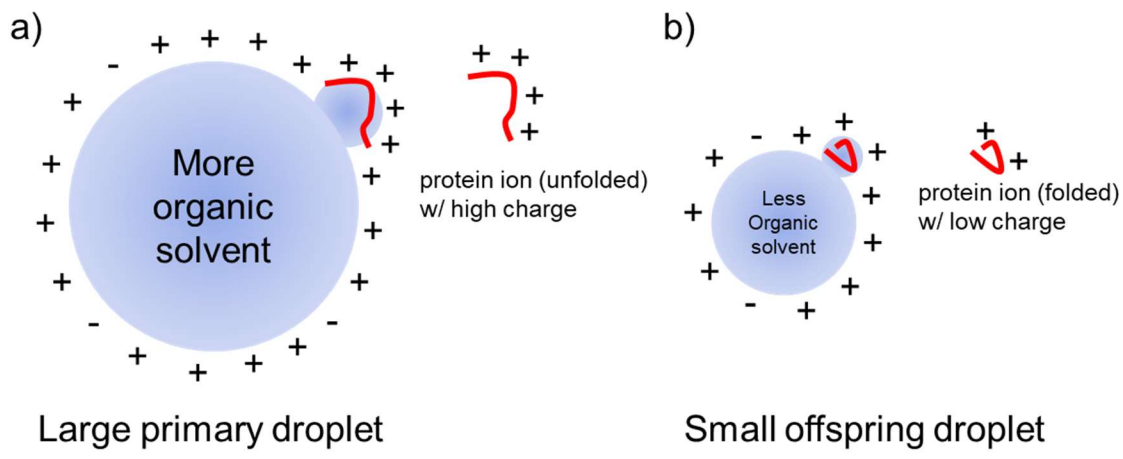


**Figure 5.2. Schematic of ion evaporation from (a) large primary droplet and (b) small offspring droplet. In large primary droplets with solvent composition close to that of the infused solution, protein molecules become denatured, increasing the number of available charge sites. In small aqueous droplets, proteins assume a folded state.**

Figure 5.2a depicts analyte ion emission that may occur on the surface of a large droplet. Despite the lower surface excess charge concentration, the local field strength between the surface charge and the highly charged ion may cause the analyte ion to leave the droplet surface. The mass spectrum obtained via conventional ESI (Figure 5.1a) displays a maximum intensity peak at m/z of +17. With DRILL-ESI, ions with +16 charge appear most abundant, indicating a shift in the charge state distribution to lower m/z. This shift in the charge state when DRILL is used is indicative of improved collection of smaller droplets where cytochrome-c exists in more folded conformation with a greater number of charged residues per molecule (lower m/z).

Signal-to-noise ratios (SNR) can also be used as a measure to infer information about droplet populations introduced to MS via standard ESI vs DRILL-ESI. Figure 5.3a compares the mass spectra of a blank solution (water:methanol 50:50) infused at 450 nL/min on a triple-stage quadrupole mass spectrometer in the positive ion mode. With Gen

1 DRILL, the abundance level of background ions is seen to be significantly reduced due to preferential exclusion by vortical gas flow of larger droplets. Figure 5.3b and 5.2c show the signal intensity (spectral peak height $S_H$) of 25nM angiotensin I (1296.5 Daltons) at +3 charge state without and with DRILL, respectively. Comparing the peak-to-peak value ($N_{pp}$) of baseline noise in two different mass-to-charge ranges around the selected +3 charge state, ESI-MS with DRILL shows a ten-fold improvement in signal-to-noise ratio (SNR). Reduction of noise due to residual solvent and chemical contaminant its carries results in an improved (lower) limit of detection (LOD), which is an important metric for analysis sensitivity.

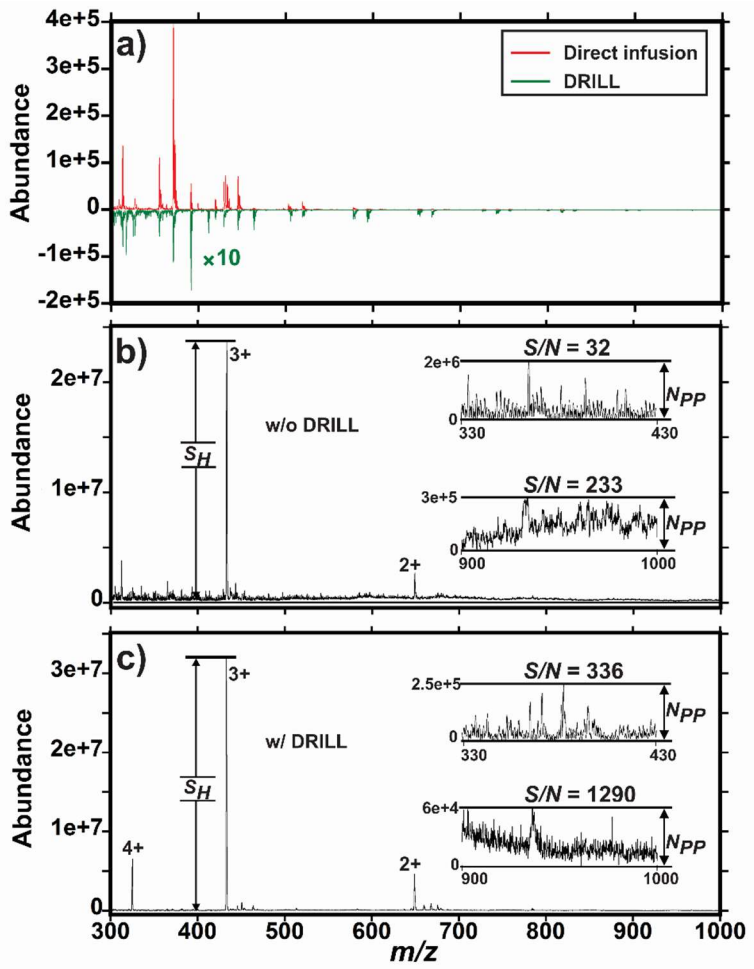


**Figure 5.3. Signal-to-noise ratios (SNRs) on a TSQ mass spectrometer of offline direct infusion (DI) ESI and Gen 1 DRILL-ESI with angiotensin I. The sample flow rate used is 450 nL/min. (a) Mass spectra for direct infusion ESI (red) and ESI-DRILL (green) of blank ESI solutions (50:50 water:methanol, 0.1% TFA) infused in positive ion mode, (b) SNR in ESI mass spectra of angiotensin I (25nM) using direct infusion, and (c) ESI-DRILL. SNR is calculated using the signal height ($S_H$) at the center of the +3 charge state of angiotensin I (m/z = 432.89) analyte mass peak and peak- to peak noise amplitude ($N_{pp}$) [91]. SNR is significantly improved in ESI-DRILL (S/N = 1290) compared to direct infusion ESI (S/N = 233). Data displayed in Figure 5.3 have been obtained by the Muddiman group at NCSU using Gen 1 DRILL device developed as part of this dissertation [84].**

Figure 5.4 displays the abundance of ions (y1 – y8) produced by fragmenting +3 (Figure 5.4a) and +2 (Figure 5.4b) charge state ions of angiotensin I as a function of analyte concentration. The product ions indicated as y ions are collected via selected reaction

monitoring (SRM) on a triple quadrupole mass spectrometer. In the SRM mode, two quadrupole mass analyzers (Q1 and Q3) are coupled together. The +3 and +2 charge state precursor ions are selected by the Q1 filter, and the isolated ions are subjected to dissociation in Q2. The fragment ions (y1 – y8) are collected in Q3. This method can be used for protein sequencing. Here, no signal is observed below 1 nM for direct infusion ESI conditions (i.e., no DRILL). Using Gen 1 DRILL-ESI, ions are detected down to 4-fold lower concentrations over direct infusion. The lower LOD is attributed to enhanced capture of small droplets containing fewer solvent molecules and adducts, resulting in high quality mass spectra with reduced noise.

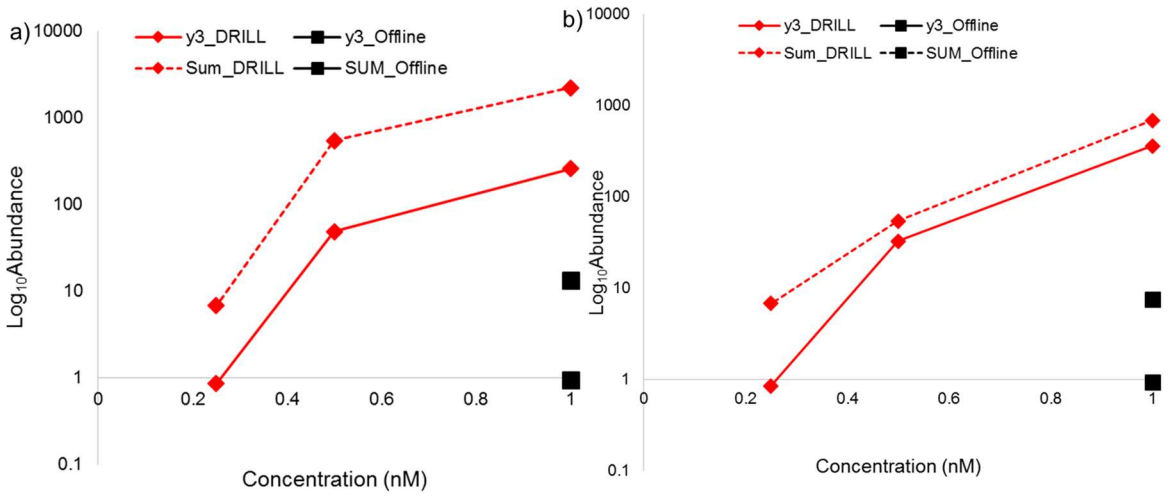


**Figure 5.4. Improvement in LOD enabled by Gen 1 DRILL (red) detecting angiotensin I (50:50 methanol:water, 0.2% formic acid) at 4-fold lower concentrations over nano-ESI conditions (black). The average abundance of y1 – y8 product ions are monitored for the (a) +3 and (b) +2 charge state of angiotensin I in the selected reaction monitoring (SRM) mode (Q1/Q3 filters) on a TSQ Vantage. The solution flow rate used is 300nL/min through a 15µm tip. Data displayed in Figure 5.4 have been obtained by the Muddiman group at NCSU using Gen 1 DRILL device.**

The same effects of reduced noise levels and improved limit of detection for angiotensin II (1046.2 Daltons) are observed via Gen 1 DRILL on an LTQ orbitrap mass

spectrometer [84].Figure 5.5a highlight that the DRILL spectrum with less local noise in the vicinity of the +2 charge state peak vs nano-ESI. Figure 5.5b displays the LOD of angiotensin II, showing an order of magnitude improvement with DRILL (0.1 nM) over direct infusion ESI (1 nM). As shown in Figure 5.5c, DRILL is introducing the highest ratio of analyte ions relative to top twenty non-target ions into the MS of all methods, leading to improved signal-to-noise ratio which is consistently observed with use of DRILL. Up to 10-fold lower abundance of background ions (e.g., triethylanine, dimethyl phthalate, etc) via DRILL vs nano-ESI [84] is attributable to use of high purity gas flow which reduces appearance of impurities/ background common to ESI-MS.

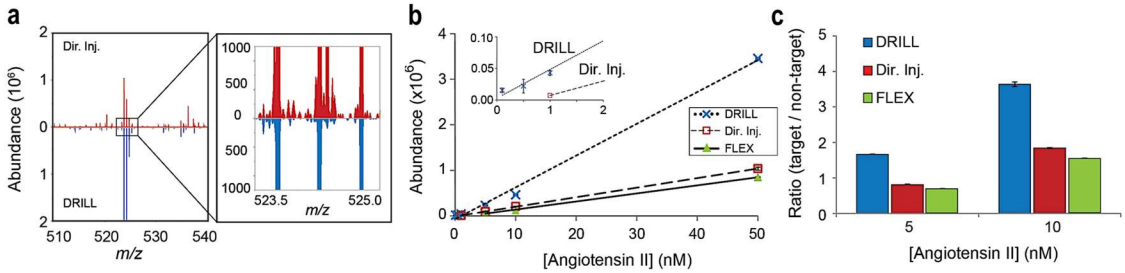


**Figure 5.5. (a) Comparison of mass spectra encapsulating +2 charge state peaks of angiotensin II on the LTQ Orbitrap. (b) Limit of detection (LOD) using Gen 1 DRILL, nESI, and Flex nESI source (Thermo Scientific, ES071) as a function of concentrations from 0.1 to 50 nM angiotensin II. Peak height is normalized to injection time. (c) Ratio of analyte peak intensity to the some of top twenty non-analyte peak intensities. Data obtained in collaboration with the Torres group at Georgia Tech; Data analysis was performed by Alex Jonke [84].**

Figure 5.6 shows the results of applications of Gen 1 DRILL to a top down ESI-MS proteomics approach, which is used for analysis of intact proteins. Solutions containing carbonic anhydrase (CA, 29 kDa) with concentrations from 1 nM to 1000 nM are infused into an Orbitrap mass spectrometer. Spectral analysis reveals fragments of CA (8.5 kDa and 15 kDa) in addition to the full protein with a molecular mass of 29 kDa. Three spectral

peaks at m/z of $714^{+12}$, $1114^{+14}$, and $1262^{+23}$ corresponding to 8.5 kDa, 15 kDa, and 29 kDa, respectively, are analyzed for the limit of detection. DRILL detects the +12 charge state ions at 714 m/z and +14 charge state ions at 1114 m/z down to 50 nM and 100 nM levels, respectively, showing a 4-fold improvement in LOD compared to direct infusion ESI-MS without DRILL (Figure 5.6b and c). For the full protein, direct infusion ESI-MS (no DRILL) detected the +23 charge state ions at 1262 m/z down to 400 nM, and DRILL does not show any improvement for detection of the full length protein (LOD of 600 nM, data not shown).

As discussed, the DRILL-MS applications lead to a shift in charge state distribution (CSD) for cytochrome-c and improvements in SNR and LOD for peptides, indicative of the ability of DRILL to enhance collection of small droplet populations. This can be used to obtain insight into the physico-chemical properties (e.g., surface affinity) of the protein fragments (8.5 kDa and 15 kDa) and the full protein, little of which are known. The 4-fold improvements in LOD via DRILL (vs ESI) for the two protein fragments suggest increased enrichment of these molecules in small droplet populations. On the other hand, the full CA protein that exhibits reduced sensitivity with DRILL (vs ESI) is likely to reside within large primary droplet populations. One of the analyte characteristics that determines its distributions within and partitioning to an electrospray droplet is the surface affinity [18]. A species with greater surface affinity has greater tendency to partition to small offspring droplets during the fission event which occurs on the surface of a primary droplet. In contrast, a hydrophilic species in the interior of the large droplet has less likelihood of migrating to small droplet populations. From the linkage between analyte partitioning behaviors dependent on the surface affinity and the ability of DRILL to preferentially

transmit of small droplet populations, one can gain the increased understanding of analyte physico-chemical characteristics.

The ESI-MS analytical results using Gen 1 DRILL clearly support the ability of a vortical flow to separate small, highly charged droplets from large, less charged droplets, enabling sampling of smaller droplets with less solvent but more surface active compounds into the mass spectrometer with reduced introduction of solvent ions and contaminants. As a result, up to ten-fold higher signal-to-noise ratios and limit of detection for small peptides and protein fragments can be achieved. Improved detection of proteins with low surface affinity which prefer to reside in large droplets may require an optimization of the residence time of droplets in the DRILL device or use of additional means (e.g., heating) to promote faster desolvation and therefore size reduction of the primary electrospray droplets..

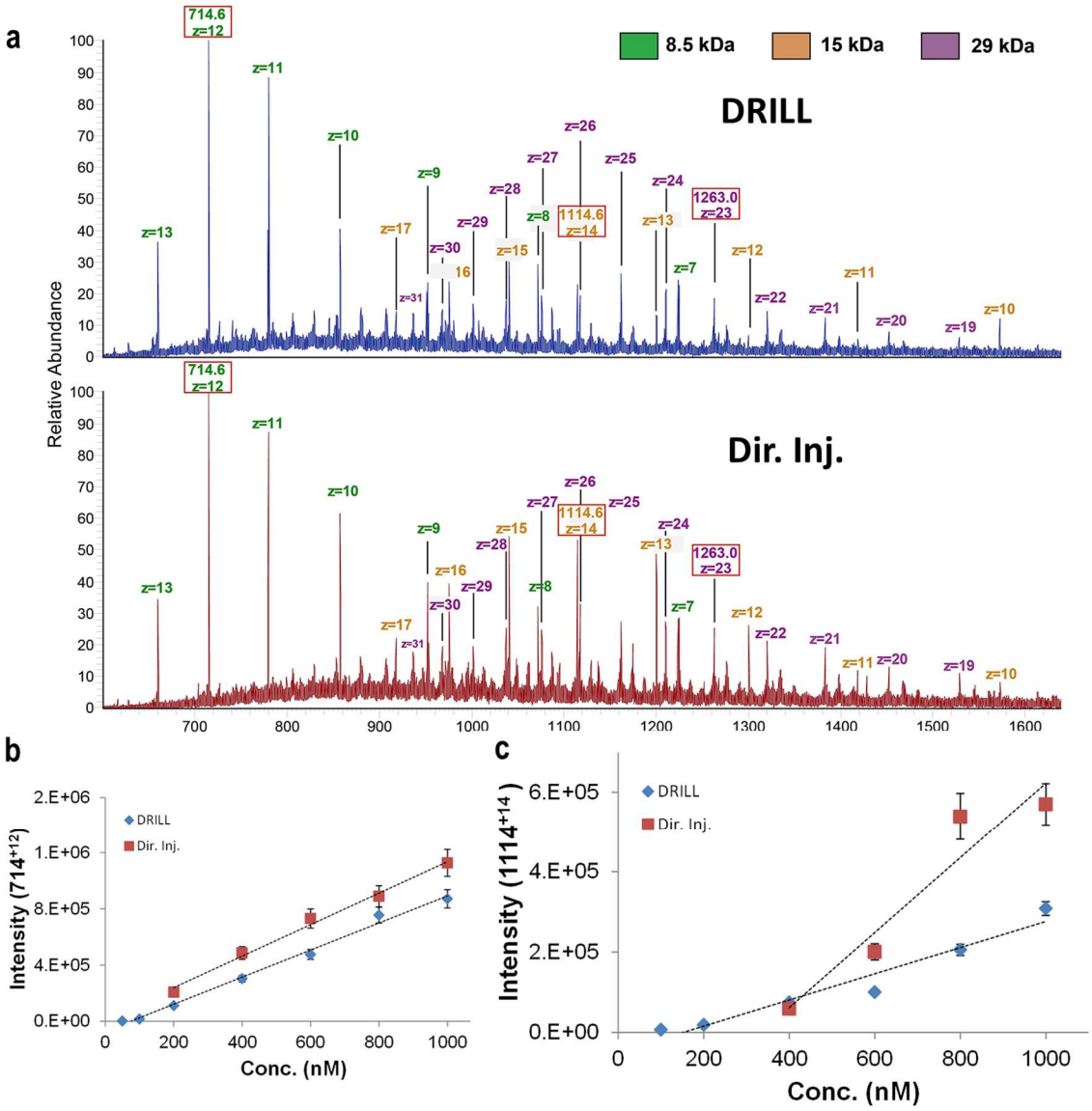


**Figure 5.6. (a) MS spectra for carbonic anhydrase for Gen 1 DRILL vs direct infusion. LOD study using DRILL and direct infusion for carbonic anhydrase fragment peaks at (b) $714^{+12}$ m/z and (c) $1114^{+14}$ m/z. Data obtained in collaboration with the Torres group at Georgia Tech; Data analysis was performed by Alex Jonke [84].**

## 5.2 Hydrophobic Biased Mass Spectra via DRILL

The hydrophobicity (or surface activity) of analyte molecules is closely related to detection efficiency in mass spectrometry as the analyte partitioning (surface vs bulk) within electrosprayed droplets depends on the hydrophobicity. In the discussion below,

droplets are assumed to have significant water content. The same points apply for other solvents with the words “hydrophobic” and “hydrophilic” replaced by “solvophobic” and “solvophilic.” Mass spectra allow differentiation of infusion methods by comparing the hydrophobic bias which is determined based on the relative abundance of different species with varying hydrophobicity. A mass spectrum showing a hydrophobic vs hydrophilic bias provides information on the relative size (small vs large) of droplet populations from which these ions are derived. Fenn has shown that in electrosprayed droplets, more hydrophilic molecules will be in higher concentration in the droplet interior (bulk). On the other hand, hydrophobic analytes are distributed near the droplet surface, which is enriched with excess charge [10]. Higher surface activity of hydrophobic molecules results in more efficient ionization and desorption of these molecules. As a result, hydrophobic molecules are more likely to be observed in a mass spectrum as compared to hydrophilic molecules [92]. During a droplet fission event, small offspring droplets eject from the elongated tail of the primary droplet, carrying surface charge and hydrophobic analytes concentrated on the surface of the primary droplet. Therefore, small offspring droplets are rich in hydrophobic analytes and have a surface with higher charge density compared to large primary droplets.

Here, the MS results using a mixture of analytes (peptides/fluorinated polymers) with varying hydrophobicity are presented to characterize droplet segregation in vortical gas flow and assess the impact on the analyte spectral signature. Overall, the results support the conclusion that DRILL gives a hydrophobic bias to mass spectrometric analysis, which is due to preferential capture and transmission of smaller droplets into MS.

#### 5.2.1.1 Fluorinated Polymer Mixture with Varying Nonpolar Surface Area)

Previous reports suggest non-polar surface area (NPSA) of analyte molecules can be used as a metric of hydrophobicity or relative affinity of analyte towards the droplet surface [92-96]. To investigate the effects of different infusion methods (DRILL-ESI vs direct infusion ESI) on the MS signal response, a mixture of fluorinated polymers, Ultramark 1621, with varying nonpolar surface area is analyzed using both methods, and the resulting MS responses are compared in the context of analyte hydrophobicity. Ultramark 1621 is a commercially available calibration mixture consisting of fluorinated phosphazines and protonated phosphazines with a mass spectrum featuring a series of peaks ranging from 922 m/z to 1922 m/z. The NPSA of a phosphazine molecule is determined using Van der Waals radii, bond lengths, and the basic geometry; and the resulting NPSA increases from 424 $Å^2$ to 1272 $Å^2$ with increasing molecular weight. DRILL's ability to preferentially transfer smaller droplets along suggests that Ultramark 1621 mass spectra acquired with use of DRILL should show a hydrophobic bias, represented by a shift to a higher abundance weighted average molecular weight, $M_{avg}$, (due to larger molecules having a larger NPSA), calculated using,

$$M_{avg} = \frac{\sum_{n=1}^{11} \left( Ab_n \times m_n \right)}{\sum_{n=1}^{11} Ab_n} \tag{5.1}$$

where $Ab_n$ is the ion abundance and $m_n$ the mass corresponding to the n-th peak of Ultramark 1621.

In Figure 5.7, the relative abundance of Ultramark 1621 infused at a volumetric flowrate, $\dot{V}$, of 1000 nL/min via standard (no DRILL) direct infusion ESI, Gen 1 DRILL,

and Gen 2 DRILL are compared on a triple quadrupole mass spectrometer. The work presented in Figure 5.7 is entirely contributed by Crystal Pace in W.M. Keck Fourier Transform Mass Spectrometry Laboratory of North Carolina State University. With DRILL and without DRILL, the maximum peak occurs at 1322 m/z. However, higher peak abundance is observed with DRILL in the direction of increasing NPSA and hence, preference toward more hydrophobic species in the MS spectra. Based on 251 mass spectra acquired via direct infusion ESI (no DRILL) and with Gen 1 DRILL, the average mass for the latter (1383.16 $\pm$ 0.27 Daltons) is distinctly higher the former (1372.81 $\pm$ 0.11 Daltons), indicative of a more hydrophobic bias imparted to mass spectrometric detection by using Gen 1 DRILL. The initial diameter of the primary droplet using the Ultramark 1621 solution is estimated to be about 1.6 $\mu$m, and the size is within the range in which the swirl-induced droplet separation effects can be exploited given enough vortex strength. On the other hand, the mass spectra obtained using Gen 2 DRILL does not indicate any evidence of droplet separation or selective capture of small droplets with the average mass (1370.86 $\pm$ 0.40 Daltons) slightly lower than that via direct infusion (no DRILL) ESI. While no measurement of the flow rate is made in this specific condition, the low weighted average mass with Gen 2 DRILL appears to be related to low vorticity in Gen 2 DRILL due to lack of vortex convergence/ retention mechanism (no front tube, ~1 cm swirler-MS inlet separation distance), suggesting that sufficiently high vorticity is required to cause pronounced droplet separation effects on mass spectra. These conclusions in agreement with results of simulations (Chapter 2, Figure 2.10) show the important of the swirl strength on separation efficiency of vortical flow.

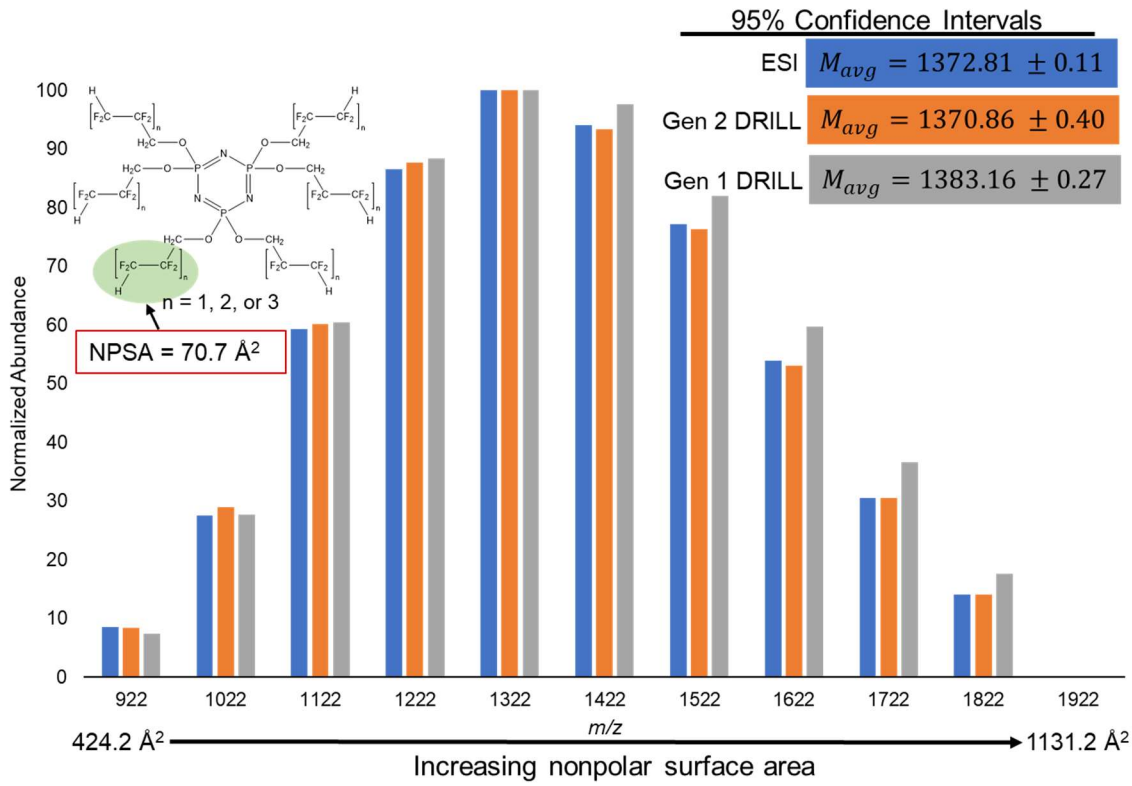


**Figure 5.7. Comparison of averaged spectra of Ultramark 1621 between Direct Infusion (no DRILL) ESI, Gen 1 DRILL, and Gen 2 DRILL. A total of 251 spectra is acquired and averaged for each analysis method. Data displayed in Figure 5.7 have been obtained by the Muddiman group at NCSU using Gen 1 and 2 DRILL device.**

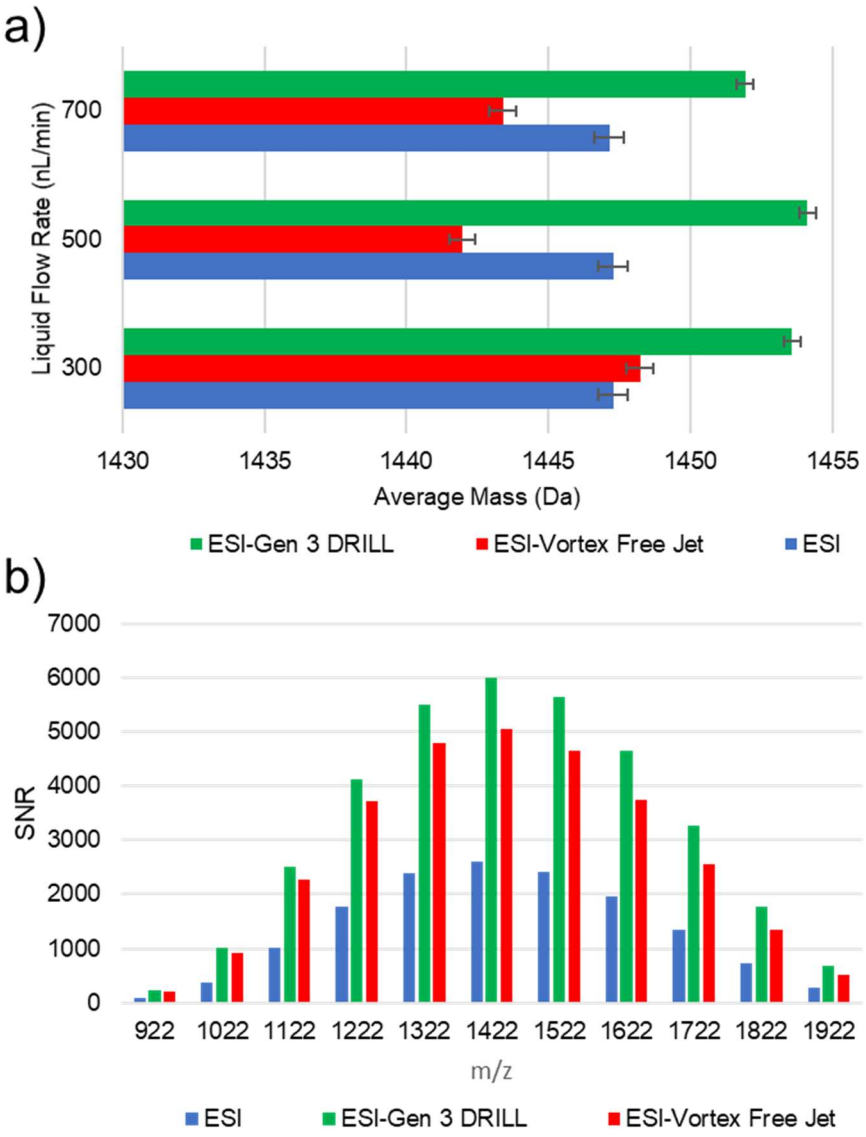


**Figure 5.8. Comparison between Direct Infusion (no DRILL) ESI, ESI-Gen 3 DRILL, and ESI-Vortex free jet. (a) The abundance weighted average mass of Ultramark 1621. The results reflect the average of 100 mass spectra for each method. (b) Signal-to-noise ratio (SNR) corresponding to each analysis method.**

Ultramark 1621 is infused via Gen 3 DRILL coupled to an LTQ orbitrap mass spectrometer varying sample flow rate. The flow rate of the vortical flow in DRILL is taken at 1.3 L/min for maximum vorticity (swirl strength) but not to exceed the MS suction rate to ensure optimal gas flow coupling. In Figure 5.8a, the abundance weighted average mass

for Gen 3 DRILL-ESI-MS (green) is compared to that acquired via direct infusion (no gas assist) ESI (blue) and ESI coupled with a vortex-free gas jet at the same flow rate of 1.3 L/min (red). The abundance weighted average molecular weight in the Ultramark 1621 spectra obtained using Gen 3 DRILL is the highest of all values obtained across the different methods, with $M_{avg}$ 7 Da greater than that obtained with direct infusion (no gas assist) ESI, demonstrating a hydrophobic bias in detection. The differences between $M_{avg}$ obtained with Gen 3 DRILL and vortex-free jet assisted ESI are even greater at liquid infusion flow rates of 500 nL/min and 700 nL/min, which yield larger size primary droplets. As indicated in Figure 2.10 (Chapter 2), the vortex free jet has no ability to separate droplets based on the droplet size but allows increased amounts of both small and large droplets to enter the MS inlet by focusing the electrospray plume. Large primary droplets tend to contain more hydrophilic molecules, so increased intake of larger droplets may result in detection of more hydrophilic ions leading to a shift in the abundance weighted average Ultramark 1621 mass to a lower value. Figure 5.8b displays signal-to-noise ratios (SNR) of all methods. Across the entire m/z range, DRILL displays the highest SNR which is the spectral enhancement associated with efficient droplet desolvation. The SNR from the vortex-free jet assisted ESI is higher compared to direct infusion (no gas assist) ESI, presumably attributable to the use of an impinging high purity gas jet which helps to repel neutrals and other potential contaminants from the sampling orifice.

Simulations discussed in Chapter 2 indicate that the vortex-induced separation effects diminish as the droplet diameter increases above 5 $\mu$m. For validation, Ultramark 1621 is infused via Gen 3 DRILL at increased sample flow rates ranging between 5 $\mu$L/min and 20 $\mu$L/min that are expected to produce larger primary droplets. The resulting average

mass is compared to that acquired using a commercial heated ESI (HESI) source and vortex-free jet assisted ESI. In Figure 5.9, DRILL demonstrates the most hydrophobic bias of all, indicative of efficient droplet separation/soring for the droplet size populations generated using electrospray flow rate $\dot{V}$ =5 $\mu$L/min. Given that the estimated primary droplet size is 2-3 $\mu$m in diameter at this flow rate, the vortex-induced outward inertia appears to be effectively removing large primary droplets in this size range. As the sample flow rate increases to 10 $\mu$L/min, the greatest hydrophobic bias appears with the HESI source. In the HESI source, the sample capillary is heated to a high temperature (275℃ in this experiment) for enhanced thermal desolvation, and electrospray is accompanied by a high-pressure coaxial gas jet with auxiliary gas flow for improved nebulization and additional desolvation. HESI allows rapid evaporation of large primary droplets generated by high flow rates (10 $\mu$L/min and 20 $\mu$L/min) leading to efficient desorption of hydrophobic ions despite the initial droplet diameter being ~4 $\mu$m and greater. As a result, the abundance of hydrophobic ions appears less affected by increase in the electrospray flow rate, as indicated by less variationsin the abundance weighted average Ultramark 1621 mass across the all sample flow rates tested. On the other hand, the abundance weighted average mass via DRILL decreases rapidly with increasing sample flow rate, supporting the result obtained via simulation, that the droplet separation effects can be best leveraged for the primary droplet size range between 1 $\mu$m and 5 $\mu$m. Importantly, no heating of the sample is performed in DRILL, thereby the softness of ionization should be preserved, which is an additional important dimension of ESI-MS analysis, especially of fragile complexes with non-covalent binding.

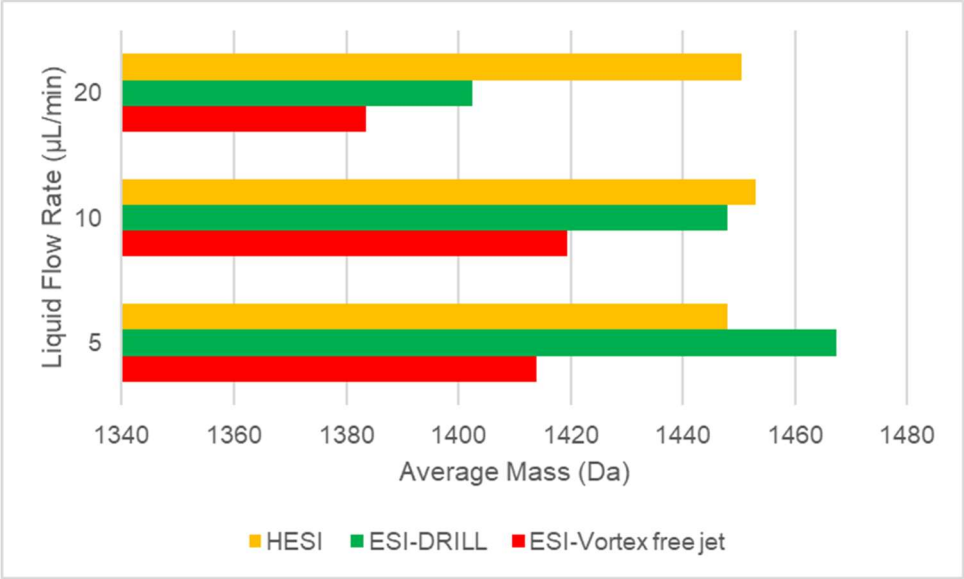


**Figure 5.9. Comparison of the average mass between commercial HESI (heated ESI source), ESI with Gen 3 DRILL, and ESI with Vortex-free jet**

5.2.1.2 Peptide Mixture with Varying NPSA

The hydrophobic bias observed in DRILL experiments with Ultramark 1621 is an indicator of the ability of DRILL to improve transmission of smaller droplets that are valuable to biochemical analysis. To observe the impact of droplet separation on detection of biomolecules, a 200 nM peptide mixture containing MRFA acetate salt (MRFA), trifluoroacetate salt (SIGSLAK), kemptide acetate salt (LRRASLG), human adrenocorticotropic hormone (MEHFRWG), angiotensin II (DRVYIHPF), and neurotensin (pE-LYENKPRRPYIL) is infused into an Orbitrap mass spectrometer via Gen 3 DRILL and a commercial nano-ESI source (Flex) with sample flow rates of 300 nL/min and 1000nL/min. The letters in the parenthesis indicate one letter code for each amino acid in a peptide sequence. As previously described [92, 95], NPSAs for the peptides are determined by summing the non-polar surface area for each amino acid [97]. A built-in protein deconvolution algorithm in the Xcalibur data processing software is used to

determine the peptide abundance by combining analyte peaks at all charge states into a single peak. Figure 5.10 compares the abundance of each peptide in the mixture between DRILL and the commercial Flex source as a function of NPSA. In Figure 5.10a, at the sample flow rate of 300 nL/min, the abundances of all peptides via Gen 3 DRILL are higher vs Flex nano-ESI except for MRFA, which is the most hydrophilic peptide with the smallest NPSA. Additionally, compared to Flex nano-ESI the DRILL-MS response displays up to ×3.5 greater slope of peptide abundance over NPSA, hence indicating an increased sensitivity to hydrophobic species.

Cech and Enke [92] demonstrated a proportional relationship between MS signal strength and analyte hydrophobicity in the relatively low NPSA region (< 300 $Å^2$). Randall et al. [93] explored the effects of analyte NPSA on the MS response more extensively covering an NPSA range between 300 $Å^2$ and 1200 $Å^2$. The studies reveal that peptides with a moderately high NPSA between 500 $Å^2$ and 700 $Å^2$ result in higher signal intensities due to better ionization compared to those outside of this NPSA zone. On the other hand, more hydrophobic peptides with increasing NPSA value (≥ 700 $Å^2$) show a decrease in abundance, presumably attributable to poor solubility in the solvent [93, 98]. This agrees well with the trend shown in Figure 5.10 (for both DRILL and Flex) that shows the peptide signal sensitivity significantly drops for the analyte with a NPSA value of 901 $Å^2$ as compares to that with an NPSA of 695 $Å^2$. Although NPSA is an important property for predicting MS response of peptides, it is not the sole determinant – in fact, there can be significant variation in abundance of peptides with similar NPSA. [93]

In Figure 5.10 (b), the peptide quantitation obtained with DRILL shows lowered abundance for some peptides at a higher sample flow rate of 1000 nL/min. Given that there may be other factors such as solution pH and analyte solubility that impact ionization and hence, detection of peptides/proteins, it may not be simple to explain some variations in relative abundance of peptides detected via ESI with DRILL vs commercial Flex nano-ESI at this flow rate. Regardless, one consistent trend observed is that the MS signal with use of DRILL is lower for the most hydrophilic peptide but higher for the most hydrophobic peptide, a clear indication of enhanced capture of small droplet populations enriched with more hydrophobic ions.

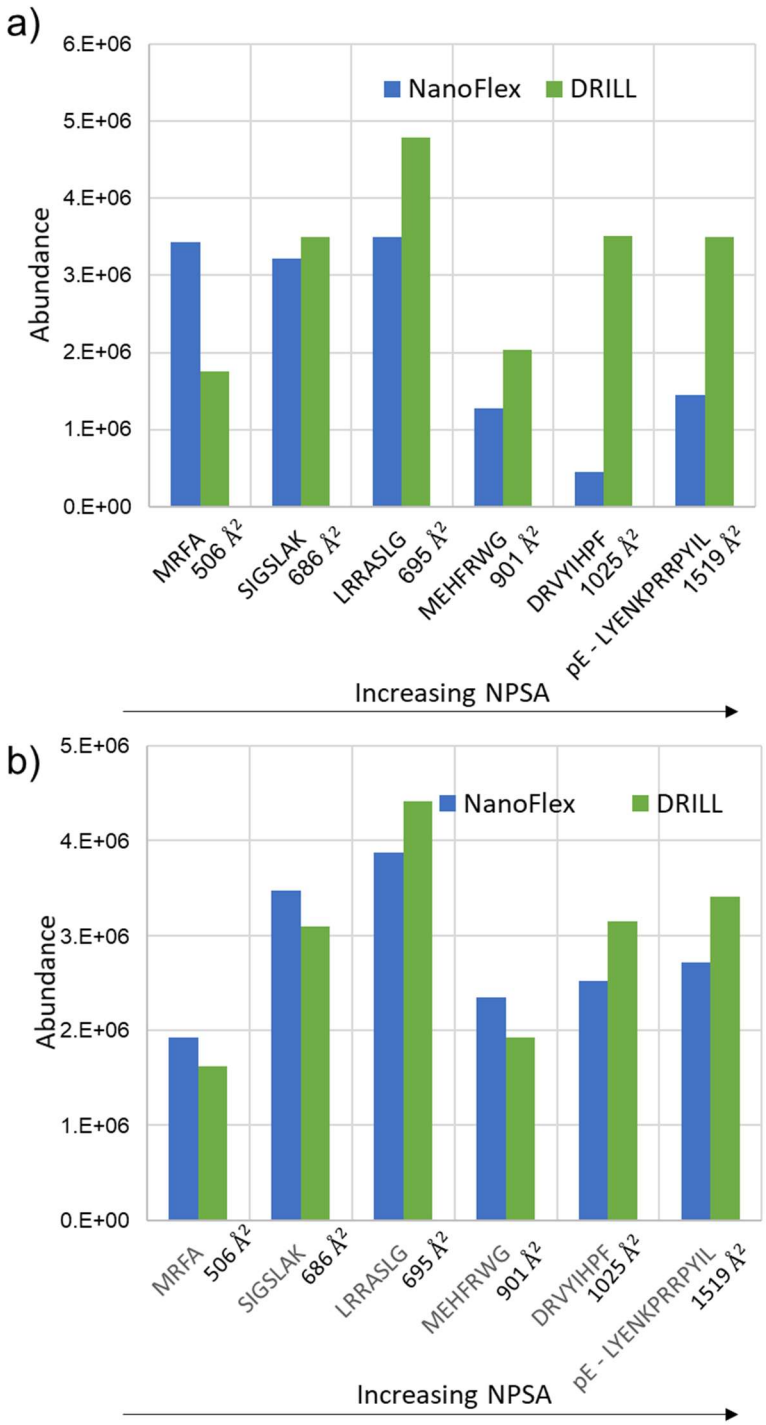


**Figure 5.10. Comparison of abundance in detected peptides with varying NPSA between Gen 3 DRILL (blue) and a commercial Flex n-ESI source (green) at sample flow rate (a) 300 nL/min and (b) 1000 nL/min. The *x*-axis indicates the amino acid sequence of peptide with NPSA in increasing order. The peptide mixture contains 200 nM of each peptide in 25:75 water:methanol (v/v), 0.1% formic acid.**

# CHAPTER 6. CONCLUSIONS

The theoretical, computational and experimental studies presented in this dissertation provide in-depth insight into several aspects of multiphase electrohydrodynamics of charged droplets in a complex flow scenario. The investigation into a flow comprised of a coupled vortical source and a sink (suction) lead to a deeper understanding of the interacting flow behavior, providing quantitative guidelines for design and operation of the novel ESI-MS interface, DRILL. The original contributions are summarized with conclusions from this dissertation work, recommendation for future studies, and potential applications beyond mass spectrometry.

## 6.1 Original Contributions

### *6.1.1 Fundamental Science*

- An electrohydrodynamic model of electrosprayed charged droplet transport is developed that incorporates the combined effects of complex gas flow and electric fields (with incorporation of space charge effects) to predict electrospray droplet interactions, trajectories, and destinations as a function of droplet size and charge in the atmospheric pressure region. The modeling methodology provides a comprehensive framework to investigate the effects of a vortical gas flow on electrospray droplet separation, transmission, and droplet size distributions in an expanding electrospray plume. The modeling and simulations are applicable to other systems that involve transport of charged particles/ions in multiphase flows, such as electrostatic precipitators, differential mobility analyzers, and other engineering devices.

- Schlieren visualization of flow behavior for free jet expansion and an aerodynamically coupled source-sink configuration was evaluated for vortex-free and vortical flow to assess the onset of turbulence and the effectiveness of hydrodynamic "coupling" as functions of the flow rate and source-to-sink distance, and also to evaluate any impact on the flow of the addition of co-axial electrospray. The flow behavior imaging was complemented by charge transmission/electric current measurements, which provide highly specific information on the effects of the flow conditions on the fates of charged droplets/ions.

*6.1.2. Engineering Innovations and Applications*

- A novel electrospray transmission device, DRILL (Dry Ion Locomotion and Localiation) was designed, optimized and implemented for size-selective inertial separation of charged droplets by vortical flow to alter electrospray droplet trajectories for improved transmission of the target electrospray droplet population.
- DRILL has been successfully applied to bioanalytical electrospray ionization mass spectrometry (ESI-MS), and enabled an improved limit of detection with greater signal-to-noise ratio.

## 6.2 Summary of Principal Findings

Multiphysics modeling and simulations revealed that the spatial size distributions of electrosprayed charged droplets and their trajectories depend strongly on the hydrodynamic conditions to which the droplets are subjected.

- In conventional electrospray without any auxiliary forced gas flow, large parent (low charge) droplets occupy the inner core, and small offspring (high charge) droplets the periphery of the plume. The radial position of the droplets is largely due to the effect of electrostatic repulsion among the droplets (space-charge effect) which accelerates the smaller more highly charged drops more effectively.
- The use of a non-swirling coaxial gas jet focuses the electrospray plume, minimizing dispersion of both large and small droplets while keeping the spatial distribution of droplets unaltered.
- The use of a vortical flow to manipulate the electrospray plume enables the droplet size distribution inversion: Large droplets are displaced to the periphery due to the vortex induced outward inertia, while small droplets are focused in a manner similar to with a non-swirling coaxial gas jet. Small droplets therefore experience less dispersion and occupy the central core region of the plume.
- This separation effect is most profound for droplets with diameters in the range of 1 $\mu$m to 5 $\mu$m (charged at 80% Rayleigh limit) and increases with increasing swirl number which is a measure of an intensity of vortical flow.
- Droplets smaller than 1 $\mu$m in diameter, especially those with diameters of a few 100s of nm, follow the gas flow streamlines very closely due to insignificance of inertia for them at relevant velocites. In a vortical flow, these small droplets (approximately corresponding to the size of offspring droplets in electrospray) display less sensitivity to outwardly directed inertia and stay close to the center of rotation while in their circular motion.

- The motion of droplets with a diameter greater than 5 $\mu$m is not strongly affected by hydrodynamic conditions. Instead, it is dominated by the droplet inertia after being accelerated by the high electric force near the emission point of the electrospray source.

Schlieren flow visualization revealed the effects of different parameters on the coupling of vortical flow and suction, helping to guide DRILL design and operation. The parameters investigated are broadly relevant to studying interacting behaviors between a jet (with and without swirling) and a suction, including the effect of the presence of co-axial electrospray introducing a charged aerosol. The flow regimes discovered in optical imaging and complemented by quantitative charge/ion current measurements at the electrospray source and the suction tube allow mapping flow conditions to charged droplet trajectories and ion current transmission.

- Onset of turbulence accompanies rapid jet growth and flow mixing which are detrimental to retention of well-structured swirling, which result in loss of droplet separation effects. The turbulence onset distance decreases with increasing gas flow rate. Swirling jets vs vortex-free jets display distinctly shorter turbulence onset distances for Re>2500 corresponding to $\dot{Q}$>1 L/min. The turbulence onset distance is measured to be 8 mm<$d_{TO}$<12 mm.
- For effective droplet separation, complete coupling of a vortical jet and suction is desirable, which depends on a few limiting parameters: the supplied flow rate, the vortical jet diameter, and the nozzle to suction distance. (1) The supplied flow rate is to match the suction rate (1.3 L/min) (2) Partial flow loss

is observed when the vortical jet grows to a diameter greater than ×3 the suction tube ID (0.6 mm), which places a limit on the separation distance between the nozzle and the suction inlet. (3) The maximum separation distance for complete coupling is shorter than the turbulence onset distance for 1000<Re<2500. For maximum swirl strength and droplet separation effects in complete coupling, the source-sink separation distance should be kept at ~6 mm.

- Ion/ charged droplet transport into the suction tube is strongly correlated with complete flow coupling. Incomplete flow coupling results in increased losses of ion currents to the periphery of the suction tube, thus lower ion current transmission efficiency into the suction tube. A flow rate greater than the suction rate leads to incomplete coupling accompanying lower ion current transmission. For example, the gas flow rate 10% greater than the suction flow rate results in 10% lower ion survival rate vs complete coupling condition. The ion current transmission efficiency suddenly drops by 20% in the incomplete coupling regime (vs complete coupling) with increased source-sink separation distance. Specific to the experimental conditions investigated, important operation parameters for optimal ion current transmission include an on-axis alignment, a flow rate match (1.3 L/min), and a source-sink separation distance equal to the maximum value (6 mm).

Case studies in DRILL ESI-MS application provide evidence of the droplet inertial separation effects via vortical flow leading to selective transmission of small offspring droplets. The characteristics of mass spectra obtained with DRILL are distinctly different from those of baseline ESI with no gas-assist flow, showing (1) less noise associated with

solvent and ambient chemical introduction to mass spectrometer, (2) improved limit-of-detection of peptides and proteins, and (3) preferentially greater sensitivity to hydrophobic analytes. Three design variations of DRILL, all exploiting the same fundamental principle of inertial droplet separation by a vortical flow, have been characterized to assessed various improvements in ion current transmission (e.g., direct coupling of the vortical flow and suction in DRILL Gen 2 vs Gen 1 design) and electrospray orientation (e.g., co-axial electrospray in Gen 3 vs Gen 2). Different metrics of ESI-MS performance have been used when assessing the different generations of DRILL due to constraints on time available for analytical experimentation; however, because the same underlying physics are embodied across applications of all DRILL designs, the conclusions listed below are deemed to be general to any electrospray transmission interfaces based on the gas-assist jet with vortical flow droplet separation.

- DRILL application for ESI-MS demonstrates up to ten-fold improvement in signal-to-noise ratio for peptides and proteins leading to proportional improvements in limit of detection.
- Direct coupling of the vortical flow in DRILL with the MS inlet reduces the charged droplet/ion losses and improves the overall ion transmission from the electrospray source to mass spectrometer.
- The electrospray, and, in turn, MS signal stability is improved by using co-axial vs. cross flow electrospray configuration, which is important for improved robustness and analytical quality of ESI-MS workflows.
- DRILL introduces a bias (increased relative sensitivity) for hydrophobic analytes as compared to standard ESI-MS. This is also apparent in a shift in the

charge state distribution of MS spectra of analytes with increased peptide non-polar surface area.

## 6.3 Recommendations for Future Research

Increasing the vertical jet swirl number: Based on flow simulations, the vortex generator used in DRILL produces a swirling jet with a moderate swirl number (S=0.35) at the maximum flow rate for which effective coupling with most analytical mass spectrometers is possible (1.3 L/min). Comparisons of the simulation results with the experimental turbulence onset distance measurements (Figure 3.5) and mass spectrometric characterization suggest that the actual tangential swirl velocity may be lower than simulated. This is attributed to strong viscous effects present in the gas domain between the no-slip annular walls close to each other (1 mm width). The gas enters the vortex flow creation domain through six tangential inlets, which results in fairly low average tangential velocity magnitude of only 1.1 m/s (Re=125). A flow with increased entry velocity gains greater momentum to overcome the viscous effects leading to improved swirl development. Figure 6.1 displays the simulated swirl number (measure of the swirl rotation strength) as function of average tangential velocity magnitude of carbon dioxide entering the tangential inlets in Gen 3 DRILL. While the flow rate is held constant at 1.3 L/min, swirl number (defined in Eq (2.16)) increases nearly linearly with increasing entering velocity of gas from 1.1 m/s to 3.5 m/s. This can be practically realized by reducing the number of tangential inlets to the flow creation domain in DRILL to increase the flow area while keeping the volumetric flow rate constant. This simple geometric modification is expected to increase the swirl number and thus increase inertial droplet separation effects.

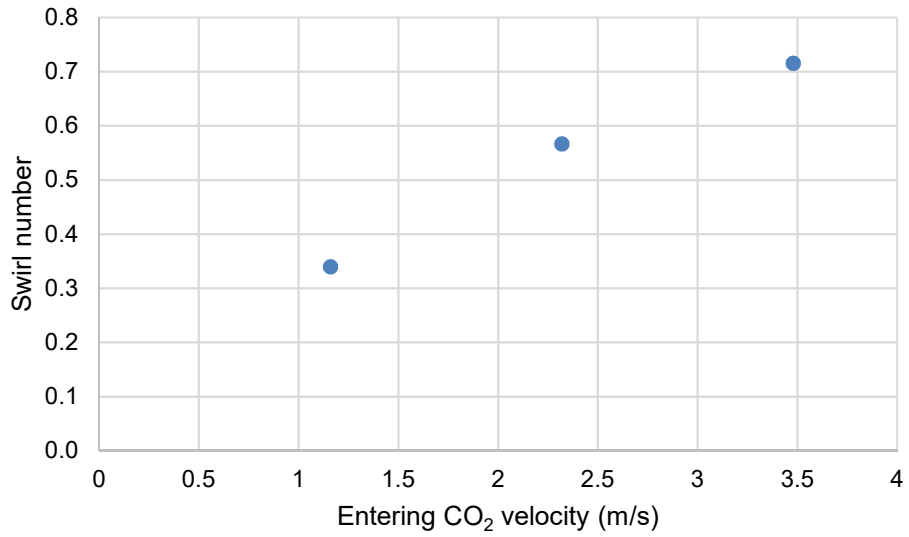


**Figure 6.1. The simulated swirl number vs velocity of $CO_2$ entering the tangential inlets. Swirl number increases with increasing entry velocity of gas (representative results for the volumetric flow rate of 1.3 L/min).**

Improved desolvation of large droplets: The inertial separation capability presented in this dissertation provides selectivity of transmission based on the droplet size: Only submicron droplets may be fully captured by the MS orifice, with major losses of large primary droplets. While this leads to mass spectral enhancements, there remains a high potential for sensitivity improvement by achieving complete desolvation of large droplets that contain significant amounts of analyte ions. Desolvation strategies may include use of heated gas or tubing with additional heating is supplied between the nozzle and the MS suction tube. Large droplets that reduce in size via desolvation may be re-entrained into the stream of small droplets due to weakened inertial effects. This is especially important for analysis of small samples where any loss of analyte, such as that in currently rejected large droplets, cannot be afforded, and is also important to remove the solvophobic bias that may hinder some analyses.

## 6.4 Applications beyond Mass Spectrometry

A vortical flow is shown to be an effective mechanism to sort/separate charged droplets/particles based on the droplet size (mass) and is relevant for phase separation (i.e. particulate matter from fluids, particles of different density) in numerous processes (e.g., filtration of air pollutant, concentration of particles from fluid-particle suspension).

Use of a vortical flow may be relevant to applications for elimination of charged contaminants from air. In an electrostatic precipitator (ESP), air containing dust and smoke flows in an array of plate electrodes that attract ionized particulates. Airborne particles are charged by corona discharge that form due to a large potential applied to the upstream side relative to the electrodes downstream. A quite large volumetric flow rate is handled by electrostatic precipitator ($<10^6$ L/s), and these devices are costly and require frequent maintenance for removal of particles accumulated on the many, closely spaced electrodes. Combination with a vortex generator designed for the large flow rate in ESPs may enable creation of flow with a high swirl number and separation of fine particles from air. The ionization may occur using a conical or point electrode for maximized corona production paired with a single cylindrical counter-electrode for particle collection. Thus a scaled up DRILL device may be exploited as an alternative to ESPs for efficient particle separation and collection.

A vortical flow in differential mobility analyzer applications can be useful to enhance the device resolution. A differential mobility analyzer (DMA) is a device used to classify and measure charged particles based on their electrical mobility, which is the ratio of the particle velocity to the electrical field intensity that causes the particle motion. The device

useful in various applications from atmospheric research to material synthesis [99] is another example of exploiting electrohydrodynamics. A typical device consists of two concentric cylindrical electrodes and a path for gas between the anulus. Charged aerosol is advected into the electric field between the two electrodes and the particles are collected based on their different electrical mobility in the flow and electric fields. The existing DMAs employ an axial gas flow and particle separation occurs by varying the electrical field only. A vortical flow in DMA devices allows enhanced manipulation and differentiation of charged particle trajectories, potentially increasing the resolution of size separation.

The utility of a vortical flow was demonstrated in ion soft landing (ISL) applications [100], which is a process in which ions of interest are concentrated into a beam to be deposited as functional thin film coatings. This ion deposition technique is applicable to a variety of practical uses, including material synthesis for batteries [101] to selective deposition of bioparticles from complex protein assemblies [102]. In ISL, sorting/separation of ions occurs based on their mass-to-charge ratio just as in MS analysis. The typical instrumentation required for soft landing of ions consists of an ionization source, ion optics for guiding ion trajectories, a mass filter for separation and selection of ions of interest, and a surface onto which ions are deposited. The processes beyond ionization take place in vacuum due to use of ion optics and the mass filter. Instead, DRILL has been applied to ISL to allow for production and desolvation of polyoxometalates (POM) ions under ambient conditions. As a result, sufficiently desolvated ions could be directly deposited onto carbon nanotube (CNT) electrodes [100] (for production of a supercapacitor [101]) without the use of a mass filter in the conventional setup, which

makes the technology much cheaper, simpler and broadly accessible. Imaging the ISL deposition obtained with assistance of DRILL revealed no residual solvent with the molecular coating film, indicative of efficient desolvation due to the combined effects of vortical flow removal of solvent enriched large droplets and solvent evaporation from the remaining small droplet in the heated swirling gas flow. The comparable energy storage performance of the supercapacitors that contain the CNT electrodes with POM deposition via DRILL and in vacuum suggests this DRILL application as a broadly accessible soft-landing method.

# APPENDIX A. SCHLIEREN IMAGE POSTPROCESSING

This appendix illustrates the post-processing procedure for schlieren images and the effects on enhancements in visibility of flow features captured by schlieren visualization. For bulk-processing of the schlieren images, macro-coded scripts written by Joel Chapman in the Fedorov group were used. The post-processing procedure is implemented in the following order: (1) Four background images taken prior to flow injection are averaged. (2) Schlieren images of flow are converted into TIFF format. (3) The averaged background image is subtracted from the flow images. (4) Three consecutively captured flow images are merged into an RGB image with red/green/blue spectral components.

## A.1 Background Averaging

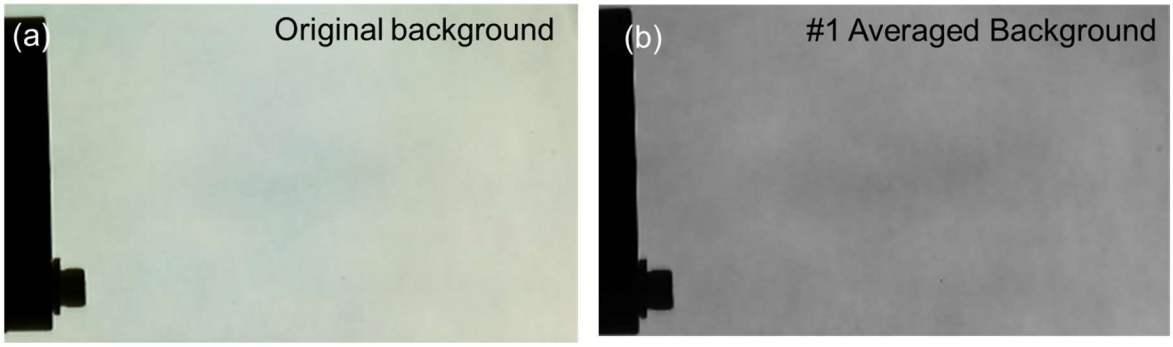


**Figure A.1 (a) Original background image captured before flow injection (b) Averaged background image is produced by combining four images**

## A.2 Conversion of Flow Images into TIFF format

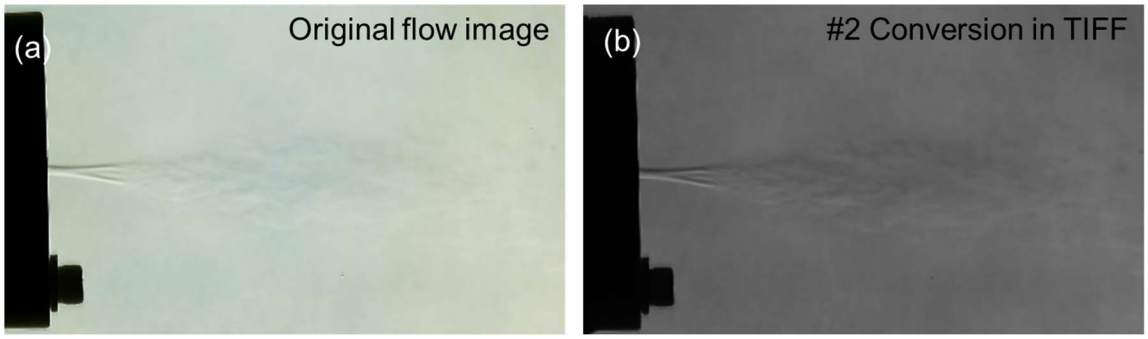


**Figure A.2 (a) Original flow image (b) Flow image in TIFF format**

## A.3 Subtraction of Background Image and Merged Flow Image

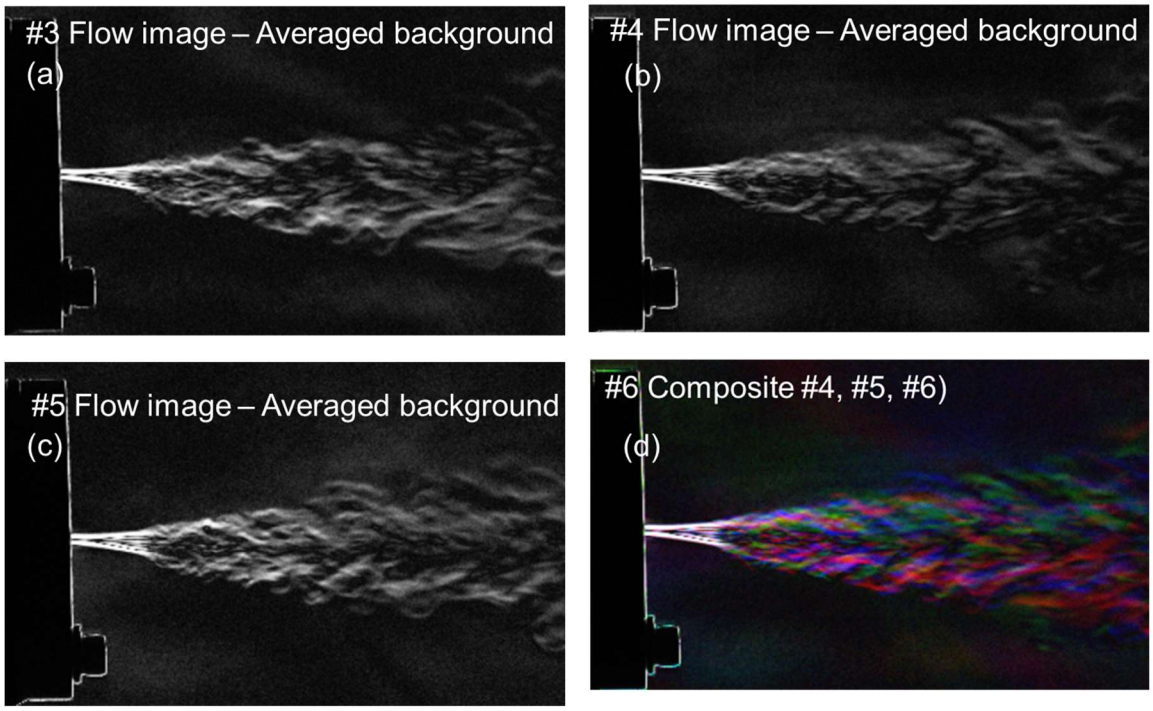


**Figure A.3 (a), (b), and (c) Images capturing differences between flow images and the averaged background image (d) Combined image of a – c with red/green/blue spectral components**

# APPENDIX B. FLOW SLICE IMAGES VIA LASER SCATTERING METHOD

To visualize the swirling flow pattern generated by Gen 3 DRILL, a fine liquid aerosol was introduced into the flow through coaxial electrospray. A fused silica capillary with conductive coating at the tip was positioned flush with the DRILL nozzle and a high voltage between 2.5kV and 3kV was applied to the needle to create an electrical potential difference from the DRILL counter-electrode or a cross shaped electrode in front of the needle which was biased with 500V or grounded. A solution series of varying MeOH and acetic acid concentrations was used to generate small sized tracer droplets. Bone dry grade carbon dioxide was supplied for DRILL. A mass flow meter downstream of the flow regulator was used to measure the flow rate entering the device and achieve the desired flow rate. The flow rate varied from 0 to 1.56 L/min. Three laser pointers were used to create green laser beams (523nm, 5mW) that intersect between 3 to 5mm downstream of the nozzle to avoid light reflecting off the reflective DRILL surface. The laser beams shined vertically, horizontally and diagonally intended to intensify the light at the intersected area. A Keyence microscope (VHX-500, IL, USA) was placed facing the DRILL device and × 100 magnified droplet streak images were taken. Images were processed using ImageJ built-in capabilities to enhance brightness and contract.

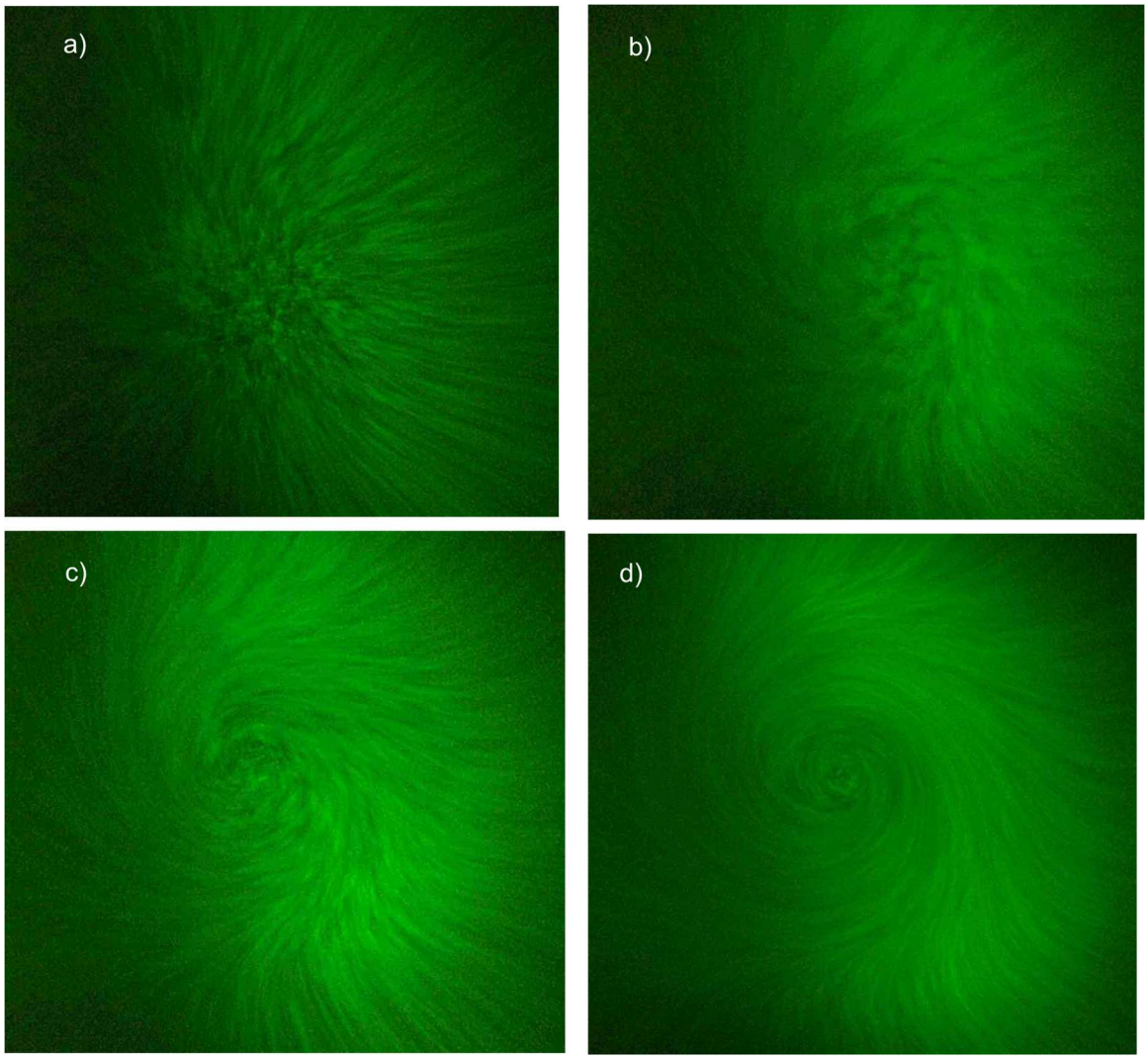


**Figure B.1 Slice images of flow 3–5 mm downstream of the Gen 3 DRILL nozzle exit. Droplet streak images with X100 magnification using a Keyence microscope (VHX-500) facing the DRILL nozzle directly. The measured flow rates were: (a) 0.65 L min$^{-1}$, (b) 0.91 L min$^{-1}$, (c) 1.17 L min$^{-1}$, and (d) 1.3L min$^{-1}$**

As shown in Figure B.1, this flow visualization technique was sufficient to illustrate the swirling motion of the flow generated by the DRILL device. Three green laser beams were combined to achieve the light intense enough to capture pathlines of the droplets and additional image processing was needed to accomplish the image quality shown. No curved motion was observed for $\dot{Q} = 0.65$ L/min and below but the weak swirling motion of

droplets appeared for the flow rate $\dot{Q}$ =0.91 L/min. The swirling motion is clearly visible for $\dot{Q}$ >1.17 L/min.

# APPENDIX C. ELECTROSTATIC SIMULATIONS IN GEN 1 DRILL

This appendix presents the numerical procedure used to find the numerical solution for the intensity of the electrical field at the ESI tip due to a combination of electrical potentials applied to the three electrodes adjacent to the tip (three non-homogeneous boundary conditions). The entire electrostatic modeling and simulations were contributed by Dr. Peter Kottke using ANSYS Fluent with a user-defined scalar for the electrical potential and custom-written user defined functions to solve the governing equation. This appendix introduces the same electrostatic simulation approach/ procedure but those performed in COMSOL for demonstration purposes. Figure C.1 displays the simulation domain of used to find the electric field strength at the ESI tip.

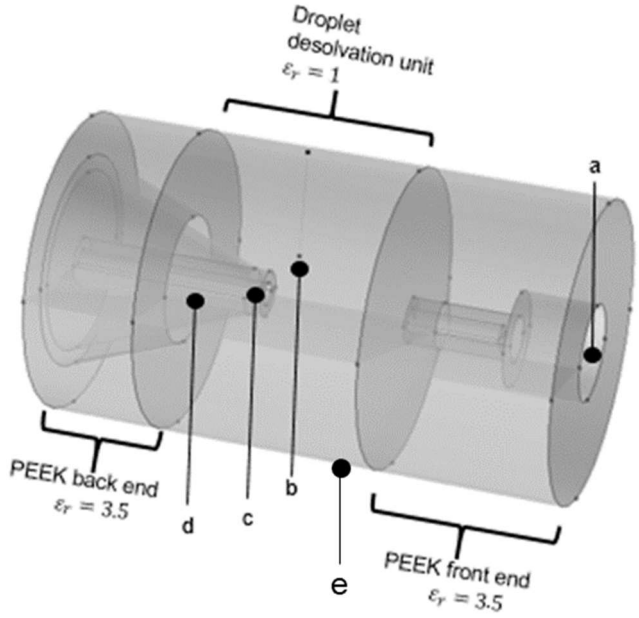


**Figure C.1 Electrostatic model of Gen 1 DRILL: (a) front electrode, (b) ESI emitter, (c) back electrode, (d) swirl cone, and (e) shell electrode.**

The goal of this simulation is to express the electric field intensity at the emitter as a linear combination of potential differences of the counter-electrodes relative to the voltage applied the ESI emitter expressed as,

$$\vec{E}_{ESI} = C_1\left(V_{shell} - V_{spray}\right) + C_2\left(V_{front} - V_{spray}\right) + C_3\left(V_{back} - V_{spray}\right)$$

where $\vec{E}_{ESI}$ is the electrical field strength, $V_{shell}$ is the voltage applied to the shell electrode, $V_{front}$ is the voltage applied to the front electrode, $V_{back}$ is the voltage applied to the back electrode, and $V_{spray}$ is the voltage applied to the ESI tip. The coefficients $C_1$, $C_2$, and $C_3$ represent the contribution of the electrical potential difference between each electrode and the spray voltage to the field intensity at the ESI tip, which are determined by implementing three simulations for any given geometry. The advantage of using this linear relationship is that one can determine the electric field strength at the ESI tip given a geometric configuration without implementing simulations for different combinations of electrical potentials applied to the four electrodes.

To determine the coefficients $C_1$, $C_2$, and $C_3$, the electrical potential field is solved using the Laplace equation without considering space charge effect.

$$\nabla\varepsilon_j\nabla\phi = 0$$

where $\phi$ is the electric potential at any location in the domain, and $\varepsilon_j$ is the relative electric permittivity (unity for air, and 3.5 for PEEK).

Let us define three normalized scalars representing the electrical potentials $\psi$, $\theta$, and $\xi$ that satisfy the Laplace equation, i.e. $\nabla\varepsilon_j\nabla\psi = 0$, $\nabla\varepsilon_j\nabla\theta = 0$ and $\nabla\varepsilon_j\nabla\xi = 0$ with

homogeneous Dirchlet boundary conditions except for ψ=1 on the outer-shell electrode (Figure C.1 #e), θ=1 on the front electrode (Figure C.1 #a), and ξ=1 (Figure C.1 #c) on the back electrode walls. Each scalar $\psi$, θ, and ξ is used to determine the contribution of the voltage applied to the associated electrode to the electrical potential field. For example, $\psi$ represents the spatial electrical potential distribution when only the outer-shell electrode is biased with an electrical potential of 1 Volt with the rest of electrodes grounded. The same applies to θ and ξ so that the effects of the electrical potential applied to different electrodes can be decoupled. Once the solutions for $\psi$, θ, and ξ are found, the electrical potential at any location in the interior of Gen 1 DRILL, $\phi$, can be expressed as,

$$\phi - V_{spray} = (V_{shell} - V_{spray})\psi + (V_{front} - V_{spray})\theta + (V_{back} - V_{spray})\xi$$

Figure C.2 to Figure C.4 display the potential fields of $\psi$, θ, and ξ decoupled from another. The superposition of the solutions for $\psi$, θ, and ξ allows one to determine the average electric field intensity at the ESI emitter $\vec{E}_{ESI}$ for a given geometry and combination of electrical potentials. The $\partial\psi/\partial n$, $\partial\theta/\partial n$, and $\partial\xi/\partial n$ are the potential gradient normal to the ESI tip area.

$$\vec{E} = \frac{1}{A_{tip}} \int \left[ (V_{shell} - V_{spray}) \frac{\partial \psi}{\partial n} + (V_{front} - V_{spray}) \frac{\partial \theta}{\partial n} + (V_{back} - V_{spray}) \frac{\partial \xi}{\partial n} \right] dA_{tip}$$

This leads to the coefficients $C_1 = \frac{1}{A_{tip}} \int \frac{\partial \psi}{\partial n} dA_{tip}$, $C_2 = \frac{1}{A_{tip}} \int \frac{\partial \theta}{\partial n} dA_{tip}$, and $C_3 = \frac{1}{A_{tip}} \int \frac{\partial \xi}{\partial n} dA_{tip}$.

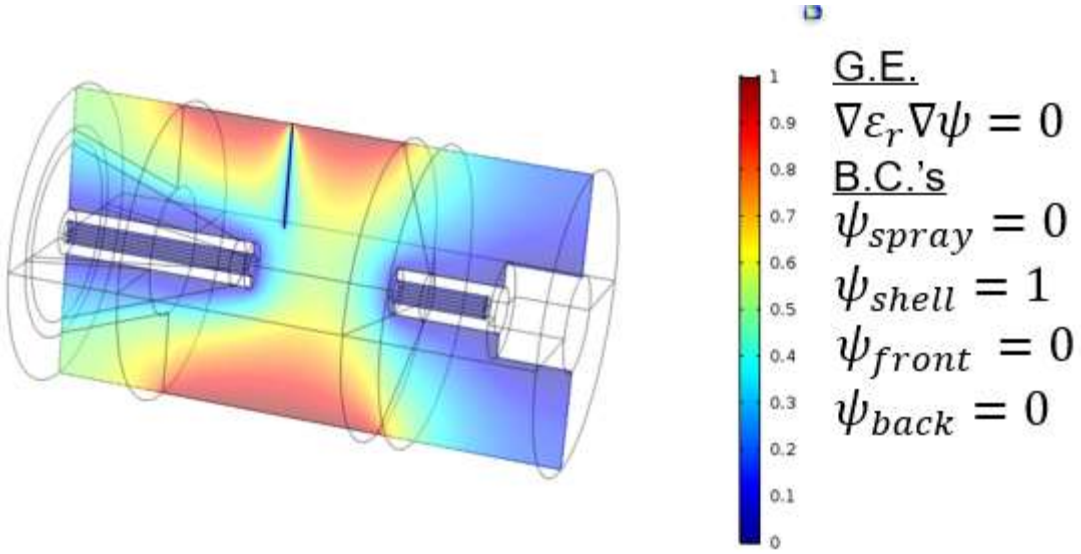


**Figure C.2 Normalized electrical potential field ψ and zero boundary conditions on the spray, front, and back electrodes**

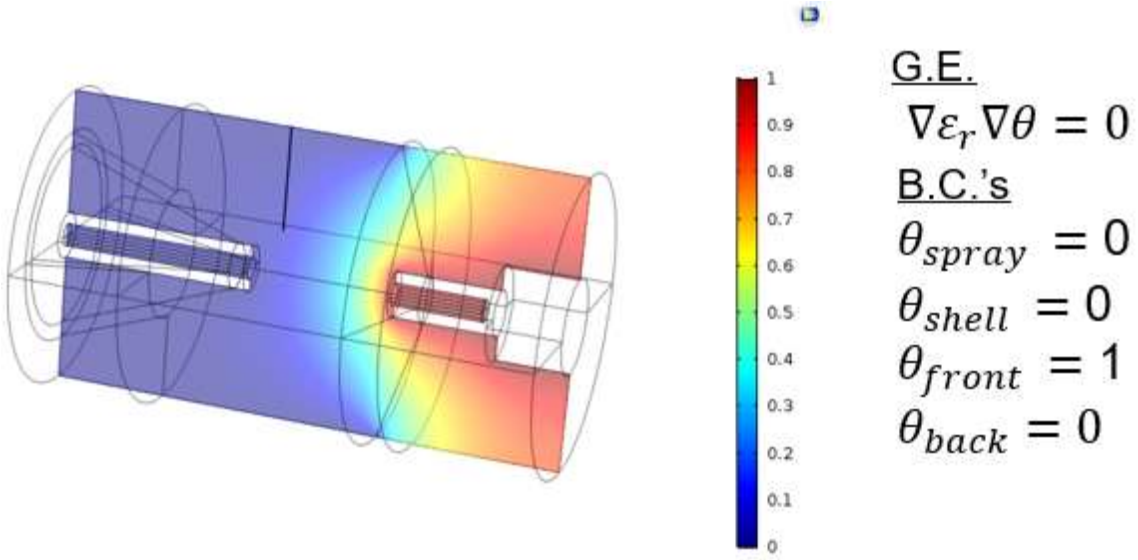


**Figure C.3 Normalized electrical potential field θ and zero boundary conditions on the spray, outershell, and back electrodes**

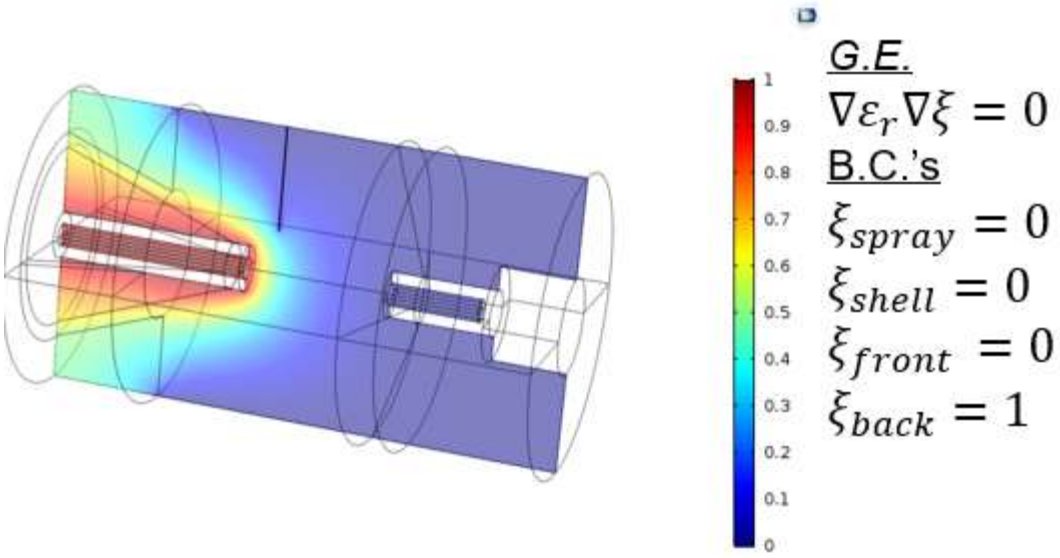


**Figure C.4 Normalized electrical potential field ξ and zero boundary conditions on the spray, outershell, and front electrodes**

.

# APPENDIX D. UNCERTAINTY QUANTIFICATION

This appendix provides uncertainties associated with experimental measurements.

In Figure 2.18, the horizontal error bar represents the estimated droplet size range assuming 50% to 100% of the Rayleigh limit computed according to Eq (2.19). The upper and lower bounds of the vertical error bar indicate the maximum and minimum of three measurements, respectively. All electrospray current readings were recorded in nA with accuracy of $\pm$ 0.5nA.

In Figure 5.7, the abundance weighted average mass is calculated according to Eq (5.1). 251 mass spectra acquired via direct infusion ESI (no DRILL) and with Gen 1 DRILL respectively are used to compute the abundance weighted average mass and the 95% confidence interval are calculated using 251 mass spectra, respectively.

In Figure 5.8. Comparison between Direct Infusion (no DRILL) ESI, ESI-Gen 3 DRILL, and ESI-Vortex free jet. (a) The abundance weighted average mass of Ultramark 1621. The results reflect the average of 100 mass spectra for each method. (b) Signal-to-noise ratio (SNR) corresponding to each analysis method. the error bar indicates the 95% confidence interval based on 113 mass spectra acquired via direct infusion (no DRILL) ESI, ESI-Gen 3 DRILL, and ESI-Vortex free jet, respectively.

A KD Scientific syringe pump (model KDS 100; Holliston, MA, USA) is used to infuse solutions for electrospray with accuracy $\pm$ 1% of the reading.

A GFM flow meter (1 L/min to 15L/min flow range, Aalborg, NJ, USA) measures the flow rate with a resolution of 0.1 L/min. The accuracy of the meter is $\pm$ 1% of the full scale, which corresponds to $\pm$ 1.5 L/min.

# REFERENCES


1. Ferries, S., et al., *Evaluation of parameters for confident phosphorylation site localization using an orbitrap fusion tribrid mass spectrometer.* Journal of proteome research, 2017. **16**(9): p. 3448-3459.

2. Sans, M., et al., *Performance of the MasSpec Pen for rapid diagnosis of ovarian cancer.* Clinical chemistry, 2019. **65**(5): p. 674-683.

3. Richardson, S.D., *Environmental mass spectrometry: emerging contaminants and current issues.* Analytical chemistry, 2008. **80**(12): p. 4373-4402.

4. Smith, D.L. and C.J. Kaeser Tran, *Mass Spectrometry Applications in Forensic Science.* Encyclopedia of Analytical Chemistry: Applications, Theory and Instrumentation, 2006: p. 1-28.

5. Dole, M., et al., *Molecular beams of macroions.* The Journal of Chemical Physics, 1968. **49**(5): p. 2240-2249.

6. Yamashita, M. and J.B. Fenn, *Electrospray ion source. Another variation on the free-jet theme.* The Journal of Physical Chemistry, 1984. **88**(20): p. 4451-4459.

7. Taylor, G.I., *Disintegration of water drops in an electric field.* Proceedings of the Royal Society of London. Series A. Mathematical and Physical Sciences, 1964. **280**(1382): p. 383-397.

8. Pfeifer, R.J. and C. Hendricks Jr, *Parametric studies of electrohydrodynamic spraying.* Aiaa Journal, 1968. **6**(3): p. 496-502.

9. De La Mora, J.F. and I.G. Loscertales, *The current emitted by highly conducting Taylor cones.* Journal of Fluid Mechanics, 1994. **260**: p. 155-184.

10. Fenn, J.B., *Ion formation from charged droplets: roles of geometry, energy, and time.* Journal of the American Society for Mass Spectrometry, 1993. **4**(7): p. 524-535.

11. Gomez, A. and K. Tang, *Charge and fission of droplets in electrostatic sprays.* Physics of Fluids, 1994. **6**(1): p. 404-414.

12. Rayleigh, L., *XX. On the equilibrium of liquid conducting masses charged with electricity.* The London, Edinburgh, and Dublin Philosophical Magazine and Journal of Science, 1882. **14**(87): p. 184-186.

13. Zhan, D., J. Rose, and J.B. Fenn, *Solvation studies of electrospray ions—method and early results.* Journal of the American Society for Mass Spectrometry, 1998. **9**(12): p. 1241-1247.

14. Iribarne, J. and B. Thomson, *On the evaporation of small ions from charged droplets.* The Journal of Chemical Physics, 1976. **64**(6): p. 2287-2294.

15. Thomson, B. and J. Iribarne, *Field induced ion evaporation from liquid surfaces at atmospheric pressure.* The Journal of Chemical Physics, 1979. **71**(11): p. 4451-4463.

16. Kebarle, P. and U.H. Verkerk, *Electrospray: from ions in solution to ions in the gas phase, what we know now.* Mass spectrometry reviews, 2009. **28**(6): p. 898-917.

17. Iavarone, A.T. and E.R. Williams, *Mechanism of charging and supercharging molecules in electrospray ionization.* Journal of the American Chemical Society, 2003. **125**(8): p. 2319-2327.

18. Wilm, M., *Principles of electrospray ionization.* Molecular & cellular proteomics, 2011. **10**(7).

19. Felitsyn, N., M. Peschke, and P. Kebarle, *Origin and number of charges observed on multiply-protonated native proteins produced by ESI.* International Journal of Mass Spectrometry, 2002. **219**(1): p. 39-62.

20. Kebarle, P. and L. Tang, *From ions in solution to ions in the gas phase-the mechanism of electrospray mass spectrometry.* Analytical chemistry, 1993. **65**(22): p. 972A-986A.

21. Juraschek, R., T. Dülcks, and M. Karas, *Nanoelectrospray—more than just a minimized-flow electrospray ionization source.* Journal of the American Society for Mass Spectrometry, 1999. **10**(4): p. 300-308.

22. Page, J.S., et al., *Ionization and transmission efficiency in an electrospray ionization—mass spectrometry interface.* Journal of the American Society for Mass Spectrometry, 2007. **18**(9): p. 1582-1590.

23. Wilhelm, O., L. Mädler, and S.E. Pratsinis, *Electrospray evaporation and deposition.* Journal of Aerosol Science, 2003. **34**(7): p. 815-836.

24. Gibson, S.C., C.S. Feigerle, and K.D. Cook, *Fluorometric measurement and modeling of droplet temperature changes in an electrospray plume.* Analytical chemistry, 2014. **86**(1): p. 464-472.

25. Tang, L. and P. Kebarle, *Dependence of ion intensity in electrospray mass spectrometry on the concentration of the analytes in the electrosprayed solution.* Analytical chemistry, 1993. **65**(24): p. 3654-3668.

26. Mylchreest, I.C. and M.E. Hail, *Electrospray ion source with reduced neutral noise and method*. 1992, Google Patents.

27. Voyksner, R.D. and H. Lee, *Improvements in LC/electrospray ion trap mass spectrometry performance using an off-axis nebulizer.* Analytical chemistry, 1999. **71**(7): p. 1441-1447.

28. Bantan, T., et al., *Investigation of low molecular weight Al complexes in human serum by fast protein liquid chromatography (FPLC)-ETAAS and electrospray (ES)-MS-MS techniques.* Journal of Analytical Atomic Spectrometry, 1999. **14**(11): p. 1743-1748.

29. McComb, M.E., L.J. Donald, and H. Perreault, *Electrospray ionization mass spectrometry and on-line capillary zone electrophoresis-mass spectrometry for the characterization of citrate synthase.* Canadian journal of chemistry, 1999. **77**(11): p. 1752-1760.

30. Lubin, A., et al., *Enhanced performance for the analysis of prostaglandins and thromboxanes by liquid chromatography-tandem mass spectrometry using a new atmospheric pressure ionization source.* Journal of Chromatography A, 2016. **1440**: p. 260-265.

31. Robichaud, G., et al., *Design, modeling, fabrication, and evaluation of the air amplifier for improved detection of biomolecules by electrospray ionization mass spectrometry.* International journal of mass spectrometry, 2011. **300**(2-3): p. 99-107.

32. Dixon, R.B., et al., *Probing the mechanisms of an air amplifier using a LTQ-FT-ICR-MS and fluorescence spectroscopy.* Journal of the American Society for Mass Spectrometry, 2007. **18**(11): p. 1909-1913.

33. Schneider, B.B., H. Javaheri, and T.R. Covey, *Ion sampling effects under conditions of total solvent consumption.* Rapid Communications in Mass Spectrometry: An International Journal Devoted to the Rapid Dissemination of Up-to-the-Minute Research in Mass Spectrometry, 2006. **20**(10): p. 1538-1544.

34. Cox, J.T., et al., *Improving the sensitivity of mass spectrometry by using a new sheath flow electrospray emitter array at subambient pressures.* Journal of the American Society for Mass Spectrometry, 2014. **25**(12): p. 2028-2037.

35. Kim, T., H.R. Udseth, and R.D. Smith, *Improved ion transmission from atmospheric pressure to high vacuum using a multicapillary inlet and electrodynamic ion funnel interface.* Analytical chemistry, 2000. **72**(20): p. 5014-5019.

36. Penn, S.G., et al., *The use of heated capillary dissociation and collision-induced dissociation to determine the strength of noncovalent bonding interactions in gas-*

*phase peptide-cyclodextrin complexes.* Journal of the American Society for Mass Spectrometry, 1997. **8**(3): p. 244-252.

37. Rockwood, A.L., et al., *Thermally induced dissociation of ions from electrospray mass spectrometry.* Rapid communications in mass spectrometry, 1991. **5**(12): p. 582-585.

38. Sakamoto, S., et al., *Characterization of self-assembling nano-sized structures by means of coldspray ionization mass spectrometry.* Tetrahedron, 2000. **56**(7): p. 955-964.

39. Gabelica, V. and E. De Pauw, *Comparison of the collision-induced dissociation of duplex DNA at different collision regimes: evidence for a multistep dissociation mechanism.* Journal of the American Society for Mass Spectrometry, 2002. **13**(1): p. 91-98.

40. Yamaguchi, K., *Cold-spray ionization mass spectrometry: principle and applications.* Journal of mass spectrometry, 2003. **38**(5): p. 473-490.

41. Gabelica, V., E. De Pauw, and M. Karas, *Influence of the capillary temperature and the source pressure on the internal energy distribution of electrosprayed ions.* International Journal of Mass Spectrometry, 2004. **231**(2-3): p. 189-195.

42. Krutchinsky, A.N., et al., *Maximizing ion transmission from atmospheric pressure into the vacuum of mass spectrometers with a novel electrospray interface.* Journal of The American Society for Mass Spectrometry, 2015. **26**(4): p. 649-658.

43. Pauly, M., et al., *A hydrodynamically optimized nano-electrospray ionization source and vacuum interface.* Analyst, 2014. **139**(8): p. 1856-1867.

44. Smith, D.P., *The electrohydrodynamic atomization of liquids.* IEEE transactions on industry applications, 1986(3): p. 527-535.

45. Hayati, I., A. Bailey, and T.F. Tadros, *J. Colloid Interface Sci.* Parts I and II, 1987. **117**: p. 205.

46. MOLIN, L. and P. TRALDI, *Basic aspects of electrospray ionization.* Advances in LC-MS Instrumentation, 2006: p. 1.

47. Wilm, M. and M. Mann, *Analytical properties of the nanoelectrospray ion source.* Analytical chemistry, 1996. **68**(1): p. 1-8.

48. De Juan, L. and J.F. De La Mora, *Charge and size distributions of electrospray drops.* Journal of colloid and interface science, 1997. **186**(2): p. 280-293.

49. Wilm, M.S. and M. Mann, *Electrospray and Taylor-Cone theory, Dole's beam of macromolecules at last?* International Journal of Mass Spectrometry and Ion Processes, 1994. **136**(2-3): p. 167-180.

50. Karas, M., U. Bahr, and T. Dülcks, *Nano-electrospray ionization mass spectrometry: addressing analytical problems beyond routine.* Fresenius' journal of analytical chemistry, 2000. **366**(6-7): p. 669-676.

51. Brouwers, J., H. Van Kemenade, and J. Kroes, *Rotational particle separator: An efficient method to separate micron-sized droplets and particles from fluids.* Filtration, 2012. **1**: p. 49-60.

52. Brouwers, J., *Phase separation in centrifugal fields with emphasis on the rotational particle separator.* Experimental thermal and fluid science, 2002. **26**(2-4): p. 325-334.

53. Nemes, P., I. Marginean, and A. Vertes, *Spraying mode effect on droplet formation and ion chemistry in electrosprays.* Analytical chemistry, 2007. **79**(8): p. 3105-3116.

54. Girod, M., et al., *Profiling an electrospray plume by laser-induced fluorescence and Fraunhofer diffraction combined to mass spectrometry: influence of size and composition of droplets on charge-state distributions of electrosprayed proteins.* Physical Chemistry Chemical Physics, 2012. **14**(26): p. 9389-9396.

55. Wang, W., et al., *Numerical Simulation of Ion Transport in a Nano-Electrospray Ion Source at Atmospheric Pressure.* Journal of The American Society for Mass Spectrometry, 2018. **29**(3): p. 600-612.

56. Ganan-Calvo, A., et al., *The electrostatic spray emitted from an electrified conical meniscus.* Journal of Aerosol Science, 1994. **25**(6): p. 1121-1142.

57. Rietveld, I.B., et al., *Electrospray deposition, model, and experiment: toward general control of film morphology.* The Journal of Physical Chemistry B, 2006. **110**(46): p. 23351-23364.

58. Page, J.S., et al., *Biases in ion transmission through an electrospray ionization-mass spectrometry capillary inlet.* Journal of the American Society for Mass Spectrometry, 2009. **20**(12): p. 2265-2272.

59. Zhou, X. and Z. Ouyang, *Following the ions through a mass spectrometer with atmospheric pressure interface: simulation of complete ion trajectories from ion source to mass analyzer.* Analytical chemistry, 2016. **88**(14): p. 7033-7040.

60. Jurčíček, P., L. Liu, and H. Zou, *Numerical simulation of Monte Carlo ion transport at atmospheric pressure within improved air amplifier geometry.* International Journal for Ion Mobility Spectrometry, 2014. **17**(3-4): p. 157-166.

61. ANSYS, A., *ANSYS Fluent User's Guide, 17.2.* Canonsburg: ANSYS, 2016.

62. Ringle, R., *3DCylPIC—a 3D particle-in-cell code in cylindrical coordinates for space charge simulations of ion trap and ion transport devices.* International Journal of Mass Spectrometry, 2011. **303**(1): p. 42-50.

63. COMSOL, M., *Comsol multiphysics user guide (version 5.2).* COMSOL, AB, 2015: p. 5-437.

64. Schiller, L., *A drag coefficient correlation.* Zeit. Ver. Deutsch. Ing., 1933. **77**: p. 318-320.

65. Davies, C., *Definitive equations for the fluid resistance of spheres.* Proceedings of the Physical Society, 1945. **57**(4): p. 259.

66. Abramzon, B. and W. Sirignano, *Droplet vaporization model for spray combustion calculations.* International journal of heat and mass transfer, 1989. **32**(9): p. 1605-1618.

67. Pope, S.B., *Turbulent flows*. 2001, IOP Publishing.

68. Olumee, Z., J.H. Callahan, and A. Vertes, *Droplet dynamics changes in electrostatic sprays of methanol− water mixtures.* The Journal of Physical Chemistry A, 1998. **102**(46): p. 9154-9160.

69. Liigand, P., et al., *The Evolution of Electrospray Generated Droplets is Not Affected by Ionization Mode.* Journal of The American Society for Mass Spectrometry, 2017. **28**(10): p. 2124-2131.

70. Tang, K. and A. Gomez, *On the structure of an electrostatic spray of monodisperse droplets.* Physics of Fluids, 1994. **6**(7): p. 2317-2332.

71. Pfeuffer, K.P., et al., *Visualization of mass transport and heat transfer in the FAPA ambient ionization source.* Journal of Analytical Atomic Spectrometry, 2013. **28**(3): p. 379-387.

72. Pfeuffer, K.P., S.J. Ray, and G.M. Hieftje, *Measurement and visualization of mass transport for the flowing atmospheric pressure afterglow (FAPA) ambient mass-spectrometry source.* Journal of the American Society for Mass Spectrometry, 2014. **25**(5): p. 800-808.

73. Rienitz, J., *Schlieren experiment 300 years ago.* Nature, 1975. **254**(5498): p. 293-295.

74. Krehl, P. and S. Engemann, *August Toepler—the first who visualized shock waves.* Shock Waves, 1995. **5**(1-2): p. 1-18.

75. Toepler, A.J.I., *Beobachtungen nach einer neuen optischen methode: Ein beitrag experimentalphysik*. 1906: W. Engelmann.

76. Gladstone, J.H. and T.P. Dale, *XIV. Researches on the refraction, dispersion, and sensitiveness of liquids.* Philosophical Transactions of the Royal Society of London, 1863(153): p. 317-343.

77. Settles, G.S., *Schlieren and shadowgraph techniques: visualizing phenomena in transparent media*. 2012: Springer Science & Business Media.

78. Mirabelli, M.F. and R. Zenobi, *Solid-phase microextraction coupled to capillary atmospheric pressure photoionization-mass spectrometry for direct analysis of polar and nonpolar compounds.* Analytical chemistry, 2018. **90**(8): p. 5015-5022.

79. Rouse, H., *Elementary fluid mechanics*. 1946, Wiley, New York.

80. Panda, J. and D. McLaughlin, *Experiments on the instabilities of a swirling jet.* Physics of Fluids, 1994. **6**(1): p. 263-276.

81. Rose, W., *A Swirling round turbulent jet: 1—Mean-flow measurements.* 1962.

82. Liang, H. and T. Maxworthy, *An experimental investigation of swirling jets.* Journal of Fluid Mechanics, 2005. **525**: p. 115-159.

83. Lott, W.G., *Hydrocyclone separator*. 2000, Google Patents.

84. Kottke, P.A., et al., *DRILL: An Electrospray Ionization-Mass Spectrometry Interface for Improved Sensitivity via Inertial Droplet Sorting and Electrohydrodynamic Focusing in a Swirling Flow.* Analytical chemistry, 2017. **89**(17): p. 8981-8987.

85. Gapeev, A., A. Berton, and D. Fabris, *Current-controlled nanospray ionization mass spectrometry.* Journal of the American Society for Mass Spectrometry, 2009. **20**(7): p. 1334-1341.

86. Juraschek, R., et al., *Dependence of Electrospray Ionization Efficiency on Axial Spray Modes.* Adv. Mass Spectrom, 1998. **14**: p. 1-15.

87. Wu, Q., et al., *Characterization of cytochrome c variants with high-resolution FTICR mass spectrometry: correlation of fragmentation and structure.* Analytical chemistry, 1995. **67**(14): p. 2498-2509.

88. Chowdhury, S.K., V. Katta, and B.T. Chait, *Probing conformational changes in proteins by mass spectrometry.* Journal of the American Chemical Society, 1990. **112**(24): p. 9012-9013.

89. Ferguson, P.L., et al., *Protein folding and protein-ligand interactions monitored by electrospray mass spectrometry.* Current Analytical Chemistry, 2009. **5**(2): p. 186-204.

90. Heck, A.J. and R.H. van den Heuvel, *Investigation of intact protein complexes by mass spectrometry.* Mass spectrometry reviews, 2004. **23**(5): p. 368-389.

91. Müller, M., et al., *Limits for the detection of (poly-) phosphoinositides by matrix-assisted laser desorption and ionization time-of-flight mass spectrometry (MALDI-TOF MS).* Chemistry and physics of lipids, 2001. **110**(2): p. 151-164.

92. Cech, N.B. and C.G. Enke, *Relating electrospray ionization response to nonpolar character of small peptides.* Analytical Chemistry, 2000. **72**(13): p. 2717-2723.

93. Randall, S.M., et al., *Evaluating Nonpolar Surface Area and LC/MS Response: An Application for Site Occupancy Measurements for Enzyme Intermediates in Polyketide Biosynthesis.* Rapid communications in mass spectrometry: RCM, 2014. **28**(23): p. 2511.

94. Shuford, C.M., et al., *Improving limits of detection for B-type natriuretic peptide using PC-IDMS: An application of the ALiPHAT strategy.* Analyst, 2010. **135**(1): p. 36-41.

95. Williams, D.K., et al., *Evaluation of the ALiPHAT method for PC-IDMS and correlation of limits-of-detection with nonpolar surface area.* Journal of the American Society for Mass Spectrometry, 2009. **20**(11): p. 2006-2012.

96. Walker, S.H., et al., *Hydrophobic derivatization of N-linked glycans for increased ion abundance in electrospray ionization mass spectrometry.* Journal of The American Society for Mass Spectrometry, 2011. **22**(8): p. 1309-1317.

97. Andrew Karplus, P., *Hydrophobicity regained.* Protein Science, 1997. **6**(6): p. 1302-1307.

98. Banerjee, S. and S. Mazumdar, *Electrospray ionization mass spectrometry: a technique to access the information beyond the molecular weight of the analyte.* International journal of analytical chemistry, 2012. **2012**.

99. Intra, P. and N. Tippayawong, *An overview of differential mobility analyzers for size classification of nanometer-sized aerosol particles.* Songklanakarin Journal of Science & Technology, 2008. **30**(2).

100. Johnson, G.E., et al., *DRILL Interface Makes Ion Soft Landing Broadly Accessible for Energy Science and Applications.* Batteries & supercaps, 2018. **1**(3): p. 97-101.

101. Prabhakaran, V., et al., *Rational design of efficient electrode–electrolyte interfaces for solid-state energy storage using ion soft landing.* Nature communications, 2016. **7**(1): p. 1-10.

102. Mikhailov, V.A., et al., *Mass-selective soft-landing of protein assemblies with controlled landing energies.* Analytical chemistry, 2014. **86**(16): p. 8321-8328.